

1-1-2002

## Direct numerical simulations of channel flows with two splitter plates

Anup Ganesh Gokarn  
Iowa State University

Follow this and additional works at: <https://lib.dr.iastate.edu/rtd>

### Recommended Citation

Gokarn, Anup Ganesh, "Direct numerical simulations of channel flows with two splitter plates" (2002).  
*Retrospective Theses and Dissertations*. 19857.  
<https://lib.dr.iastate.edu/rtd/19857>

This Thesis is brought to you for free and open access by the Iowa State University Capstones, Theses and Dissertations at Iowa State University Digital Repository. It has been accepted for inclusion in Retrospective Theses and Dissertations by an authorized administrator of Iowa State University Digital Repository. For more information, please contact [digirep@iastate.edu](mailto:digirep@iastate.edu).

Direct numerical simulations of channel flows with two splitter plates

by

Anup Ganesh Gokarn

A thesis submitted to the graduate faculty  
in partial fulfillment of the requirements for the degree of  
MASTER OF SCIENCE

Major: Mechanical Engineering

Program of Study Committee:  
Francine Battaglia, Major Professor  
Rodney O. Fox  
Richard H. Pletcher

Iowa State University

Ames, Iowa

2002

Copyright © Anup Ganesh Gokarn, 2002. All rights reserved.

Graduate College  
Iowa State University

This is to certify that the master's thesis of  
Anup Ganesh Gokarn  
has met the thesis requirements of Iowa State University

Signatures have been redacted for privacy

---

## ABSTRACT

In this research, direct numerical simulations are performed for the evolution of a mixing layer in a reactor with two splitter plates at the inlet, for the first time. A splitter plate configuration is a well-studied geometry, known to induce mixing as a result of the Kelvin-Helmholtz instability in shear layers. Turbulent mixing processes are of great importance in reacting flows owing to the fact that turbulence induces reactants to mix rapidly thereby increasing the reaction rate. A turbulent mixing flow exhibits complex dynamic behavior and the advection of a passive scalar, such as a reactant, by the same flow reveals many phenomenological parallels with the behavior of the velocity field.

Detailed field information is obtained by solving the unsteady Navier-Stokes equations. A time marching method which utilizes an artificial compressibility formulation is employed for transient solutions using a dual-time stepping technique. Finite difference schemes are used to discretize the equations.

The two-dimensional simulations of the unsteady, spatially developing mixing layer are able to capture the large-scale vortical structures that are shed at the trailing edge of the splitter plates. The growth of the mixing layer is due to pairing of neighboring vortices. Instability of the flow increases as the velocity ratio decreases and the vortex rollups occur closer to the trailing edge of splitter plates. The vortex strength also increases with decreasing velocity ratio. The transport of a conserved passive scalar is examined to assess the mechanisms of entrainment and mixing within the shear flow. The scalars mix in the channel by means of advection and diffusion. Better mixing at lower velocity ratios is attained due to increased advection. Mean and RMS scalar

profiles emphasize the fact that mixing is enhanced when the inner feed stream is much faster than the outer feed streams. The scalar probability density functions revealed the evolution of the mixing layer along the streamwise direction. Based on the simulated results, the validity of the turbulent viscosity and gradient diffusion closures were assessed. The study was extended to the three-dimensional mixing layer to set a foundation for future computational studies.

## TABLE OF CONTENTS

<b>CHAPTER 1 INTRODUCTION</b> . . . . .	1
1.1 Background . . . . .	1
1.2 Motivation . . . . .	2
1.3 Statement of problem . . . . .	4
<b>CHAPTER 2 LITERATURE REVIEW</b> . . . . .	6
2.1 The two-dimensional shear layer . . . . .	6
2.2 Numerical simulations . . . . .	9
2.3 Passive scalars and chemical reactions . . . . .	10
2.4 The three-dimensional evolution of the mixing layer . . . . .	13
2.5 Summary . . . . .	14
<b>CHAPTER 3 MATHEMATICAL FORMULATION</b> . . . . .	16
3.1 Governing equations . . . . .	16
3.2 Time-marching methods . . . . .	18
3.2.1 The dependent variables . . . . .	19
3.2.2 Preconditioning technique . . . . .	20
3.2.3 Dual-time stepping procedure . . . . .	21
3.3 Numerical formulation . . . . .	21
3.3.1 Coordinate transformation . . . . .	22
3.3.2 Spatial discretization . . . . .	23
3.3.3 Implicit time discretization . . . . .	23

3.3.4	Runge-Kutta method . . . . .	25
3.4	Mathematical and computational conditions . . . . .	27
3.4.1	Boundary conditions . . . . .	27
3.4.2	Initial condition . . . . .	28
3.4.3	Computational parameters . . . . .	29
<b>CHAPTER 4 NUMERICAL SOLUTIONS OF FLOW IN 2-D RE-</b>		
<b>ACTOR: VELOCITY AND VORTICITY . . . . .</b>		<b>30</b>
4.1	Geometry of reactor . . . . .	30
4.2	Initial and boundary conditions . . . . .	31
4.3	Computational performance . . . . .	31
4.4	The two-dimensional mixing layer . . . . .	33
4.4.1	Characteristics of evolution of mixing layer (results for $r = 0.5$ ) . . . . .	33
4.4.2	Generation of instability and growth of mixing layer . . . . .	37
4.5	Results for different velocity ratios. . . . .	39
<b>CHAPTER 5 NUMERICAL SOLUTIONS OF FLOW IN 2-D RE-</b>		
<b>ACTOR: SCALAR MIXING AND TURBULENCE CLOSURES . . . . .</b>		<b>47</b>
5.1	Boundary conditions . . . . .	48
5.2	Scalar mixing (results for $r = 0.5$ ) . . . . .	48
5.3	Results for different velocity ratios. . . . .	51
5.4	Probability density function (PDF) . . . . .	56
5.5	Assessment of turbulence closures: turbulent viscosity and gradient dif- fusion hypotheses . . . . .	60
5.5.1	Turbulent viscosity . . . . .	61
5.5.2	Turbulent diffusivity . . . . .	61
5.6	Modeling of turbulent convective fluxes . . . . .	61

<b>CHAPTER 6 TOWARD THREE-DIMENSIONAL SOLUTIONS: PROGRESS AND FUTURE WORK . . . . .</b>	<b>67</b>
6.1 Numerical considerations . . . . .	68
6.2 Configuration . . . . .	68
6.2.1 Geometry and mesh . . . . .	68
6.2.2 Initial and boundary conditions . . . . .	69
6.3 Results . . . . .	69
<b>CHAPTER 7 CONCLUDING REMARKS . . . . .</b>	<b>81</b>

## LIST OF TABLES

3.1	Numerical parameters for two- and three-dimensional flows. . . .	29
-----	--	----

## LIST OF FIGURES

4.1	Schematic of planar mixing of three co-flowing streams in a symmetric channel. . . . .	31
4.2	Grid for the two-dimensional reactor. Mesh is $1025 \times 129$ grid points showing every 4th node in $x$ and $y$ . . . . .	32
4.3	Instantaneous velocity vector plot at $t = 53.94$ s, showing every 12th vector in $x$ and 2nd vector in $y$ , $Re = 3000$ , $r = 0.5$ . . . . .	34
4.4	Instantaneous velocity vector plot at $t = 53.94$ s, showing every 100th vector in $x$ and 2nd vector in $y$ , $Re = 3000$ , $r = 0.5$ . . . . .	34
4.5	Instantaneous contour plot showing pressure distribution in the channel at $t = 53.94$ s for $Re = 3000$ , $r = 0.5$ . . . . .	35
4.6	Instantaneous contour plot of $u$ -velocity in the channel at $t = 53.94$ s for $Re = 3000$ , $r = 0.5$ . . . . .	35
4.7	Instantaneous contour plot of $v$ -velocity in the channel at $t = 53.94$ s for $Re = 3000$ , $r = 0.5$ . . . . .	35
4.8	Time-averaged contour plot of streamwise velocity for $Re = 3000$ , $r = 0.5$ . . . . .	36
4.9	Normalized mean streamwise velocity at different streamwise locations for $Re=3000$ , $r = 0.5$ . . . . .	36
4.10	Evolution of spanwise vorticity field for $Re = 3000$ , $r = 0.5$ . . . . .	38
4.11	Instantaneous spanwise vorticity contour plot at $t = 39.94$ s for $Re = 3000$ and $r = 0.5$ , $r = 0.3$ and $r = 0.25$ . . . . .	40

4.12	Normalized mean streamwise velocity at different streamwise locations for $Re = 3000$ , $r = 0.3$ . . . . .	41
4.13	Normalized mean streamwise velocity at different streamwise locations for $Re = 3000$ , $r = 0.25$ . . . . .	41
4.14	Normalized RMS streamwise velocity at different streamwise locations for $Re = 3000$ , $r = 0.5$ . . . . .	42
4.15	Normalized RMS streamwise velocity at different streamwise locations for $Re = 3000$ , $r = 0.3$ . . . . .	43
4.16	Normalized RMS streamwise velocity at different streamwise locations for $Re = 3000$ , $r = 0.25$ . . . . .	43
4.17	Normalized RMS cross-stream velocity at different streamwise locations for $Re = 3000$ , $r = 0.5$ . . . . .	44
4.18	Normalized RMS cross-stream velocity at different streamwise locations for $Re = 3000$ , $r = 0.3$ . . . . .	44
4.19	Normalized RMS cross-stream velocity at different streamwise locations for $Re = 3000$ , $r = 0.25$ . . . . .	45
4.20	Normalized mean Reynolds stress at different streamwise locations for $Re = 3000$ , $r = 0.5$ . . . . .	45
4.21	Normalized mean Reynolds stress at different streamwise locations for $Re = 3000$ , $r = 0.3$ . . . . .	46
4.22	Normalized mean Reynolds stress at different streamwise locations for $Re = 3000$ , $r = 0.25$ . . . . .	46
5.1	Instantaneous contour of scalar diffusing in the shear layer for $Re = 3000$ , $r = 0.5$ . . . . .	49
5.2	Time-averaged scalar contour for $Re = 3000$ , $r = 0.5$ . . . . .	50

5.3	Time-averaged scalar variance plot showing the extent of mixing for $Re = 3000$ , $r = 0.5$ . . . . .	51
5.4	Time-averaged intensity of segregation characterizing the concentration uniformity for $Re = 3000$ , $r = 0.5$ . . . . .	51
5.5	Normalized mean conserved scalar profiles for $Re = 3000$ , $r = 0.5$ .	52
5.6	Normalized mean conserved scalar profiles for $Re = 3000$ , $r = 0.3$ .	52
5.7	Normalized mean conserved scalar profiles for $Re = 3000$ , $r = 0.25$ , . . . . .	53
5.8	Normalized RMS conserved scalar profiles for $Re = 3000$ , $r = 0.5$ .	54
5.9	Normalized RMS conserved scalar profiles for $Re = 3000$ , $r = 0.3$ .	54
5.10	Normalized RMS conserved scalar profiles for $Re = 3000$ , $r = 0.25$ .	55
5.11	A typical PDF . . . . .	56
5.12	Evolution of the PDF of the scalar field for $Re = 3000$ , $r = 0.5$ , (a) $x = 0.5$ m, (b) $x = 0.6$ m, (c) $x = 0.7$ m, (d) $x = 0.8$ m. . . . .	57
5.13	Evolution of the PDF of the scalar field for $Re = 3000$ , $r = 0.3$ , (a) $x = 0.5$ m, (b) $x = 0.6$ m, (c) $x = 0.7$ m, (d) $x = 0.8$ m. . . . .	58
5.14	Evolution of the PDF of the scalar field for $Re = 3000$ , $r = 0.25$ , (a) $x = 0.5$ m, (b) $x = 0.6$ m, (c) $x = 0.7$ m, (d) $x = 0.8$ m. . . . .	59
5.15	Normalized turbulent viscosity at $x = 0.5, 0.6$ m for $Re = 3000$ , $r = 0.5$ , showing every 3rd point. . . . .	63
5.16	Normalized turbulent viscosity at $x = 0.5, 0.6$ m for $Re = 3000$ , $r = 0.3$ , showing every 3rd point. . . . .	63
5.17	Normalized turbulent viscosity at $x = 0.5, 0.6$ m for $Re = 3000$ , $r = 0.25$ , showing every 3rd point. . . . .	64
5.18	Turbulent Schmidt number at $x = 0.5, 0.6$ m for $Re = 3000$ , $r = 0.5$ , showing every 3rd point. . . . .	65

5.19	Turbulent Schmidt number at $x = 0.5, 0.6$ m for $Re = 3000$ , $r = 0.3$ , showing every 3rd point, $Re = 3000$ . . . . .	65
5.20	Turbulent Schmidt number at $x = 0.5, 0.6$ m for $Re = 3000$ , $r = 0.25$ , showing every 3rd point, $Re = 3000$ . . . . .	66
6.1	Schematic of mixing of three co-flowing streams in a reactor. . .	69
6.2	Grid for a three-dimensional reactor. Mesh is $513 \times 65 \times 73$ showing every 4th node in $x, y$ and $z$ directions. . . . .	70
6.3	Spanwise vorticity contours at three spanwise planes for $Re =$ $1500, t = 75$ s, $r = 0.3$ . . . . .	72
6.4	Conserved scalar contours at three spanwise locations for $Re =$ $1500, t = 75$ s, $r = 0.3$ . . . . .	73
6.5	Cross-stream vorticity contours at three cross-stream planes for $Re = 1500, t = 75$ s, $r = 0.3$ . . . . .	74
6.6	Conserved scalar contours at three cross-stream locations for $Re = 1500, t = 75$ s, $r = 0.3$ . . . . .	75
6.7	Three-dimensional iso-vorticity contours of magnitude $2.5$ 1/s for $Re = 1500, t = 75$ s, $r = 0.3$ . . . . .	77
6.8	Streamwise vorticity at locations for $Re = 1500$ (a) $x = 0.7$ m, (b) $x = 0.8$ m, (c) $x = 0.9$ m, (d) $x = 1.0$ m, $t = 75$ s, $r = 0.3$ . . .	78
6.9	Conserved scalar contours at locations for $Re = 1500$ (a) $x = 0.7$ m, (b) $x = 0.8$ m, (c) $x = 0.9$ m, (d) $x = 1.0$ m, $t = 75$ s, $r = 0.3$ . . .	79

## NOMENCLATURE

$\mathcal{D}$	molecular diffusivity
$E$	conservative flux vector in the $x$ direction
$\hat{E}$	conservative flux vector in the $\xi$ direction
$E_\nu$	viscous flux vector in the $x$ direction
$\hat{E}_\nu$	viscous flux vector in the $\xi$ direction
$F$	conservative flux vector in the $y$ direction
$\hat{F}$	conservative flux vector in the $\eta$ direction
$F_\nu$	viscous flux vector in the $y$ direction
$\hat{F}_\nu$	viscous flux vector in the $\eta$ direction
$G$	conservative flux vector in the $z$ direction
$\hat{G}$	conservative flux vector in the $\zeta$ direction
$G_\nu$	viscous flux vector in the $z$ direction
$\hat{G}_\nu$	viscous flux vector in the $\zeta$ direction
$h$	channel height
$J$	Jacobian
$L_c$	length of channel
$L_s$	length of splitter plate
$\hat{n}$	unit normal direction
$p$	pressure
$Q$	vector of conservative dependent variables

$Q_v$	vector of primitive variables
$Re$	Reynolds number
$Sc$	molecular Schmidt number
$Sc_T$	turbulent Schmidt number
$r$	velocity ratio of slower to faster fluid
$t$	time
$\Delta t$	time step
$\mathbf{u}$	velocity vector
$u$	streamwise velocity component
$u_1$	speed of faster fluid in channel
$u_2$	speed of slower fluid in channel
$\bar{u}$	average velocity in the channel
$U$	contravariant velocity component in the $\xi$ direction
$v$	cross-stream velocity component
$V$	contravariant velocity component in the $\eta$ direction
$w$	spanwise velocity component
$W$	contravariant velocity component in the $\zeta$ direction
$x$	streamwise direction
$y$	cross-stream direction
$z$	spanwise direction

## Greek Symbols

$\alpha$	constant in Runge-Kutta algorithm
$\beta$	artificial compressibility parameter
$\Delta$	delta form

$\epsilon_e$	artificial dissipation coefficient
$\Gamma$	matrix for physical time derivative
$\Gamma_p$	preconditioning matrix
$\Gamma_T$	turbulent diffusivity
$\lambda$	eigenvalue
$\lambda_B$	Batchelor's scale
$\lambda_\nu$	viscous scale
$\nu$	kinematic viscosity
$\nu_T$	turbulent viscosity
$\phi$	conserved passive scalar
$\rho$	density
$\sigma$	von Neumann number
$\tau$	pseudo-time variable
$\Delta\tau$	pseudo-time step
$\omega$	vorticity
$\xi, \eta, \zeta$	independent variables in generalized coordinate system

## Superscripts

*	Runge-Kutta intermediate stage
$k$	pseudo-time level
$n$	physical time level
$T$	transpose of a matrix
'	fluctuating component of variable

## Subscripts

$x, y, z$	partial derivatives with respect to physical coordinates
$\xi, \eta, \zeta$	partial derivatives with respect to transformed coordinates

## Other Symbols

$\nabla$	gradient operator
$\nabla \cdot$	divergence operator
$\nabla^2$	Laplacian operator
$\nabla \times$	curl operator
$\langle \rangle$	mean or expectation

## Abbreviations

CFL	Courant-Fredrichs-Lewy number
DNS	direct numerical simulations
LES	large eddy simulations
SGS	sub grid scale
STM	statistical turbulence modeling
PDF	probability density function
RANS	Reynolds averaged Navier–Stokes equations

## CHAPTER 1 INTRODUCTION

### 1.1 Background

The phenomenon of turbulence in fluid flow has been a widely studied topic for centuries. The complex behavior of turbulent flows is governed by the Navier–Stokes equations. The non–linear nature of this system of equations gives rise to a rich variety of fascinating phenomena. In any fluid flow there exist perturbations in initial conditions, boundary conditions, and material properties. Perturbations in initial conditions could be due to slight variations in the mass flow rate at the inlet, while those at boundaries could be due to vibration of apparatus or from the finish of nominally smooth apparatus or complex geometries with sharp corners. With care and effort, these perturbations can be reduced, but they cannot be eliminated. In the case of turbulent flows, the evolution of the flow field is extremely sensitive to small changes in initial conditions, boundary conditions and material properties [1]. As a result of this, analytical solutions to even the simplest turbulent flows do not exist [2].

All turbulent flows are characterized by irregularities in time and space, mixing, nonlinearities, dissipation and large ranges of length and time scales. Principally, there are three different approaches to predict turbulent flows [3]:

1. Statistical turbulence modeling (STM).
2. Large eddy simulations (LES).
3. Direct numerical simulations (DNS).

The above classification is cited according to the potential usefulness of each methodology, ending with the most promising. In STM, the variables are broken down into their mean and fluctuating parts and then solved as in Reynolds-averaged Navier–Stokes equations. However, STM is associated with the highest loss of quantitative information due to closure models required by the method. The main problem is associated with modeling the pressure–strain rates and dissipation rate tensors. Large eddy simulations are intermediate methods between STM and DNS since they predict the dynamics of the large turbulent scales. In general, numerical simulations are the result of discretized equations solved on a grid. The size of a grid impacts the accuracy of the solution as well as calculation time required for the problem. With LES, the three–dimensional, time–dependent transport equations are filtered to separate the large and small scales since the small scales are less anisotropic and less influenced by the flow geometry. The large-scale flow features are then directly resolved numerically while the small scales are modeled using subgrid–scale (SGS) models. The advantage of LES is that since SGS models are used, grid resolution is not a primary issue. An alternative approach is to obtain a complete description of a turbulent flow without using filtered equations. The approach is known as DNS, whereby the transport equations are *directly* solved. With DNS, grid resolution is an important consideration in that a very fine grid is required to capture the small scale flow features. Since the required number of grid points increases faster than the square of the Reynolds number, DNS are at present feasible only at low or moderate Reynolds numbers [3].

## 1.2 Motivation

Reducing pollution and toxic byproducts caused by poor product selectivity is a critical step towards the development of environmentally–friendly, sustainable chemical processes [4]. The ultimate impact of reducing undesirable emissions will depend on

successful implementation of chemical process design in industry. To advance design in the chemical process industry, high-end computing technology will play a major role.

DNS have been established along with LES as important tools for research in turbulent fluid mechanics. The progress in computational power, such as memory and high-speed processors, has provided greater opportunities to investigate high Reynolds number turbulent flows using DNS and LES. Turbulent mixing processes are of great importance in reacting flows owing to the fact that turbulence induces reactants to mix rapidly thereby increasing the reaction rate [5]. Including chemistry into a calculation significantly increases the computational time required to solve a problem.

Detailed field information for complex turbulent flows can be obtained by solving the unsteady Navier–Stokes equations using DNS. A highly-resolved simulation precludes the need for closure models. DNS are then useful for testing and parameterizing more approximate methods such as LES. In addition, DNS are useful for studying the underlying physics of the problem; it is possible to numerically probe the database of velocity and concentration fields to measure and visualize quantities that cannot be obtained in the laboratory.

A splitter plate configuration is a well-studied geometry, known to induce mixing as a result of the Kelvin–Helmholtz instability in a planar shear layer. A turbulent mixing flow exhibits complex dynamic behavior; the advection of a passive scalar, such as a reactant, by the same flow can reveal many phenomenological parallels with the behavior of the velocity field. Turbulent flow transports and disperses the scalar through parcels of fluid following chaotic trajectories of the evolving structures in the shear layer [6]. From a DNS viewpoint, turbulent shear flow develops over a broad range of space and time scales. In this research, the goal is to study the hydrodynamic mixing and evolution of shear layers using DNS. Passive scalars will be used to examine the behavior of entrainment and mixing. DNS results will be validated against experimental data which will be obtained in the near future.

The DNS code used for the present research has been benchmarked by Deshpande *et al.* [7] for cavity flow predictions and Battaglia *et al.* [8] for flows in channels. The results show good agreement with experimental measurements, and provide confidence for use in the present research.

### 1.3 Statement of problem

The focus of the present research is to analyze and understand the entrainment and mixing characteristics of flow in a reactor geometry with two splitter plates. Flow fields in two-dimensional planar channels and three-dimensional rectangular ducts are studied numerically to understand the mechanism and occurrence of instability leading to mixing. Extensive research has been done in the past on shear-layers generated by a single splitter plate. In the present research, we look at the shear layers generated by two splitter plates and the interaction between them. The future work on this project involves chemical reactions. As a first step, passive scalars are used to understand the mechanism of mixing in this research.

Chapter 2 is a detailed survey of literature from the past decades. Included are reviews of shear layers in two-dimensional planar flows as well as recent advancements in three-dimensional channel flows. The full, incompressible, Navier-Stokes equations are discretized and the governing equations and numerical formulations are presented in Chapter 3. A time-marching, finite difference procedure is used, where the dual-time stepping technique is coupled with the artificial compressibility formulation. The equations are solved based on a Cartesian coordinate system.

Results pertaining to two-dimensional flows are discussed in Chapters 4 and 5. In Chapter 4, the hydrodynamic evolution, entrainment and mixing characteristics of the incompressible mixing layer are presented. Chapter 5 discusses the mixing of a passive scalar in the channel. The results generated by DNS are statistically analyzed in an

attempt to develop turbulence closures for statistical modeling of shear flows.

Three-dimensional rectangular duct flows are presented in Chapter 6. The results are preliminary and the three-dimensional evolution of the plane mixing layer is discussed in brief. Chapter 7 closes with a summary of findings and conclusions and recommendations for future work.

## CHAPTER 2 LITERATURE REVIEW

Turbulent mixing has been the focus of research for over three decades. A turbulent mixing layer is formed when two fluids of unequal velocity flow parallel to each other and interact. Turbulent mixing layers have been the subject of extensive experimental, numerical and theoretical studies due to their common technological occurrence and significant importance in mixing processes, often combined with chemical reactions and combustion. Most of the initial research on mixing layers was conducted experimentally. A decade later, numerical simulations followed. Both gaseous and liquid mixing layers have been studied. Deterministic models have also been proposed for the mixing phenomenon. Effects of parametric variations such as velocity ratio, density ratio, initial and inflow conditions, Reynolds number, etc. on the behavior of the mixing layer have been explored. These will be discussed in the ensuing paragraphs. Although the present research involves two splitter plates, the characteristics of the mixing layers are similar to flows with a single splitter-plate configuration.

### 2.1 The two-dimensional shear layer

The classical picture of turbulence was one of chaos and disorder. It was therefore rather astonishing when shadow graphs of the flow revealed the presence of well-defined large structures with the appearance of breaking waves or rollers or vortices [9–18]. The mean flow is controlled by these large, organized structures, which are not affected by the small-scale turbulence appearing at higher values of Reynolds numbers. The measured

mean properties of the flow, velocity and density profiles, spreading rate, etc. do not vary much for a wide range of Reynolds numbers. The sizes of vortices and their spacing relative to each other increases downstream of the splitter plate and both are related to the thickness of the mixing layer. Pairing is attributed to be the dominant mode of vortex interaction and the principal mechanism for growth of these structures. In pairing, neighboring vortices rotate around each other and coalesce into a larger structure. This mode of coalescence, however, is not seen in flows with a large density difference [11].

A fundamental property of turbulent shear flows is entrainment. Entrainment is the incorporation of non-turbulent, irrotational fluid into the turbulent region. Continuous repetition of the pairing process is responsible for the entrainment of the surrounding fluid, controlling the growth of the mixing layer [12]. The structures derive energy directly from the velocity difference between the two streams and pairing is a result of the instability of the row of finite amplitude vortical structures [9]. After coalescence, the spacing between vortices roughly doubles.

Existence of vortical structures for Reynolds numbers as high as  $3 \times 10^6$  proves that the structures persist at high Reynolds number flows and are not just at transition from the well-defined periodicity of the laminar instability region [13]. The induced velocity at a point in the shear layer owing to a vortical structure downstream diminishes inversely as the distance of the structure from the shear layer origin. However, the strength of the vortical structure increases in proportion to the distance between the structure and the shear-layer origin [19]. Conditional sampling of the mixing layer indicates that Reynolds-stress production is associated with the pairing interaction of vortices [12] and 50% of the turbulent kinetic energy is associated with the vortices [15]. Vortex interactions are responsible for the cross-stream momentum transfer. Even for flows with non-uniform density, the mixing layer is dominated by large coherent structures. Large changes in the density ratio have a relatively small effect on the spreading of the layer. For incompressible flow, a density ratio of 7 decreases the vorticity thickness

by about 30% compared with the uniform density case [10]. The spreading angle of the density profile is greater than that for velocity. The implication is that different diffusion rates exist for mass and momentum and must be taken into account for any model constructed to calculate variable-density turbulent flows. There are, however, a number of studies [20,21] that view the structures as a result of forcing or as a transition, rather than as an integral part of the turbulence.

An initial condition has a long lasting effect on the development of the mixing layer [14, 22–24]. In an unforced experiment, random background noise supplies the perturbation necessary for initial vortex formation. The particular component of the background noise responsible for vortex formation is determined from linear inviscid stability theory as the frequency that exhibits the largest spatial growth rate [22]. If the mixing layer is perturbed near a subharmonic of the most-amplified frequency, the spreading rate of a mixing layer can be manipulated. A subharmonic forcing technique makes several vortices merge simultaneously thereby increasing the spreading rate. A mechanism called collective interaction bypasses the sequential stages of vortex merging and makes a large number of vortices (ten or more) coalesce [14]. Oscillatory forcing is sometimes used at inflow to intensify the mixing process in the shear layer for low Reynolds number flows since shear layers require long distances to develop [23]. The spreading rate and velocity profiles of a forced mixing layer are distinctly different from an unforced case. When the amplitude and frequency of the forcing component are tuned with the unforced frequency response of the flow field, maximum effects on the vortex structures are observed. However, the effects of forcing do not have substantial effect on the flow in the later stages of development [24].

An important feature of the mixing layer that was discovered is asymmetric mixing of the two fluids in the mixing layer [17, 25–28], that is, there is more high-speed fluid than low-speed fluid entrained and mixed in the coherent structures.

## 2.2 Numerical simulations

The bulk of research effort on the mixing layer has been primarily experimental. Attempts have been made in solving the linearized Navier-Stokes equations [29] and inviscid Euler equations [27]. The progress in computational power, such as memory and high-speed processors, has provided greater opportunities to investigate high Reynolds number turbulent flows using direct numerical simulations (DNS) and large eddy simulations (LES). A few numerical methods used to simulate the mixing layer are outlined to demonstrate the progress in this area.

1. A high-order, finite-element 2-D isoparametric spectral element method has been implemented [23]. This technique divides the domain into a series of quadrangular elements transformed into regular squares. All functions are represented as tensor-product high-order Lagrangian interpolants through Gauss-Lobatto-Chebyshev collocating points. The method incorporates a splitting scheme that effectively separates the nonlinear pressure and viscous parts of the Navier-Stokes equations. An explicit standard collocation approach with third-order Adams-Bashforth is used for the nonlinear terms. The remaining pressure and viscous parts are solved implicitly with variational projection operators based on Chebyshev polynomial expansions. The solver is either a direct matrix inversion or an iterative conjugate gradient method.
2. Flux-Corrected Transport (FCT), a nonlinear, monotone, finite-difference technique is used for solving the governing equations [27]. FCT adds linear velocity-dependent diffusion to a high-order algorithm during convective transport. Fourth order accuracy is maintained by subtracting out the added diffusion during a second nonlinear anti-diffusion stage. FCT has the ability to separate grid motions from the fluid flow. This allows for variably spaced grids as well as adaptive grids.

The algorithm is explicit in nature.

3. Direct lagrangian simulations (DLS) using a “transport-element” method are performed for an inviscid mixing layer [24]. The Lagrangian simulation is a “grid free” discretization of the transport equations for the vorticity and for the gradients of the mixture fraction. A beta density model is used to calculate the probability distribution of an appropriately defined Shvab-Zeldovich variable. It is shown that the gradient diffusion model works reasonably well to account for the effects of turbulent convective fluxes.
4. A methodology named the filtered mass density function (FMDF) is developed and implemented for large eddy simulations of variable-density chemically reacting turbulent flows at low mach numbers [30]. The FMDF represents the joint probability density function of the subgrid-scale (SGS) scalar quantities and is obtained by solution of its modeled transport equation. In this equation, the effect of chemical reactions appears in a closed form and the influences of SGS mixing and convection are modeled. The equations are solved via a lagrangian Monte Carlo scheme.
5. A method, velocity filtered density function (VFDF), is developed and implemented for large eddy simulation of turbulent flows [31]. The effects of the unresolved subgrid scales are taken into account by considering the joint probability density function of all the components of the velocity vector. Lagrangian Monte Carlo scheme is used to solve the equations.

### 2.3 Passive scalars and chemical reactions

So far, the hydrodynamic characteristics of the turbulent mixing layer were discussed. Mixing in reacting turbulent shear layers has also been well documented. Non-reacting

flow experiments established the hydrodynamic field and the entrainment and mixing characteristics of the mixing layer [9–15, 18]. In non-reacting cases, sometimes a passive scalar is used to measure the probability distribution function of the composition field. These studies help in understanding the extent of mixing in the layer at a molecular level [17, 24, 26, 28, 32–36].

The amount of molecular scale mixing in a turbulent shear layer between two streams can be measured in at least two ways [32, 34]. The passive-scalar technique consists of introducing a passive scalar contaminant into one stream and measuring the local instantaneous concentration as a function of time. This method is found to have resolution problems. If the probe sampling volume is small compared to the smallest concentration scales then it is possible to measure the true local concentration and to infer the product information at that point [32]. If, however, the sampling volume is too large, concentration fluctuations are smoothed out and the inferred amount of mixing or chemical reaction is overestimated. The second technique is to use a method whereby mixing at the molecular level is displayed macroscopically in some conveniently measurable fashion [26, 34]. Such a process is a fast second-order chemical reaction of the type  $A + B \rightarrow P$ . If a dilute reactant  $A$  is added to one stream and dilute reactant  $B$  is added to the other, and if they react rapidly and irreversibly to form reaction product  $P$ , then the amount of product formed is directly proportional to the consumption of the lean reactant, and is a measure of the amount of molecular mixing. In contrast with the passive-scalar technique [36], a finite sampling volume does not inherently overestimate the amount of mixing. For an irreversible reaction, the total amount of mixed fluid within the sampling volume is proportional to the amount of product, independent of the sampling size of the volume. With the drawbacks associated with the passive-scalar method in determining the true extent of molecular mixing, it is nevertheless the simplest way to get an estimate of the composition field.

Chemical reactions have been carried out in liquid as well as gaseous shear layers.

The distinction between gas and liquid, in the context of mixing, is due to their different molecular diffusivities. Gases are characterized by a high mass-diffusion coefficient or, in non-dimensional form, a Schmidt number of order unity. The Schmidt number is the ratio of the diffusion coefficient of momentum to that of mass. A liquid has a low mass-diffusion coefficient leading to higher values of Schmidt numbers on the order of thousand. In the turbulent mixing layer, the amount of product in the gaseous layer is found to be 20 – 50% more than that in a liquid shear layer, indicating that diffusion plays an important role in turbulent mixing of high Reynolds number flows. Some models of turbulent transport and mixing take no explicit account of molecular transport [37–39] and are, therefore, incapable of addressing Schmidt-number effects. In these models, molecular diffusion is neglected in comparison with turbulent diffusion and transport and mixing are modeled as separate processes. Statistics of conserved-scalar fields indicate that the scalar mixing region extends further into the feed streams than does the momentum mixing region, suggesting enhanced transport of scalars over momentum [28, 33].

‘Flip’ experiments have been performed for chemical reactions in the shear layer [17, 26, 28, 36]. In a flip experiment, the velocities at the inlet are kept fixed, but the given pair of reactant compositions are exchanged. At conditions just past the mixing transition, the chemical-product concentration profiles at high- and low-stoichiometric ratios are symmetric and the average concentration of mixed-fluid is uniform across the layer [17]. However, when the layer is fully developed, the scalar field evolves to an asymptotic state: the chemical-product concentration profiles from the flip experiment develop modest asymmetries, and the average mixed-fluid concentration develops a small variation across the layer. This change is however less than that observed in gases. It has been found that the amount of chemical product formed decreases as the Reynolds number increases [35, 36].

## 2.4 The three-dimensional evolution of the mixing layer

In addition to the primary two-dimensional vortical structures, it has long been observed that the plane free shear layer also contains a well organized array of streamwise vortices that superimpose onto spanwise eddies [40,41]. Results have shown that the streamwise structures first form in the braided region, a region connecting adjacent spanwise vortices that lacks significant spanwise vorticity and are dominated by large-scale strain [40–43]. The existence of counter-rotating streamwise vortices connecting the primary spanwise rollers were found. Lasheras and Choi [42] have given the following explanation for the qualitative evolution of the layer.

1. The two-dimensional shear instability develops, forming concentrated regions of two-dimensional spanwise vortex tubes.
2. Under the effect of the positive strain created by the spanwise vortex tubes, the vorticity existing in the braids is stretched, leading to the formation of vortex tubes whose axes align with the direction of maximum positive strain. During the formation of the streamwise vortex tubes, the spanwise vortices maintain their two-dimensionality, suggesting an almost uncoupled development of both two- and three-dimensional instabilities.
3. Coupling effects occur and the vortex tubes further interact with the spanwise vortex tubes inducing on their axes a wavy undulation of the same wavelength, but phase shifted  $180^\circ$  with respect to the perturbation.
4. The vorticity in the layer organizes into a complex topography of vortex tubes composed of an array of spanwise vortices tangled with counter-rotating pairs of axial vortices. The complex vorticity field further develops additional instabilities such as pairings, tearing, and amalgamation among the spanwise vortex tubes, and a much more complicated topography of the vorticity field is achieved.

The effects of velocity ratio on the near-field generation and development of three-dimensionality have also been investigated [44]. The mixing layer three-dimensionality is strongest with the lowest velocity ratio. The amount of stretching in the braided regions due to spanwise vortical structures is affected by velocity ratio. As the velocity ratio decreases (velocity difference increases), stronger spanwise rollers are generated which increase the amount of stretching in the braided regions and hence the streamwise vorticity is amplified.

The most extensive set of direct numerical simulations of temporally evolving mixing layers have been reported by Rogers and Moser [43, 45, 46]. These simulations have yielded complete details of the mixing layer structure and dynamics, starting from the formation of the initial spanwise vortex rollup leading into the evolution of the mixing layer up to the third pairing.

## 2.5 Summary

To date, there has been extensive work, both experimental and numerical, in the areas of two- and three-dimensional turbulent mixing layers using a single splitter plate configuration. Effects of varying the velocity ratio, density ratio, initial conditions and Reynolds numbers on the behavior of the mixing layer have been well documented. Numerical data have compared well with many of the experimental results, both qualitatively and quantitatively [24, 27, 30].

The intent of the present work is to look at the mixing layer in a reactor configuration with two splitter plates. The channel-flow reactor configuration has been chosen for DNS of the turbulent flow at moderate Reynolds-Schmidt numbers. From these simulations, it is possible to extract all relevant velocity and scalar statistics needed for detailed model validation. Indeed, DNS is the only method by which the small-scale processes of turbulent transport can be captured and studied. The full Navier-Stokes equations will

be used in the numerical simulations. The following chapter discusses the theoretical formulation of a three-dimensional flow and numerical implementation of the current work. In subsequent chapters, results are presented for two- and three-dimensional flows in the reactor.

## CHAPTER 3 MATHEMATICAL FORMULATION

In this chapter, a mathematical model for flow in a rectangular geometry is presented. The Navier-Stokes equations are presented in conservative three-dimensional form. A time-marching method which employs an artificial compressibility formulation is presented for transient solutions using a dual-time stepping technique. Finite difference schemes are used to discretize the equations. Appropriate boundary conditions are presented for flow in a rectangular reactor. Final comments address the different numerical parameters for two- and three-dimensional flows.

### 3.1 Governing equations

The motion of a constant density fluid is governed by the incompressible Navier-Stokes equations [47]. The governing equations in vector notation are

$$\nabla \cdot \mathbf{u} = 0 \quad (3.1)$$

$$\frac{\partial \mathbf{u}}{\partial t} + \mathbf{u} \cdot \nabla \mathbf{u} = -\nabla p + \nabla (\nu \nabla \mathbf{u}) \quad (3.2)$$

where  $\mathbf{u}$  is the velocity field,  $p$  is a modified pressure that accounts for the density, and  $\nu$  is the kinematic viscosity.

The advection of a passive scalar is important in many natural and engineering settings. The concentration of such a substance is of interest in the transport and mixing processes in turbulent shear flows. The scalar transport equation is included

which expresses the conservation of a passive property,  $\phi$ :

$$\frac{\partial \phi}{\partial t} + \mathbf{u} \cdot \nabla \phi = \nabla (\mathcal{D} \nabla \phi) \quad (3.3)$$

The property  $\phi$  is passive in that it is influenced by the flow without itself having any influence on the flow.

The conservative form of the Navier-Stokes equations in a Cartesian coordinate system  $(x, y, z)$  is

$$\frac{\partial Q}{\partial t} + \frac{\partial E}{\partial x} + \frac{\partial F}{\partial y} + \frac{\partial G}{\partial z} = \frac{\partial E_v}{\partial x} + \frac{\partial F_v}{\partial y} + \frac{\partial G_v}{\partial z} \quad (3.4)$$

where

$$Q = \begin{pmatrix} 0 \\ u \\ v \\ w \\ \phi \end{pmatrix} \quad E = \begin{pmatrix} u \\ u^2 + p \\ uv \\ uw \\ u\phi \end{pmatrix} \quad F = \begin{pmatrix} v \\ uv \\ v^2 + p \\ vw \\ v\phi \end{pmatrix} \quad G = \begin{pmatrix} w \\ uw \\ vw \\ w^2 + p \\ w\phi \end{pmatrix}$$

$$E_v = \nu \begin{pmatrix} 0 \\ \partial u / \partial x \\ \partial v / \partial x \\ \partial w / \partial x \\ \partial \phi / \partial x \end{pmatrix} \quad F_v = \nu \begin{pmatrix} 0 \\ \partial u / \partial y \\ \partial v / \partial y \\ \partial w / \partial y \\ \partial \phi / \partial y \end{pmatrix} \quad G_v = \nu \begin{pmatrix} 0 \\ \partial u / \partial z \\ \partial v / \partial z \\ \partial w / \partial z \\ \partial \phi / \partial z \end{pmatrix}$$

In this form,  $Q$  is a vector of the conservative dependent variables;  $E, F, G$ , are the conservative flux vectors; and  $E_v, F_v, G_v$  are the 'viscous' flux vectors comprising the shear stresses.

The Navier-Stokes equations form a set of parabolic-elliptic partial differential equations [48, pp. 17-33]. The solution of Eqs. (3.4) involves solving for the dependent variables,  $p, u, v, w$  and  $\phi$ . Due to the incompressible nature of the formulation, the

continuity equation is decoupled from the momentum equations. The following section discusses a way to couple the governing equations and proceed toward a numerical solution. The remainder of this chapter focuses on the numerical formulation of the governing equations.

### 3.2 Time-marching methods

Density-based methods were developed as time-marching schemes for the compressible form of the Navier-Stokes equations [49]. The compressible equations are coupled due to the presence of the full complement of primitive variables in the continuity equation. Originally, time-marching techniques were inefficient for solving low speed flows due to poor convergence. The difference between time scales associated with acoustic speeds and particle velocities resulted in the solution of a stiff matrix. The problem of poor convergence was alleviated by the use of preconditioning techniques that aided in exercising control over the disparities in the eigenvalues [50].

The artificial compressibility method is a special case of preconditioning for incompressible flows [51]. It permits the use of a density-based method to obtain the solution for incompressible flow fields by altering the continuity equation. Regardless of the particle velocity, the acoustic speeds can be chosen similar in magnitude. The result is improved convergence rates of the time-marching scheme. In a steady-state analysis, the artificial compressibility term vanishes, thereby restoring the true equations (§3.2.2). The method is very robust and efficient for solving the Navier-Stokes equations over a wide range of flow regimes.

In order to simulate unsteady fluid dynamic processes, a dual-time stepping technique is utilized [52, 53]. The dual-time stepping method incorporates a ‘pseudo’ time into the transient equations, which serves the purpose of iterating towards a converged solution. By using an implicit time discretization, the nature of the method does not impose

restrictions to small physical time steps. Hence, larger time steps may be used while still preserving temporal accuracy. The application of dual-time stepping is presented in §3.2.3. The following discussion explains how the governing equations are modified using a new set of dependent variables (§3.2.1) and preconditioning techniques (§3.2.2). The dual-time stepping method is implemented in §3.2.3 to solve transient flow problems.

### 3.2.1 The dependent variables

The choice of dependent variables when solving the governing equations is arbitrary. However, an appropriate choice can easily transform the equations for use with certain numerical techniques. Combining preconditioning techniques with time-marching methods requires a time derivative in all equations. In addition, it is essential that the governing equations are coupled. These factors are the motivations for the following choice.

A new set of dependent variables couple the governing equations and incorporate a time derivative into the continuity equation. The preference is to use a viscous variable set,  $Q_v$ , where the variables are identical to the quantities in the diffusion terms. The vector  $Q_v$  includes the full set of primitive variables

$$Q_v = (p, u, v, w, \phi)^T \quad (3.5)$$

and is incorporated into the system of equations using the chain rule

$$\frac{\partial Q}{\partial Q_v} \frac{\partial Q_v}{\partial t} + \frac{\partial E}{\partial x} + \frac{\partial F}{\partial y} + \frac{\partial G}{\partial z} = \frac{\partial E_v}{\partial x} + \frac{\partial F_v}{\partial y} + \frac{\partial G_v}{\partial z} \quad (3.6)$$

Overall, the equations above have the same form as Eqs. (3.4) but an additional term is present, the Jacobian matrix  $\partial Q/\partial Q_v$ . Computing the matrix results in the following

equation, where  $\partial Q/\partial Q_v$  has been replaced with the notation  $\Gamma$

$$\Gamma = \begin{pmatrix} 0 & 0 & 0 & 0 & 0 \\ 0 & 1 & 0 & 0 & 0 \\ 0 & 0 & 1 & 0 & 0 \\ 0 & 0 & 0 & 1 & 0 \\ 0 & 0 & 0 & 0 & 1 \end{pmatrix} \quad (3.7)$$

### 3.2.2 Preconditioning technique

The new set of dependent variables couples the incompressible form of the governing equations. However, a time derivative of pressure is added to the continuity equation. The true transient formulation of the equations is restored when the time derivative is multiplied by the matrix  $\Gamma$ . The form of Eqs. (3.6) can conveniently be solved for steady-state solutions of the equations using preconditioning. The artificial compressibility method [51] is a preconditioning technique used to modify the continuity equation to include an artificial compressibility term that vanishes at steady-state. In this manner, the physical time is replaced with a ‘pseudo’ time  $\tau$  and matrix  $\Gamma$  is redefined as a preconditioning matrix  $\Gamma_p$

$$\Gamma_p = \begin{pmatrix} 1/\beta & 0 & 0 & 0 & 0 \\ 0 & 1 & 0 & 0 & 0 \\ 0 & 0 & 1 & 0 & 0 \\ 0 & 0 & 0 & 1 & 0 \\ 0 & 0 & 0 & 0 & 1 \end{pmatrix} \quad (3.8)$$

where  $\beta$  is the artificial compressibility parameter. The value of  $\beta$  is chosen such that the eigenvalues are approximately the same order of magnitude for efficient convergence [54, pp. 661–665], [52].

The formulation can now be used for steady-state solutions by iterating in pseudo-

time. A solution is converged when

$$\Gamma_p \frac{\partial Q_v}{\partial \tau} \rightarrow 0 \quad (3.9)$$

Therefore, as the limit in pseudo-time becomes large, steady-state is reached.

### 3.2.3 Dual-time stepping procedure

The artificial compressibility formulation produces a transformation of Eqs. (3.4) that is only valid for steady-state solutions. Time accuracy is recovered by combining the artificial compressibility formulation with a dual-time stepping technique. A pseudo-time derivative is included with the physical time derivative in Eqs. (3.6)

$$\Gamma_p \frac{\partial Q_v}{\partial \tau} + \Gamma \frac{\partial Q_v}{\partial t} + \frac{\partial}{\partial x}(E - E_v) + \frac{\partial}{\partial y}(F - F_v) + \frac{\partial}{\partial z}(G - G_v) = 0 \quad (3.10)$$

The new formulation requires an additional inner level of iterations for the solution at each time level. The derivative  $\partial Q_v / \partial \tau$  is marched in pseudo-time, which is the inner iterative process, until a converged solution is reached in physical time.

## 3.3 Numerical formulation

The numerical formulation is presented by applying a coordinate transformation to the equations (§3.3.1) after which the equations are discretized using explicit time differencing for the pseudo-time and implicit time differencing for the physical time. Second order central differencing is used throughout for all spatial terms. The explicit Runge-Kutta method for the pseudo-time is presented in §3.3.4, and the entire formulation is closed with a discussion of the initial and boundary conditions in §3.4. The numerical code used in this research was originally developed by Dr. Jinzhang Feng (formerly at Pennsylvania State University) and has been modified to accommodate the requirements of the work herein.

### 3.3.1 Coordinate transformation

A general formulation of Eq. (3.10) is achieved by transforming the Cartesian coordinate system to a generalized coordinate system [54, pp. 338–341], [55, Ch. 9]. The physical domain  $(x, y, z)$  is mapped to a computational domain of independent variables  $(\xi, \eta, \zeta)$ . The new rectangular coordinate system is computationally easier to solve, especially if the physical domain is a complicated geometry. The generalized system is also advantageous for nonuniform grid spacing in regions where large gradients are expected.

The transformation requires a nonsingular mapping between the two coordinate systems to preserve the characteristics of the partial differential equation. Provided that the Jacobian is nonzero, i.e.,

$$J = \frac{\partial(\xi, \eta, \zeta)}{\partial(x, y, z)} = \begin{pmatrix} \xi_x & \xi_y & \xi_z \\ \eta_x & \eta_y & \eta_z \\ \zeta_x & \zeta_y & \zeta_z \end{pmatrix} \quad (3.11)$$

the mapping is successful [54, p. 25]. The subscripts  $x, y, z$  refer to partial derivatives of the generalized coordinates.

The chain rule is used to transform the partial differential equations (Eqs. 3.10) into equations that can be solved in the computational domain. Dividing the entire equation set by the Jacobian and rearranging terms forms the generalized, conservative equation.

$$\Gamma_p \frac{\partial \hat{Q}_v}{\partial \tau} + \Gamma \frac{\partial \hat{Q}_v}{\partial t} + \frac{\partial}{\partial \xi}(\hat{E} - \hat{E}_v) + \frac{\partial}{\partial \eta}(\hat{F} - \hat{F}_v) + \frac{\partial}{\partial \zeta}(\hat{G} - \hat{G}_v) = 0 \quad (3.12)$$

The generalized, conservative vectors are denoted with a caret,  $\hat{\cdot}$ , where,  $\hat{Q}_v = Q_v/J$  and  $\hat{E}$ ,  $\hat{F}$  and  $\hat{G}$  are

$$\hat{E} = \frac{1}{J} \begin{pmatrix} U \\ uU + \xi_x p \\ vU + \xi_y p \\ wU + \xi_z p \\ U\phi \end{pmatrix} \quad \hat{F} = \frac{1}{J} \begin{pmatrix} V \\ uV + \eta_x p \\ vV + \eta_y p \\ wV + \eta_z p \\ V\phi \end{pmatrix} \quad \hat{G} = \frac{1}{J} \begin{pmatrix} W \\ uW + \zeta_x p \\ vW + \zeta_y p \\ wW + \zeta_z p \\ W\phi \end{pmatrix}$$

where

$$U = u\xi_x + v\xi_y + w\xi_z$$

$$V = u\eta_x + v\eta_y + w\eta_z$$

$$W = u\zeta_x + v\zeta_y + w\zeta_z$$

The new contravariant velocity components  $U, V, W$  are in the directions of the transformed coordinates  $\xi, \eta, \zeta$ , respectively. The generalized viscous flux vectors are written in terms of vector  $Q_v$ , where

$$\begin{aligned}\hat{E}_v &= \frac{\nu}{J} \Gamma \left[ (\nabla\xi \cdot \nabla\xi) \frac{\partial(J\hat{Q}_v)}{\partial\xi} + (\nabla\xi \cdot \nabla\eta) \frac{\partial(J\hat{Q}_v)}{\partial\eta} + (\nabla\xi \cdot \nabla\zeta) \frac{\partial(J\hat{Q}_v)}{\partial\zeta} \right] \\ \hat{F}_v &= \frac{\nu}{J} \Gamma \left[ (\nabla\eta \cdot \nabla\xi) \frac{\partial(J\hat{Q}_v)}{\partial\xi} + (\nabla\eta \cdot \nabla\eta) \frac{\partial(J\hat{Q}_v)}{\partial\eta} + (\nabla\eta \cdot \nabla\zeta) \frac{\partial(J\hat{Q}_v)}{\partial\zeta} \right] \\ \hat{G}_v &= \frac{\nu}{J} \Gamma \left[ (\nabla\zeta \cdot \nabla\xi) \frac{\partial(J\hat{Q}_v)}{\partial\xi} + (\nabla\zeta \cdot \nabla\eta) \frac{\partial(J\hat{Q}_v)}{\partial\eta} + (\nabla\zeta \cdot \nabla\zeta) \frac{\partial(J\hat{Q}_v)}{\partial\zeta} \right]\end{aligned}$$

### 3.3.2 Spatial discretization

The convective and viscous fluxes are second order accurate and are centrally differenced. The discretization for the convective terms are shown here.

$$\begin{aligned}\frac{\partial\hat{E}}{\partial\xi} &= \frac{\hat{E}_{i+1} - \hat{E}_{i-1}}{2\Delta\xi} \\ \frac{\partial\hat{F}}{\partial\eta} &= \frac{\hat{F}_{j+1} - \hat{F}_{j-1}}{2\Delta\eta} \\ \frac{\partial\hat{G}}{\partial\zeta} &= \frac{\hat{G}_{k+1} - \hat{G}_{k-1}}{2\Delta\zeta}\end{aligned}$$

where  $i, j, k$  represent the  $x, y, z$  directions, respectively.

### 3.3.3 Implicit time discretization

The use of an implicit time scheme instead of an explicit scheme for the physical time step offers computational advantages. The artificial compressibility parameter is

ill-conditioned when  $\beta$  is large because  $1/\beta$  approaches zero. An implicit approach enables the preconditioning matrix to be inverted and removes the singularity. Another advantage is that implicit schemes are inherently stable. Therefore, it is possible to choose larger time steps and improve numerical convergence rates of the discretized equations.

The time derivatives of Eqs. (3.12) are implicitly discretized according to the significance of each term. The pseudo-time derivative is discretized using first order, finite-differencing, which is satisfactory for convergence. The physical time derivative uses 3-point, second order, finite-differencing for higher temporal accuracy [54, pp. 45–53]. Discretizing the time derivatives for an implicit formulation gives

$$\frac{\partial \hat{Q}_v}{\partial \tau} = \frac{\hat{Q}_v^{k+1} - \hat{Q}_v^k}{\Delta \tau} \quad (3.13)$$

$$\frac{\partial \hat{Q}_v}{\partial t} = \frac{3\hat{Q}_v^{n+1} - 4\hat{Q}_v^n + \hat{Q}_v^{n-1}}{2\Delta t} \quad (3.14)$$

where  $k$  is the pseudo-time level, and  $n$  is the physical time level. Because the implicit assumption requires the knowledge of  $\hat{Q}_v^{n+1}$ , the term is approximated by  $\hat{Q}_v^{k+1}$ . Equations (3.13–3.14) are substituted into Eqs. (3.12), after which, the equations are rearranged and cast in delta form

$$\left( \Gamma_p + \frac{3}{2} \frac{\Delta \tau}{\Delta t} \Gamma \right) \Delta \bar{Q}_v = -\Delta \tau \left[ \Gamma \left( \frac{3\hat{Q}_v^k - 4\hat{Q}_v^n + \hat{Q}_v^{n-1}}{2\Delta t} \right) + \bar{R}^n \right] \quad (3.15)$$

where

$$\bar{R}^n = \left\{ \frac{\partial(\hat{E} - \hat{E}_v)}{\partial \xi} + \frac{\partial(\hat{F} - \hat{F}_v)}{\partial \eta} + \frac{\partial(\hat{G} - \hat{G}_v)}{\partial \zeta} \right\}^n$$

and

$$\Delta \bar{Q}_v = \hat{Q}_v^{k+1} - \hat{Q}_v^k$$

Equations (3.15) define the inner iterations,  $k$ , for the solution at time level  $n + 1$ . Convergence is obtained when  $\Delta \bar{Q}_v \rightarrow 0$ , satisfying the unsteady Navier-Stokes equations. Note that Eqs. (3.15) reduce to the pseudo-time formulation for the steady-state problem when  $\Delta t \rightarrow \infty$ .

### 3.3.4 Runge-Kutta method

The numerical formulation of the governing equations is completed by using central differences to accomplish the discretization of the spatial derivatives. An efficient scheme is desired to solve the discretized equations. A two-stage, explicit, Runge-Kutta scheme is used to integrate the Navier-Stokes equations in pseudo-time [56]. To employ the numerical scheme, Eqs. (3.15) are rewritten in a more general form

$$\hat{Q}_v^{k+1} - \hat{Q}_v^k = -\Delta\tau\mathcal{S}^{-1} \left[ \Gamma \left( \frac{3\hat{Q}_v^k - 4\hat{Q}_v^n + \hat{Q}_v^{n-1}}{2\Delta t} \right) + \bar{R}^n \right] \quad (3.16)$$

$$\mathcal{S}^{-1} = \left( \Gamma_p + \frac{3}{2} \frac{\Delta\tau}{\Delta t} \Gamma \right)^{-1}$$

The integration in pseudo-time ends with the evaluation of  $\hat{Q}_v^{k+1}$ . An intermediate step, denoted by the superscript \* is used to calculate the provisional values of  $Q$

$$Q_v^* = \hat{Q}_v^k - \alpha\Delta\tau\mathcal{S}^{-1} \left[ \Gamma \frac{\Delta\tilde{Q}_v}{2\Delta t} + \left( \frac{\partial\hat{E}}{\partial\xi} + \frac{\partial\hat{F}}{\partial\eta} + \frac{\partial\hat{G}}{\partial\zeta} \right)^k + \text{VIS} + \text{AD} \right]$$

$$\hat{Q}_v^{k+1} = \hat{Q}_v^k - \Delta\tau\mathcal{S}^{-1} \left[ \Gamma \frac{\Delta\tilde{Q}_v}{2\Delta t} + \left( \frac{\partial\hat{E}}{\partial\xi} + \frac{\partial\hat{F}}{\partial\eta} + \frac{\partial\hat{G}}{\partial\zeta} \right)^* + \text{VIS} + \text{AD} \right] \quad (3.17)$$

where

$$\begin{aligned} \Delta\tilde{Q}_v &= 3\hat{Q}_v^k - 4\hat{Q}_v^n + \hat{Q}_v^{n-1} \\ \text{VIS} &= \left( \frac{\partial\hat{E}_v}{\partial\xi} + \frac{\partial\hat{F}_v}{\partial\eta} + \frac{\partial\hat{G}_v}{\partial\zeta} \right)^n \\ \text{AD} &= \left( \frac{\epsilon_{ex}}{8\Delta\tau} \frac{\partial^4\hat{Q}_v}{\partial\xi^4} + \frac{\epsilon_{ey}}{8\Delta\tau} \frac{\partial^4\hat{Q}_v}{\partial\eta^4} + \frac{\epsilon_{ez}}{8\Delta\tau} \frac{\partial^4\hat{Q}_v}{\partial\zeta^4} \right)^n \end{aligned} \quad (3.18)$$

The constant  $\alpha$  has a value of 1/2 in the two-stage scheme. Equation (3.18) is a fourth order dissipative term, with artificial dissipation coefficients  $\epsilon_{ex}$ ,  $\epsilon_{ey}$ ,  $\epsilon_{ez}$ .

The convective fluxes are evaluated at both stages of the integration scheme, while the viscous fluxes are evaluated only once in pseudo-time. The reason is that solving for the viscous terms in both stages can be computationally expensive when compared to the gain in convergence rate.

The last term of Eq. (3.17) represents artificial dissipation [57]. Fourth order dissipation is added to the discretized Navier-Stokes equations to damp out high wavenumbers and prevent odd-even splitting of the numerical solution. Similar to the viscous terms, the artificial dissipation terms are calculated only once in the Runge-Kutta cycle. A stability analysis of the scheme gives a limiting value of 0.3 for the artificial dissipation coefficients [58].

The local time step is calculated by comparing the convective and diffusive time steps in the Navier-Stokes equations. The convective time step is defined from the Courant-Friedrichs-Lewy (CFL) number. The CFL number is the ratio of the distance traveled by a discrete wave in a given time step to an incremental distance such as grid spacing. For a particular eigenvalue  $\lambda$  (i.e., the characteristic speed), in the flow direction  $\kappa$ , the CFL number is

$$\text{CFL} = \frac{\lambda_{\kappa} \Delta \tau}{\Delta \kappa} \quad (3.19)$$

The CFL number is kept constant to ensure every grid point converges at the same rate. The method has been proven to be effective and stable [58]. The local time step is defined as

$$\Delta \tau = \text{CFL} \frac{\Delta \xi + \Delta \eta + \Delta \zeta}{\sqrt{\lambda_{\xi \max}^2 + \lambda_{\eta \max}^2 + \lambda_{\zeta \max}^2}} \quad (3.20)$$

where  $\lambda_{\max}$  are the maximum eigenvalues in the  $\xi, \eta, \zeta$  directions.

The time step definition of Eq. (3.20) is compared to the diffusive time step, and the minimum of the two values is used at each grid point. The diffusive time step is defined by the von Neumann number  $\sigma$ , and represents the ratio of the viscous speed of a particle ( $\nu/\Delta \kappa$ ) to the convective speed ( $\Delta \kappa/\Delta \tau$ ).

$$\sigma = \frac{\nu \Delta \tau}{\Delta \kappa^2} \quad (3.21)$$

The stability of the Runge-Kutta scheme limits the magnitude of the CFL and  $\sigma$  numbers. The upper limit of the CFL and  $\sigma$  numbers for this explicit scheme are  $2\sqrt{2}$  and 0.3, respectively.

### 3.4 Mathematical and computational conditions

The presentation of the governing equations and the numerical formulations up to this point have been for a general solution of the Navier-Stokes equations for constant density. The equations are closed by specifying initial and boundary conditions. Typical initial conditions include defining the velocity field for the computational domain. Boundary conditions involve Dirichlet and Neumann conditions. From a computational viewpoint, there also exist conditions which must be satisfied to render a well-posed computational solution [59, p. 334]. These conditions will be addressed throughout the following discussions.

#### 3.4.1 Boundary conditions

The boundary-value problem involves specifying conditions along all boundaries of the physical and computational domains [48, p. 20]. One such example is the Dirichlet boundary condition for the velocity. The no-slip condition is implemented to account for viscous effects along solid surfaces. The fluid velocities at any wall must satisfy

$$u = u_{\text{wall}} \quad v = v_{\text{wall}} \quad (3.22)$$

The pressure condition is a Neumann boundary condition. It is formulated by applying the momentum equation in the direction normal to the surface after enforcing the no-slip condition,

$$\nabla p \cdot \hat{n} = \nu(\nabla^2 u + \nabla^2 v) \quad (3.23)$$

where  $\hat{n}$  is the normal direction.

The unsteady Navier-Stokes equations have been transformed into a mixed set of hyperbolic-parabolic equations by the artificial compressibility method. The formulation of the numerical inflow/outflow boundary conditions is analogous to the method of characteristics and consistent with time-marching schemes for (subsonic) compressible

flow. The number of numerical conditions specified at an inflow boundary is based on the number of positive eigenvalues that represent characteristics traveling into the domain [59, pp. 26–28]. The outflow boundary condition depends on the number of negative eigenvalues leaving the domain. It is common to specify the velocity field as an inflow condition and the static pressure as an outflow condition. The remaining unknown inflow/outflow conditions are extrapolated from known information within the computational domain.

For the passive scalars, the high speed stream has a concentration of 1.0 and the low speed streams have a concentration of 0.0 at the inlet. Since the scalar is conserved, the concentration of scalars in the domain must have a value  $0.0 \leq \phi \leq 1.0$ . At the walls, the scalar flux is made zero.

### 3.4.2 Initial condition

The initial-value problem is required for both steady-state and time-dependent formulations. Time-marching schemes require information regarding the flow field prior to the commencement of a simulation. Typically, the initial condition uses a specified velocity distribution. The velocity distribution should also satisfy conservation of mass (Eq. 3.1).

The steady-state formulation of §3.2.2 was developed for numerical convergence in pseudo-time. The time-marching ‘pseudo’ variable is not physical but has the same role as time in a transient problem. The pseudo-time derivative of Eq. (3.13) requires variable information at pseudo-time level  $k$  in order for the simulation to proceed to the first pseudo-time level  $k + 1$ . The transient formulation incorporates the dual-time stepping technique, requiring two initial conditions. Recall from §3.3.3 that the physical time was discretized using second order differencing. The implication is that information must be specified for two time levels,  $n - 1$  and  $n$ , to complete the initial-value problem.

An initial condition which is simple to implement is to specify the mass flow rate at

the inlet of the domain. The condition can be interpreted as the start-up of flow moving into a domain of quiescent fluid. After a converged simulation is obtained, the solution can be used as an initial condition for further simulations because a complete flow field distribution within the domain is known and provides better convergence. The initial condition also provides a well-posed computational condition. For different cases using the same flow domain, the inlet velocity profile can be modified to account for a new mass flow rate.

### 3.4.3 Computational parameters

The numerical algorithm is optimized by determining various parameters at the onset of the simulation. Such parameters include the numerical CFL and  $\sigma$  numbers, and the artificial dissipation coefficients  $\epsilon_{ex}, \epsilon_{ey}, \epsilon_{ez}$ . The effect of artificial dissipation on the solution was investigated and it was found that for the values cited in Table 3.1, artificial dissipation does not affect the numerical solution. However, it was necessary to add the artificial dissipation term in order to control the dissipation error. The stability criteria stated in §3.3.4 imposed upper bounds on the numerical validity of the parameters. Furthermore, two- and three-dimensional simulations do not necessarily utilize the same constants for the governing numerical parameters due to the increased complexity of the additional dimension. Table 3.1 summarizes the parameters used in the numerical schemes, which were determined to be most efficient for the nature of these computations.

	CFL	$\sigma$	$\epsilon_{ex}, \epsilon_{ey},$ $\epsilon_{ez}$
2-D	1.0	0.20	0.20
3-D	1.0	0.15	0.20

Table 3.1 Numerical parameters for two- and three-dimensional flows.

## CHAPTER 4 NUMERICAL SOLUTIONS OF FLOW IN 2-D REACTOR: VELOCITY AND VORTICITY

The focus of this chapter is to interpret the results of simulations in a two-dimensional reactor. Here the hydrodynamic evolution and the entrainment and mixing characteristics of the incompressible mixing layer are presented. A thorough understanding of the hydrodynamics is a prerequisite to the study of scalar mixing in such a flow. The effect of velocity ratio on the evolution of the mixing layer is discussed for a Reynolds number of 3000. The results shown here represent the solutions of a purely two-dimensional problem.

In §4.1, the geometry of the reactor is presented, followed by the discussion of initial and boundary conditions in §4.2. Section 4.3 discusses the grid used for the purposes of simulations. The two-dimensional mixing layer is discussed in detail in §4.4, followed by the comparison of statistical results for different velocity ratios in §4.5.

### 4.1 Geometry of reactor

The geometry for a simple two-dimensional mixing channel is shown in Fig. 4.1. The configuration is a planar channel of streamwise length  $L_c$  in which three horizontal inlet streams are separated by two splitter plates of equal length  $L_s$  to initiate mixing. The central stream velocity  $u_2$  is varied relative to the two outer stream velocities  $u_1$  to induce the development of the mixing layer. The Reynolds number is defined as  $Re = \bar{u}h/\nu$ , where  $\bar{u}$  is the average velocity of the three inlet streams,  $h$  is the height of channel in

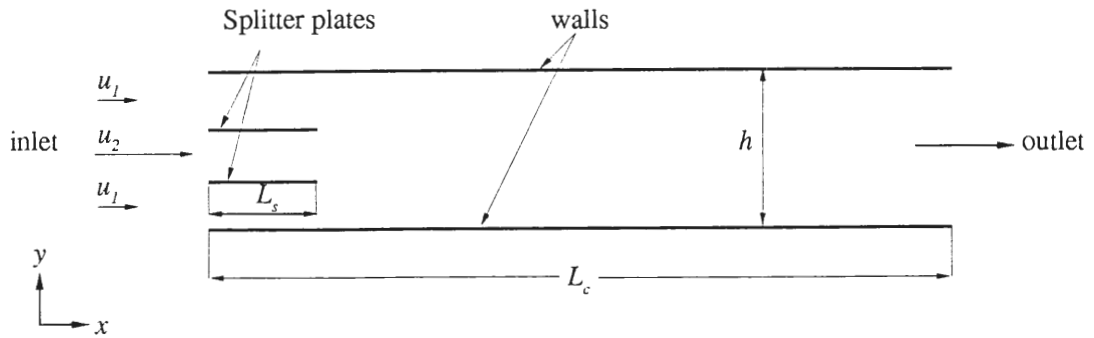


Figure 4.1 Schematic of planar mixing of three co-flowing streams in a symmetric channel.

the cross-stream direction and  $\nu$  is the kinematic viscosity. The fluid used for purposes of simulation is water. The dimensions of the channel are  $h=0.06$  m,  $L_c=1.0$  m,  $L_s=0.1$  m.

## 4.2 Initial and boundary conditions

As an initial condition, a plug velocity profile was provided at the channel inlet as well as at the inner grid points. Initializing the domain helped the residuals converge at a faster rate. At the channel walls and splitter plate walls, a no-slip boundary condition was imposed. At the inlet, velocity was specified while pressure was extrapolated from within the domain. At the channel exit, ambient pressure was specified and velocities were extrapolated from within the channel.

## 4.3 Computational performance

It is essential for a numerical simulation to adequately resolve flow regions where the gradients are largest. An example of such a case is viscous flow near solid surfaces where velocity gradients are important. A means for improving numerical resolution is

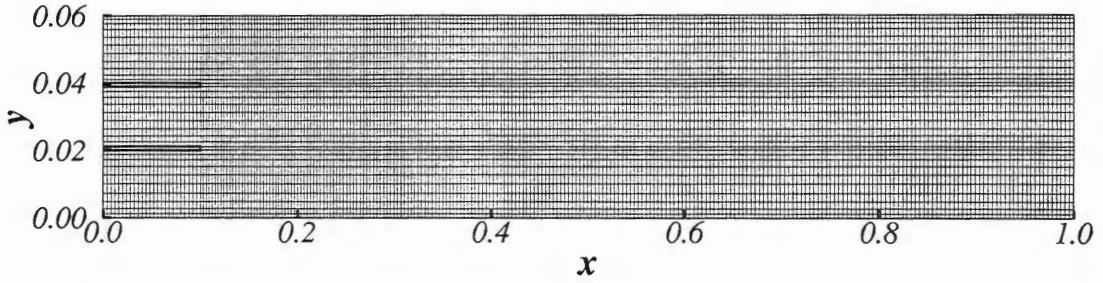


Figure 4.2 Grid for the two-dimensional reactor. Mesh is  $1025 \times 129$  grid points showing every 4th node in  $x$  and  $y$ .

by increasing the number of grid points and clustering the grid in regions of high gradients [55]. A rectangular grid was used in the numerical simulations with clustering close to the channel walls and splitter plate walls, as seen in Fig. 4.2. The grid was clustered to resolve the intricate details of the developing flow in the cross-stream direction. Numerical tests were performed to determine the grid size needed to resolve the flow field and to generate grid-independent solutions. Three different grid sizes were used for the purpose, viz.  $513 \times 65$ ,  $1025 \times 129$  and  $2049 \times 257$ . Based on the results, it was concluded to use a mesh of size  $1025 \times 129$  for the purpose of simulations. The grid aspect ratio  $\Delta x/\Delta y$  was maintained in the range of 1.5–2.5.

Convergence was assured by requiring the residuals of the numerical simulations to reduce to a small value such that the relative difference between successive iterations be smaller than  $10^{-7}$ . The residuals,  $\Delta R_Q$ , are defined as the change in the solution variables  $p$ ,  $u$ , or  $v$ , where

$$\Delta R_Q = \sqrt{\frac{\sum_{j=1}^{j_{max}} \sum_{i=1}^{i_{max}} (\Delta Q)^2}{(i_{max})(j_{max})}}$$

and  $i_{max}$  and  $j_{max}$  are the maximum number of grid points in the  $\xi$  and  $\eta$  directions, respectively. The time step for the transient simulations was calculated from the CFL criterion as discussed in Chapter 3:

## 4.4 The two-dimensional mixing layer

Transient simulations were performed of the two-dimensional mixing layer. The Reynolds number in the channel was maintained at 3000 and three different velocity ratios were used to study the evolution of the mixing layer. The velocity ratios used for the simulations were,  $r = 0.5, 0.3$  and  $0.25$ , where  $r = u_1/u_2$ . Results for the case with  $r = 0.5$  are discussed first, followed by comparison of results for the three velocity ratios in §4.5.

### 4.4.1 Characteristics of evolution of mixing layer (results for $r = 0.5$ )

Figure. 4.3 shows the instantaneous velocity vector plot ( $t = 53.94$  s). The splitter plate ends at  $x = 0.1$  m and the outer streams come in contact with the central stream. In the near-field region, beyond the trailing edge of the splitter plate, the mixing layer is undeveloped and a step-like velocity profile can be seen in Fig. 4.4. As the shear layers mix and merge further downstream, the velocity no longer shows the step profile. As the mixing layer grows and instability increases, the faster fluid particles in the far-field region are pushed in the downward and upward direction. For example, at  $x = 0.65$  m., the velocity vectors are directed downward while at  $x = 0.98$  m., the vectors are directed upward.

The pressure distribution in the channel is shown as a contour plot in Fig. 4.5. The pressure distribution is quite uniform in the channel without any sudden changes. It decreases to ambient pressure at the outlet, which is the boundary condition used. The dark and light patches in the plot correspond to the low and high velocities in the channel respectively. Figure. 4.6 shows the instantaneous  $u$ -contour plot. The contours appear smooth and unbroken initially. However, downstream of the splitter plate, the contours break up, due to instability. The high speed fluid is driven in the downward ( $x = 0.7$  m) direction and then upward ( $x = 0.8$  m), hinting that mixing has occurred.

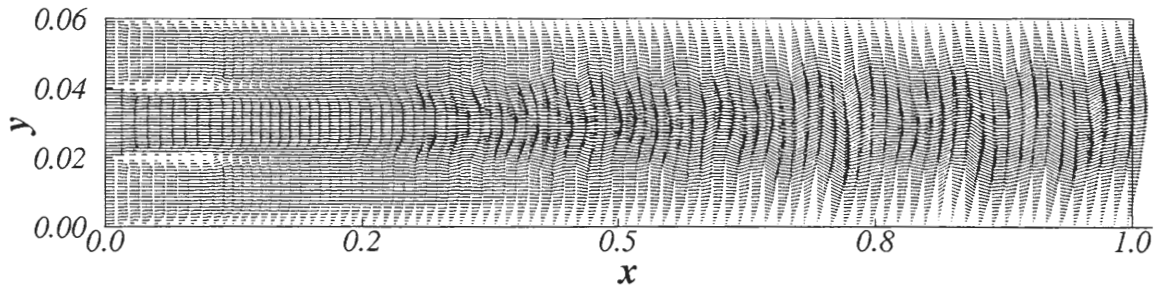


Figure 4.3 Instantaneous velocity vector plot at  $t = 53.94$  s, showing every 12th vector in  $x$  and 2nd vector in  $y$ ,  $Re = 3000$ ,  $r = 0.5$ .

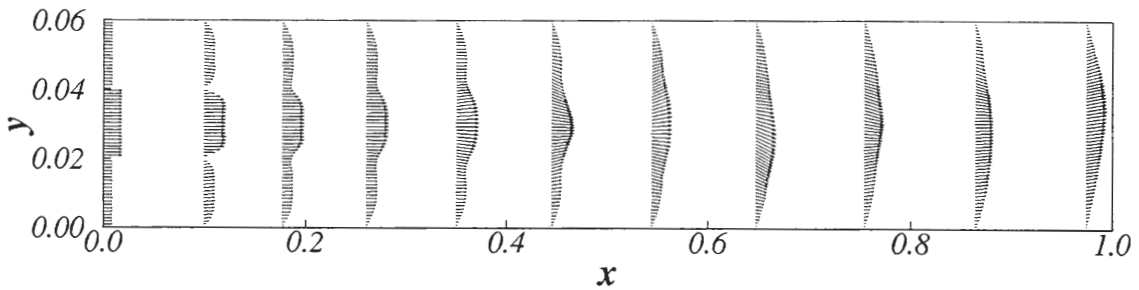


Figure 4.4 Instantaneous velocity vector plot at  $t = 53.94$  s, showing every 100th vector in  $x$  and 2nd vector in  $y$ ,  $Re = 3000$ ,  $r = 0.5$ .

The  $u$ -contour plot shows the presence of negative velocity at some parts of the domain. These negative velocities are very close to the wall and far downstream of the splitter plates. The negative velocity results from the entrainment process in which the fluid from outside the shear layer is brought into the shear layer. The  $v$ -contour plot in Fig. 4.7 shows that the velocity in the cross-stream direction is initially small downstream of the splitter plate, but later on, its strength increases, which confirms the earlier conclusion about the fluid particles being convected in the cross-stream direction downstream of the channel. Figure 4.8 shows the mean velocity contour in the streamwise direction, averaged over time. About 700 realizations were used to compute the average. The plot shows the spreading of the shear layer. Initially one can see the red band of fluid in the

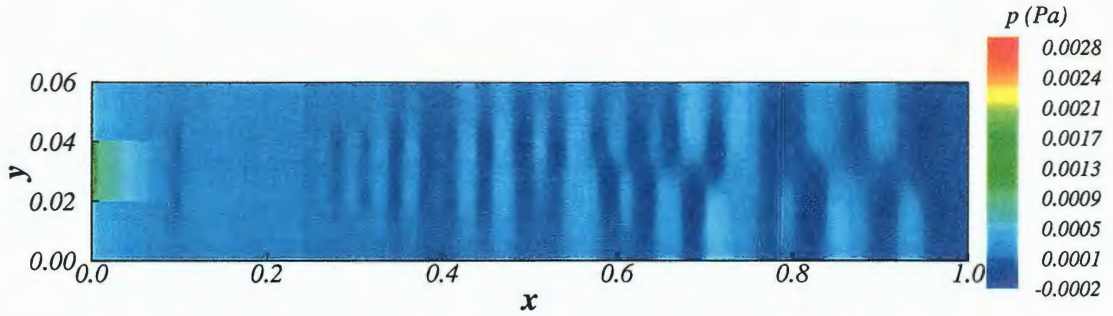


Figure 4.5 Instantaneous contour plot showing pressure distribution in the channel at  $t = 53.94$  s for  $Re = 3000$ ,  $r = 0.5$ .

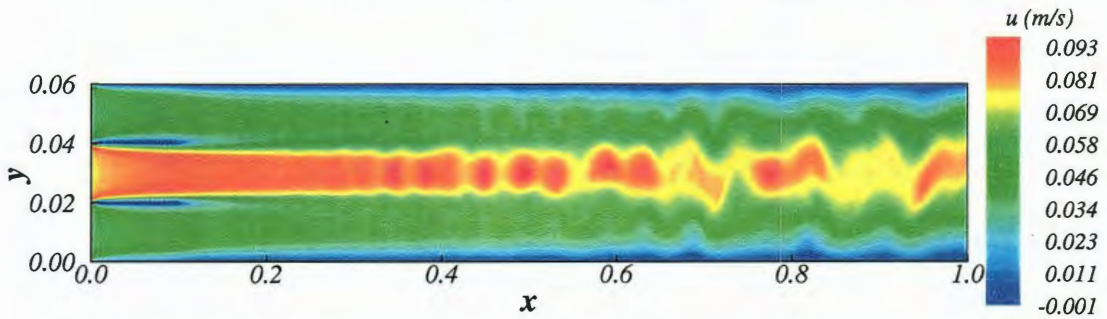


Figure 4.6 Instantaneous contour plot of  $u$ -velocity in the channel at  $t = 53.94$  s for  $Re = 3000$ ,  $r = 0.5$ .

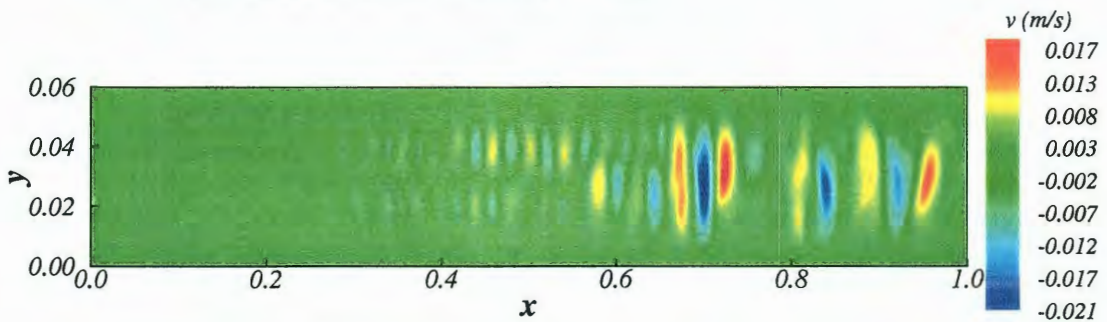


Figure 4.7 Instantaneous contour plot of  $v$ -velocity in the channel at  $t = 53.94$  s for  $Re = 3000$ ,  $r = 0.5$ .

central stream. However, downstream of the splitter plate, the faster fluid spreads into the outer streams. The mean velocity profiles, normalized by the velocity difference of the fast and slow streams are shown versus the cross-stream direction at five sections in the streamwise direction in Fig. 4.9. The initial step-like profile becomes smoother as the flow moves downstream and beyond  $x = 0.6$  m, the profiles fall almost on top of each other: the flow becomes fully developed.

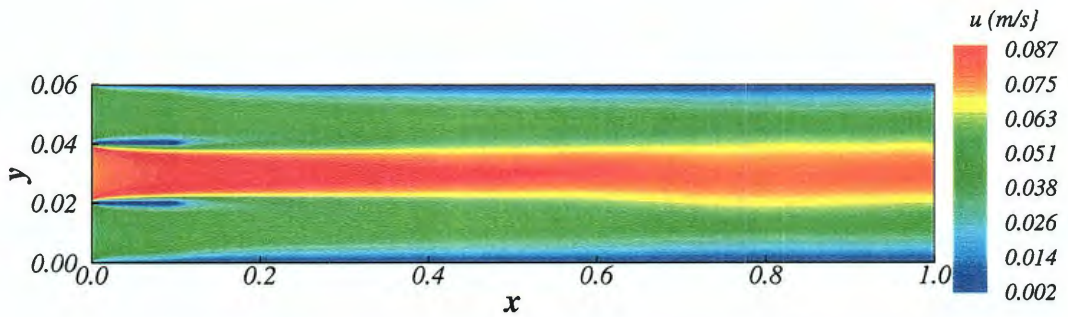


Figure 4.8 Time-averaged contour plot of streamwise velocity for  $Re = 3000$ ,  $r = 0.5$ .

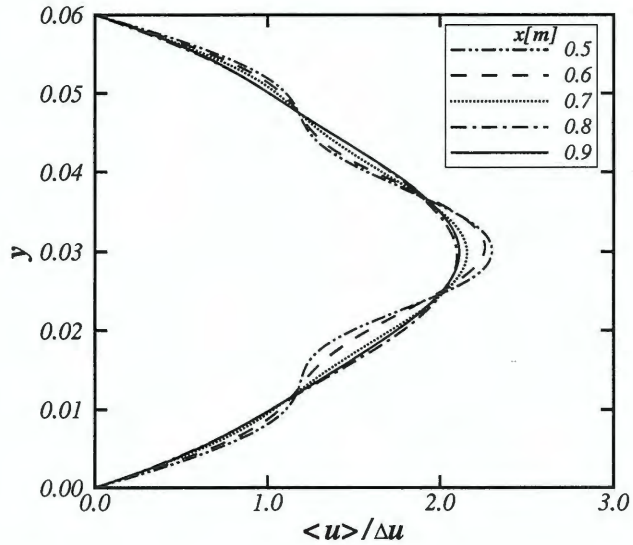


Figure 4.9 Normalized mean streamwise velocity at different streamwise locations for  $Re=3000$ ,  $r = 0.5$ .

The figures shown so far do not provide in depth information about the origin of instability and its propagation in the mixing layer. The plots do not provide evidence for the mechanism of growth of the mixing layer. In literature, the mixing layer is commonly described by means of vorticity. Hence the vorticity plots are presented next.

#### 4.4.2 Generation of instability and growth of mixing layer

An essential feature of turbulent flows is that they are irrotational, that is, they have non-zero vorticity. Vorticity  $\omega$  is the curl of the velocity.

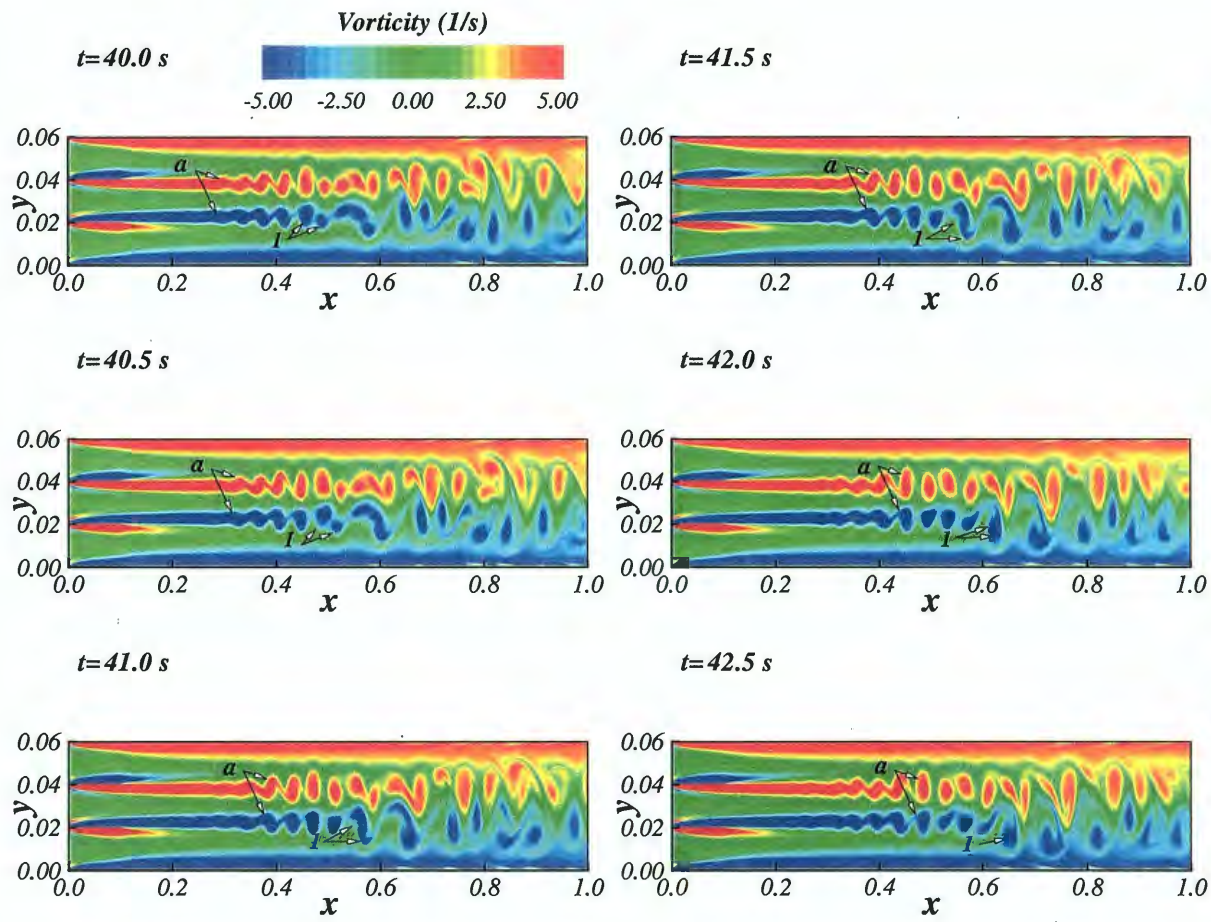
$$\omega = \nabla \times \mathbf{u}$$

In two-dimensional flow in the  $x$ - and  $y$ -directions, only the  $z$ -component of the vorticity vector is finite.

$$\omega_z = \frac{\partial v}{\partial x} - \frac{\partial u}{\partial y}$$

The time evolution of the vorticity field within the domain of the spatially developing shear layer is shown in Fig. 4.10 for  $r = 0.5$ , starting at  $t = 40$  s. The time interval between each frame is 0.5 seconds. An examination of this figure indicates that large vortical structures are created at the trailing edge of the splitter plate (marked as 'a') at  $t = 40$  s. These structures are caused by natural instabilities inherent in the flow. The instabilities are a consequence of the Kelvin–Helmholtz mechanism and constitute the dominating factors in developing the roll-up of coherent vortices [24]. The “cores” and “braids” of the vortex structures can be seen. The core is formed by the vortex structure itself and the braid is the thin connection between two vortex eddies. The vortex structures undergo pairing downstream of the splitter plate to form larger structures. From the figure a neighboring pair of vortices labeled ‘1’ can be followed as they rotate around each other. Following through the time sequence the eddies further coalesce to form a larger structure. The coalescence is termed as ‘pairing’, and is the dominant mode of interaction and principal mechanism for growth of the shear layer. The vorti-

Figure 4.10 Evolution of spanwise vorticity field for  $Re = 3000$ ,  $\tau = 0.5$ .



cal structures control the entrainment process and mixing mechanism within the layer. Also noteworthy is the development of the two vortices (labeled 'a') that initially shed and grow downstream of the plate. These vortices will also coalesce in time.

#### 4.5 Results for different velocity ratios.

Two-dimensional simulations are performed for three different velocity ratios of 0.5, 0.3 and 0.25, respectively. The Reynolds number for all three cases is 3000. Therefore, as the velocity ratio decreases,  $u_2$  increases and  $u_1$  decreases. Instantaneous vorticity contours for the three different velocity ratios are shown in Fig. 4.11. The common characteristics that are seen from the three plots are the two rows of vortical structures. The size of the vortical structures appears to grow larger as the velocity ratio decreases (i.e. the velocity difference across the shear layer increases). Also, the first vortex roll-up initiates closer to the trailing edge of the splitter plate as the velocity ratio decreases. The interaction between the two shear layers grows stronger as the velocity ratio decreases. The mean velocity profiles for cases,  $r=0.3$  and  $r=0.25$  are shown in Fig. 4.12 and Fig. 4.13 respectively. The mean velocity profiles depict the steep gradient in the layer due to the high and the low speed streams and this gradient increases as the velocity ratio decreases. Also for a particular velocity ratio, as the distance from the trailing edge of the splitter plate increases, the mean velocity gradient increases.

Figures 4.14, 4.15 and 4.16 show the normalized root mean square streamwise velocity  $u'_{rms}$  for the three cases at different streamwise locations. The fluctuations peak at a maximum intensity and as the streamwise distance increases, the peak intensity of fluctuations traverse from the center of the channel to the walls. Initially at  $x=0.5$  m, the profiles are undeveloped due to the influence of the fast central stream. As the downstream distance increases, the mixing is complete and turbulence due the walls develops, as can be seen from the  $u'_{rms}$  profiles at  $x=0.8$  and  $0.9$  m. The profiles at these

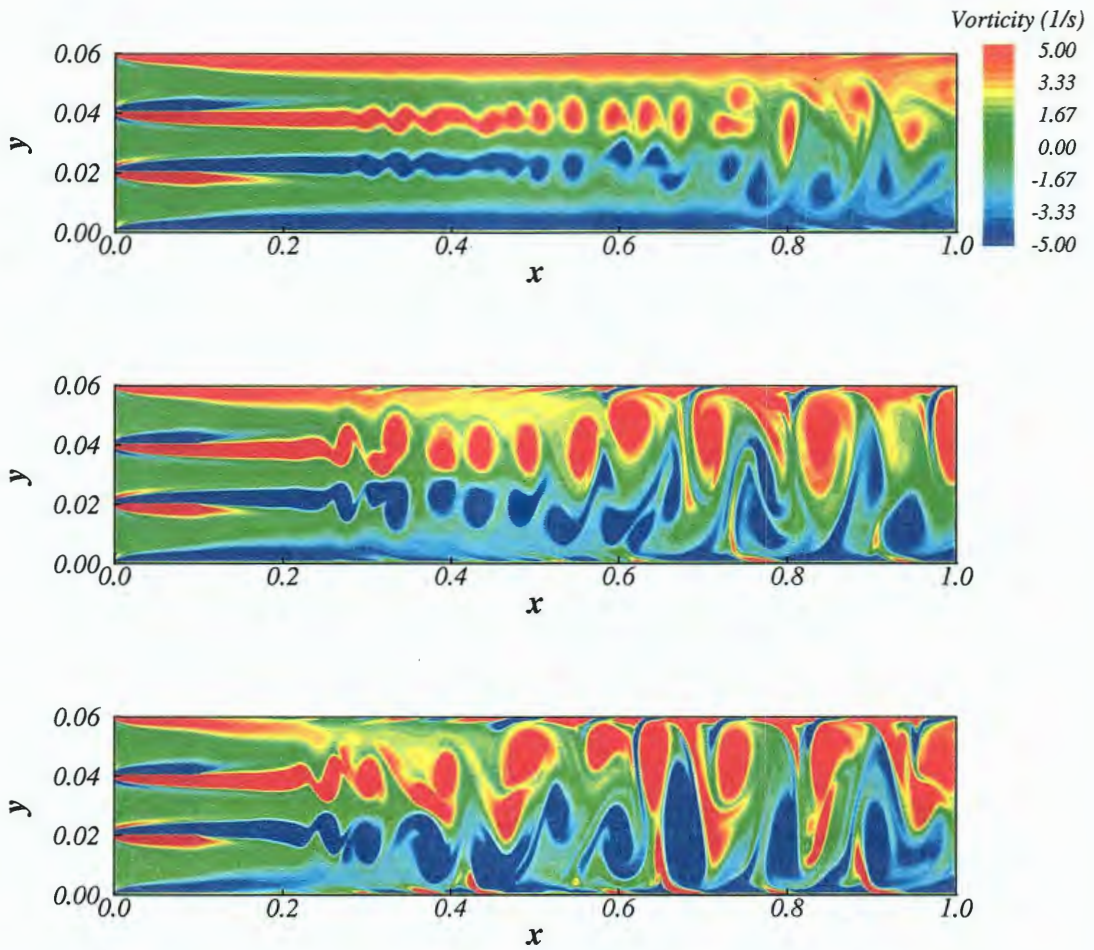


Figure 4.11 Instantaneous spanwise vorticity contour plot at  $t = 39.94$  s for  $Re = 3000$  and  $r = 0.5$ ,  $r = 0.3$  and  $r = 0.25$ .

two locations have their peak intensities close to the walls, indicating an almost fully developed turbulent profile. Similarly,  $v'_{rms}$  is shown in Fig. 4.17, 4.18 and 4.19. As the streamwise distance increases, the fluctuations increase indicating that downstream of the splitter plate mixing has occurred. Also the peak intensity of fluctuations is at the center of channel, where the two shear layers merge and mix. The values of  $v'_{rms}$  are as significant as  $u'_{rms}$ , which is a result of mixing occurring downstream of the splitter plate in the channel.

The Reynolds stresses for the three velocity ratios are shown in Figures 4.20, 4.21

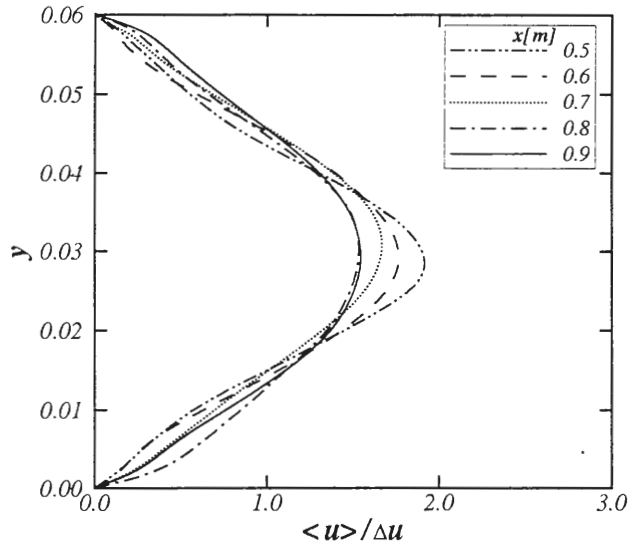


Figure 4.12 Normalized mean streamwise velocity at different streamwise locations for  $Re = 3000$ ,  $r = 0.3$ .

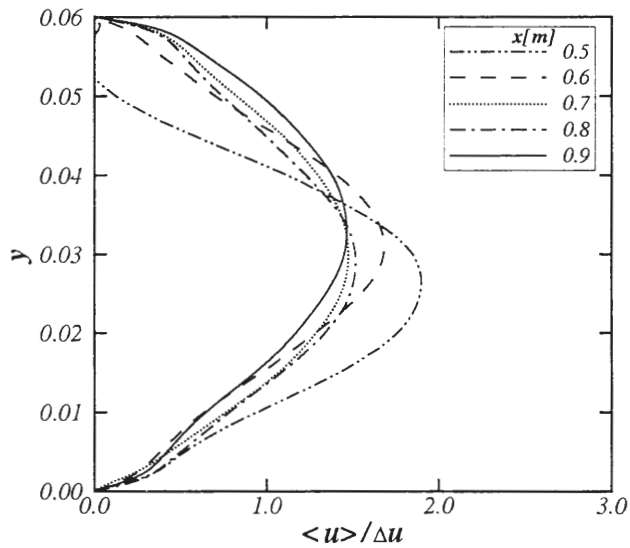


Figure 4.13 Normalized mean streamwise velocity at different streamwise locations for  $Re = 3000$ ,  $r = 0.25$ .

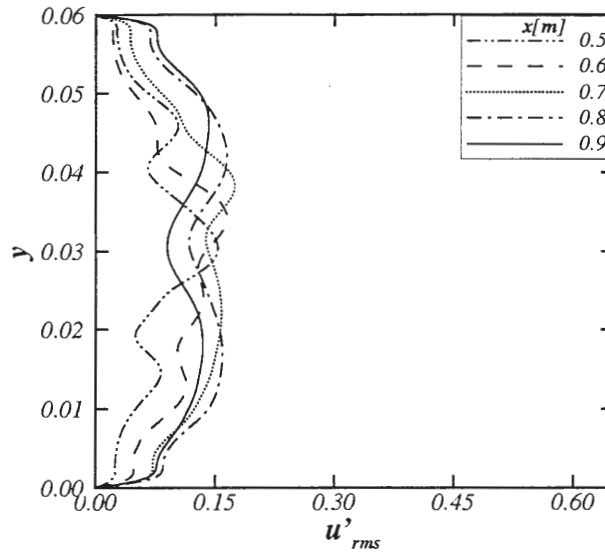


Figure 4.14 Normalized RMS streamwise velocity at different streamwise locations for  $Re = 3000$ ,  $r = 0.5$ .

and 4.22. The stresses are generated due to the fluctuating components of velocity  $u'_{rms}$  and  $v'_{rms}$ . The profiles are initially undeveloped, but as the streamwise distance increases, the profiles become developed. The shape of the stress profile follows that of the  $u'_{rms}$  profile with peak intensities close to wall for fully developed flow. At  $x=0.8$  m. and  $x=0.9$  m., the peak stresses lie at the same cross-stream location indicating fully developed flow.

The discussion on velocity, vorticity and statistics explained the mechanism of entrainment and merging of the shear layer. The data collected for statistical analysis was over two eddy turnover times. The following chapter presents the evolution of a passive scalar field in the mixing layer.

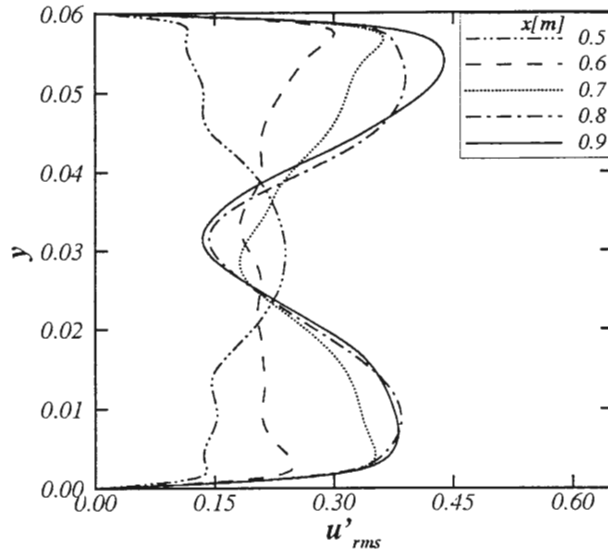


Figure 4.15 Normalized RMS streamwise velocity at different streamwise locations for  $Re = 3000$ ,  $r = 0.3$ .

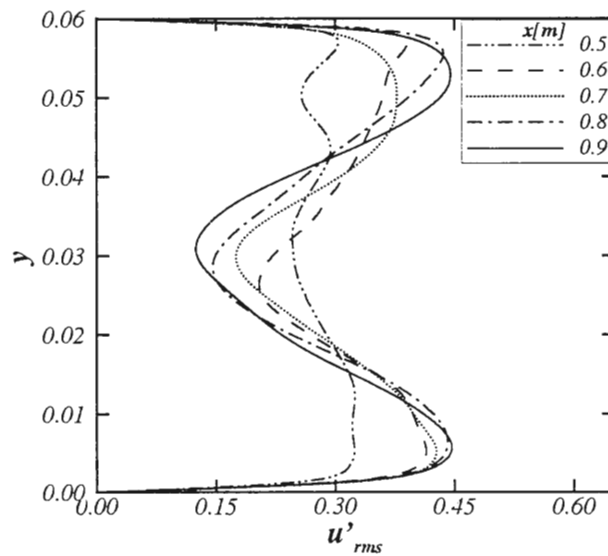


Figure 4.16 Normalized RMS streamwise velocity at different streamwise locations for  $Re = 3000$ ,  $r = 0.25$ .

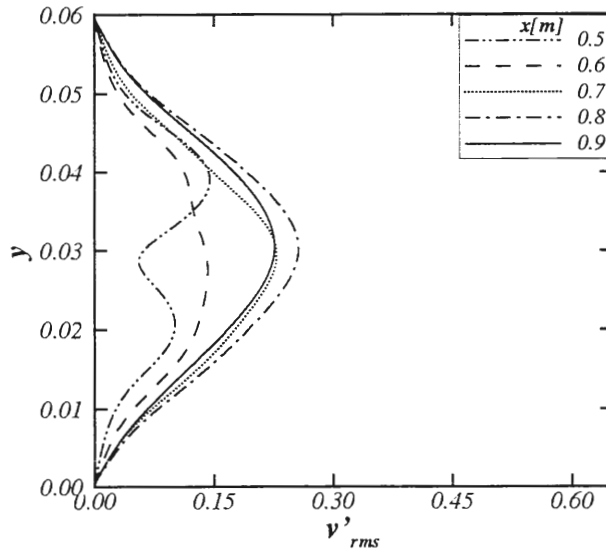


Figure 4.17 Normalized RMS cross-stream velocity at different streamwise locations for  $Re = 3000$ ,  $r = 0.5$ .

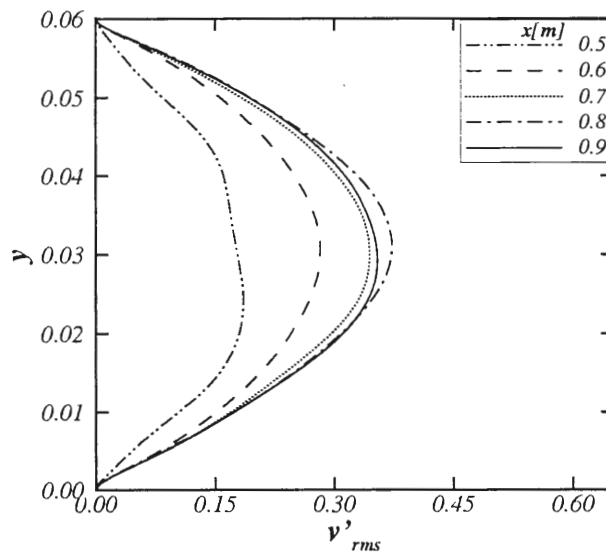


Figure 4.18 Normalized RMS cross-stream velocity at different streamwise locations for  $Re = 3000$ ,  $r = 0.3$ .

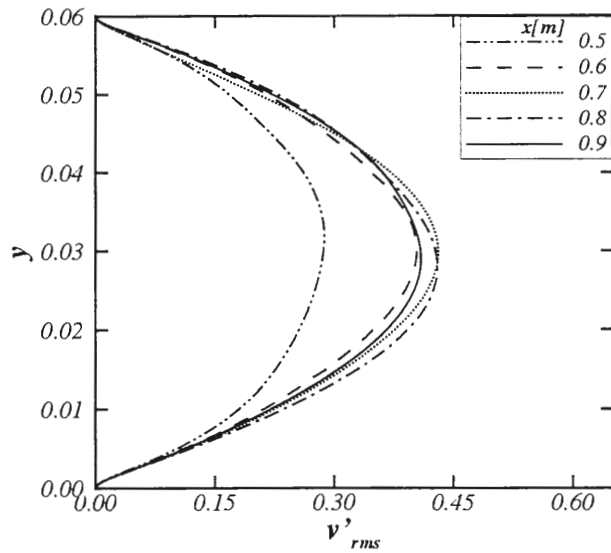


Figure 4.19 Normalized RMS cross-stream velocity at different streamwise locations for  $Re = 3000$ ,  $r = 0.25$ .

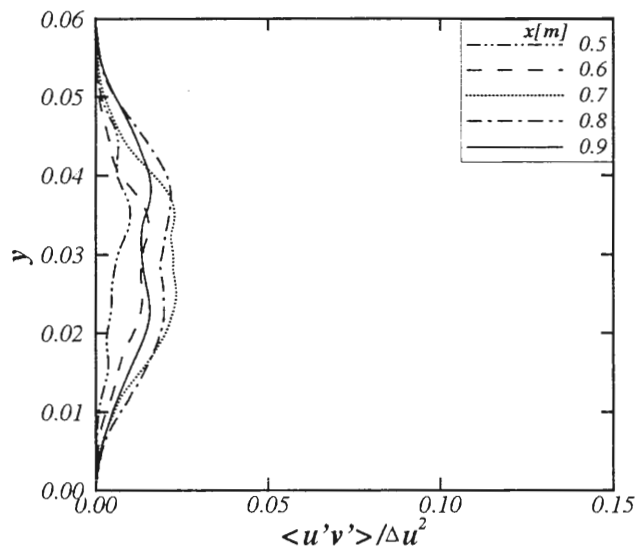


Figure 4.20 Normalized mean Reynolds stress at different streamwise locations for  $Re = 3000$ ,  $r = 0.5$ .

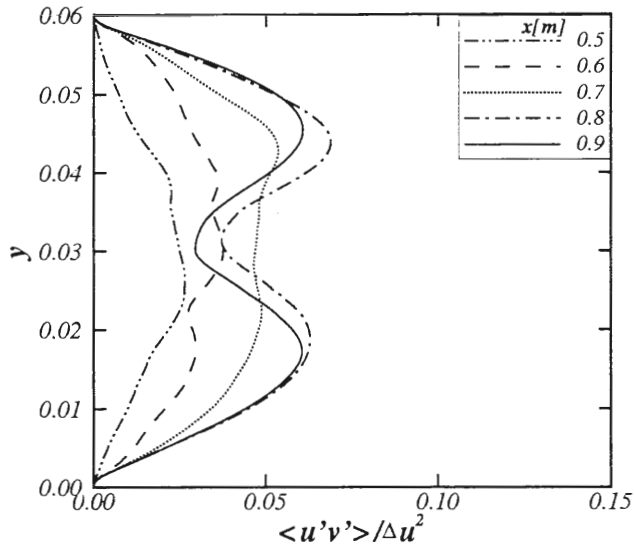


Figure 4.21 Normalized mean Reynolds stress at different streamwise locations for  $Re = 3000$ ,  $r = 0.3$ .

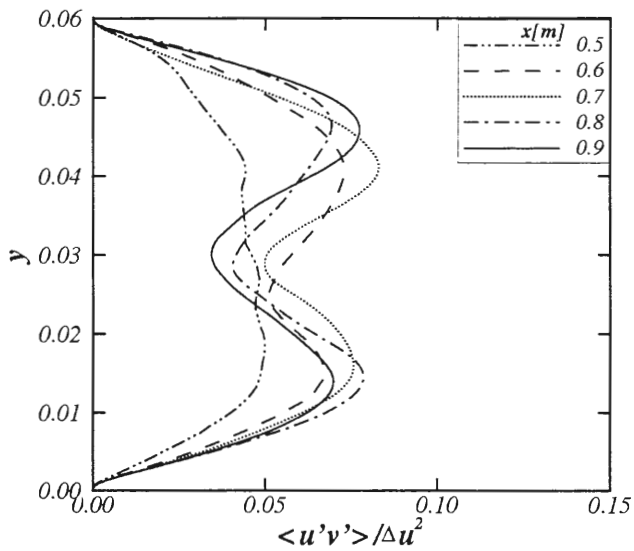


Figure 4.22 Normalized mean Reynolds stress at different streamwise locations for  $Re = 3000$ ,  $r = 0.25$ .

## CHAPTER 5 NUMERICAL SOLUTIONS OF FLOW IN 2-D REACTOR: SCALAR MIXING AND TURBULENCE CLOSURES

In Chapter 4, the hydrodynamic evolution, mixing and entrainment characteristics of the shear layer were discussed. The focus of present chapter is on scalar mixing. A passive scalar is a diffusive contaminant in a fluid flow that is present in such low concentration that it has no dynamical effect on the fluid motion itself [60]. The study of scalar mixing from a large-scale-structure point of view is important since the entrainment of fluid (and hence the growth rate) and the composition field of the layer are controlled by these structures. The presence of coherent vortices heavily affects the dynamics of passively advected scalars. In particular, vortices act as barriers to particle exchanges between the inside and outside of a vortex and enhance coherent transport of particles trapped in the vortex cores [61].

The role of molecular diffusion in mixing is characterized by the Schmidt number,  $Sc = \nu/D$ , defined as the ratio of the kinematic viscosity and scalar diffusivity. The molecular transport kinetics in liquids leads to Schmidt numbers on the order of one-thousand. The smallest physical length scale for mixing is the mass diffusion scale (Batchelor's scale), denoted by  $\lambda_B$ . This mass diffusion scale is related to the viscous scale  $\lambda_\nu$  by,

$$\lambda_B \approx \lambda_\nu Sc^{-0.5}$$

Therefore, as the Schmidt number increases, as in case of liquids, the grid resolution

requirements for the scalar field increases. A Schmidt number of 2 is used in the present simulations to reduce the high resolution requirements.

Direct numerical simulations of passive scalar transport are discussed in this chapter. The advection and diffusion of scalar in a shear-layer is presented. The evolution of scalar in the mixing layer is illustrated by means of probability density functions followed by prediction of closure terms for the Reynolds-averaged Navier-Stokes equations.

## 5.1 Boundary conditions

At the inlet, the scalar concentration is unity in the central stream and zero in the outer streams. At the channel walls and the splitter plate walls, the scalar flux gradient is zero. At the channel exit, the scalar values are extrapolated from within the channel.

## 5.2 Scalar mixing (results for $r = 0.5$ )

The results for a passive scalar field are used to examine the behavior of entrainment and mixing. Presented in Fig. 5.1 are instantaneous contour plots of a passive scalar field. Six frames are shown starting at  $t = 40$  s, where the time interval between two frames is 0.5 s. These results indicate that the fluid is entrained from the fast (red) and slow (blue) feed streams into the shear layer. This representation clearly captures the dynamical evolution of the mixing layer and the mechanisms of entrainment and mixing enhancement [16]. The high-concentration scalar from the fast central stream can be seen diffusing into the outer slow-streams. As the downstream distance from splitter plates increases, the diffusion grows stronger and is a result of mixing.

The time-averaged scalar  $\langle \phi \rangle$  contour is illustrated in Fig. 5.2 and is averaged using 700 realizations in time. A comparison of Figs. 5.1 and 5.2 indicates the limitations of time-averaged data in capturing the detailed unsteady structures. That is, the detailed physical features of the large-scale structures are smeared due to averaging. Also, com-

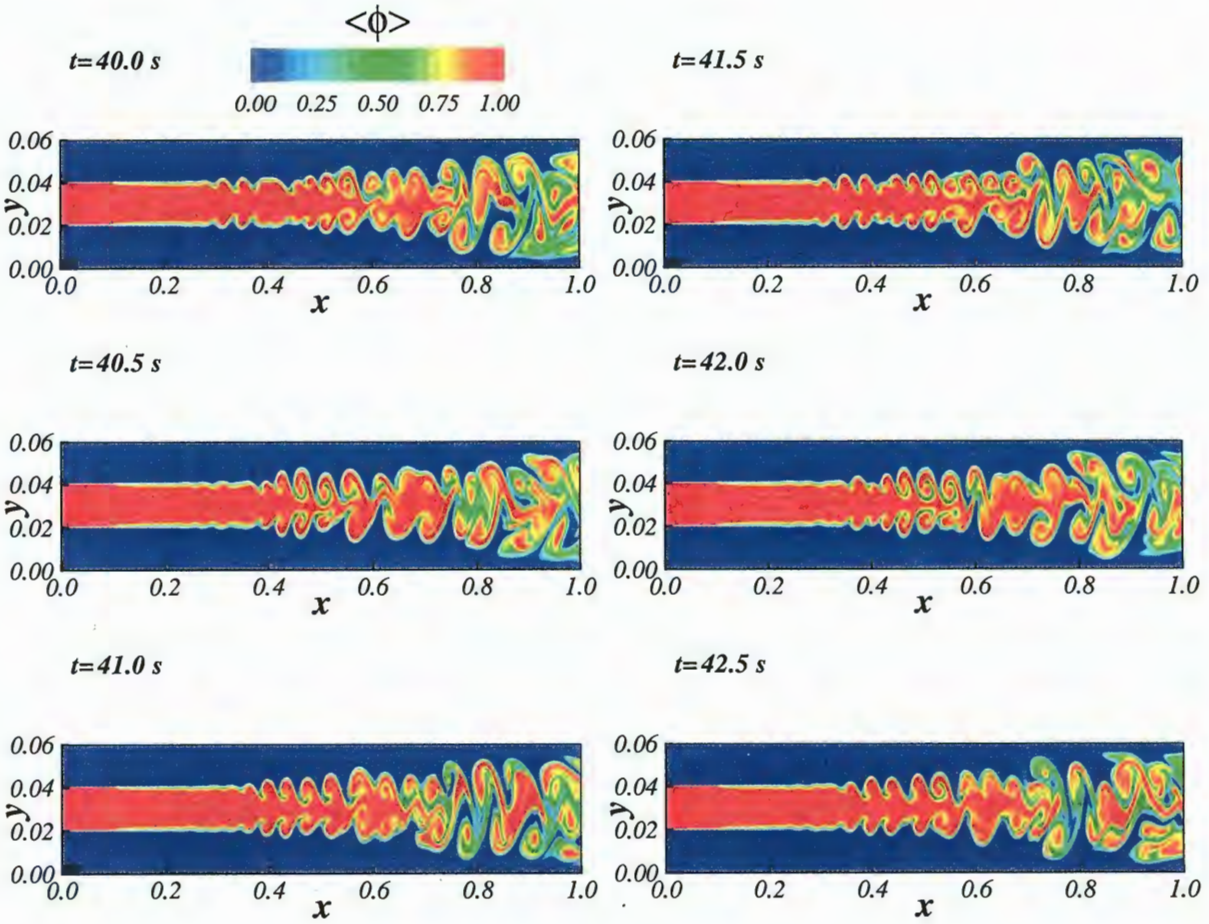


Figure 5.1 Instantaneous contour of scalar diffusing in the shear layer for  $Re = 3000$ ,  $\tau = 0.5$ .

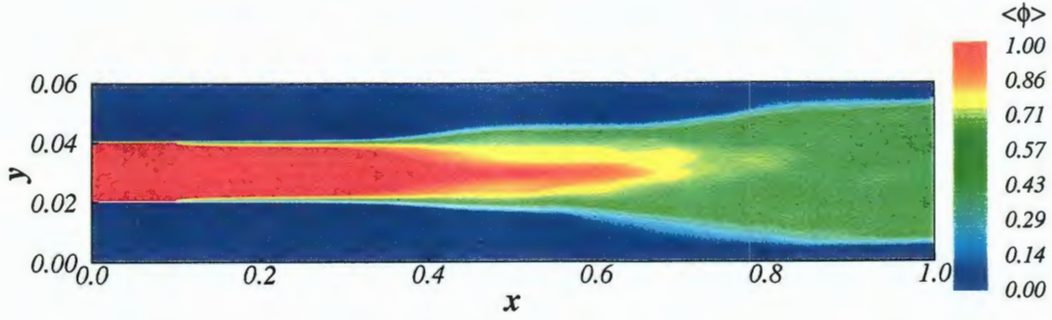


Figure 5.2 Time-averaged scalar contour for  $Re = 3000$ ,  $r = 0.5$ .

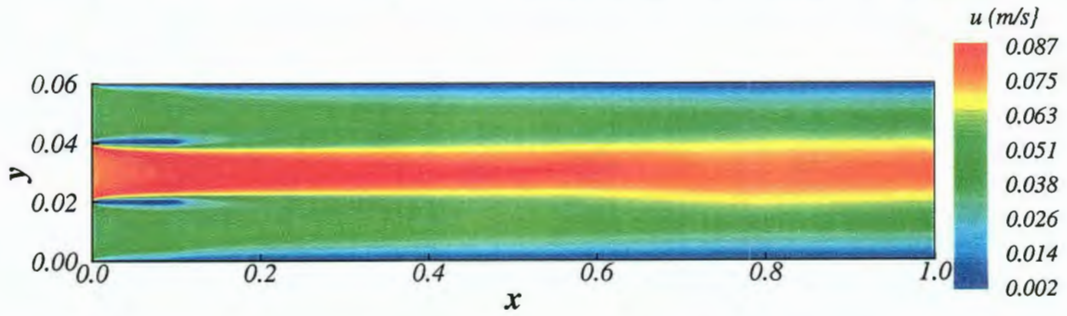


Figure 4.8 Time-averaged velocity contour for  $Re = 3000$ ,  $r = 0.5$ .

parison of mean velocity and mean scalar profile in Figs. 4.8 and 5.2 respectively, reveals that the spreading of the scalar is more than that of the velocity. This indicates that the scalar mixing region extends further into the feed streams than does the momentum mixing region, suggesting enhanced transport of scalars over momentum. A reason for this could be the low value of Schmidt number used for present simulations. The Schmidt number used is on the order used for gases which have high diffusion.

Figures 5.3 and 5.4 show the time-averaged contour plots of scalar variance and intensity of segregation respectively, where

$$\begin{aligned} \text{variance} &= \langle (\langle \phi \rangle - \phi)^2 \rangle \\ \text{intensity of segregation} &= \frac{\text{variance}}{\langle \phi \rangle (1 - \langle \phi \rangle)} \end{aligned}$$

Variance is a measure of the spread, or dispersion of the scalar around its mean [62]. Since the scalars are conserved, their values must strictly lie between 0 and 1. Maximum variance occurs when the mean is 0.5 and the maximum variance has a value of 0.25. For

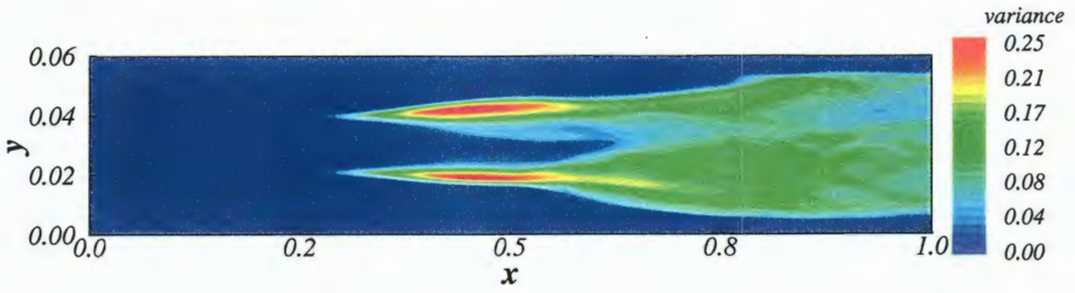


Figure 5.3 Time-averaged scalar variance plot showing the extent of mixing for  $Re = 3000$ ,  $r = 0.5$ .

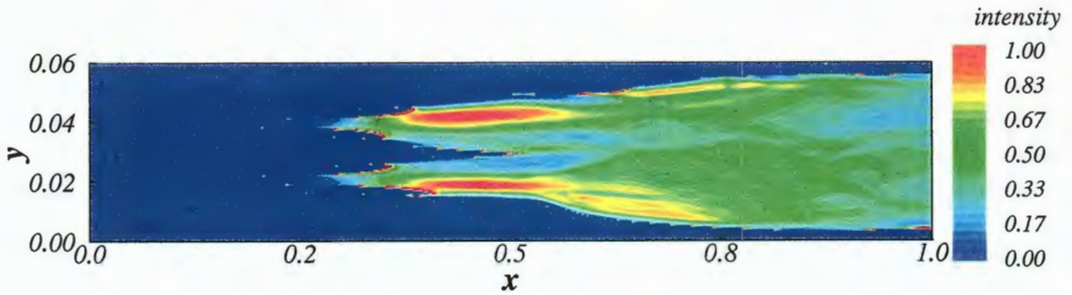


Figure 5.4 Time-averaged intensity of segregation characterizing the concentration uniformity for  $Re = 3000$ ,  $r = 0.5$ .

the present simulations, the maximum variance is obtained near the center of each of the two shear layers, i.e., in the plane of the splitter plates (see Fig. 5.3). The intensity of segregation characterizes the concentration uniformity and is computed by dividing the variance at a point by the maximum variance that can occur at that point. It follows then, that the intensity of segregation can have a maximum value of 1, which, in the present case occurs in the plane of the splitter plates, as shown in Fig. 5.4.

### 5.3 Results for different velocity ratios.

Time-averaged scalar profiles at different streamwise locations are shown in Figs. 5.5–5.7 for velocity ratios of 0.5, 0.3 and 0.25 respectively. From Fig. 5.5, it is observed that as the streamwise distance from the splitter plate increases, the scalar diffusion from

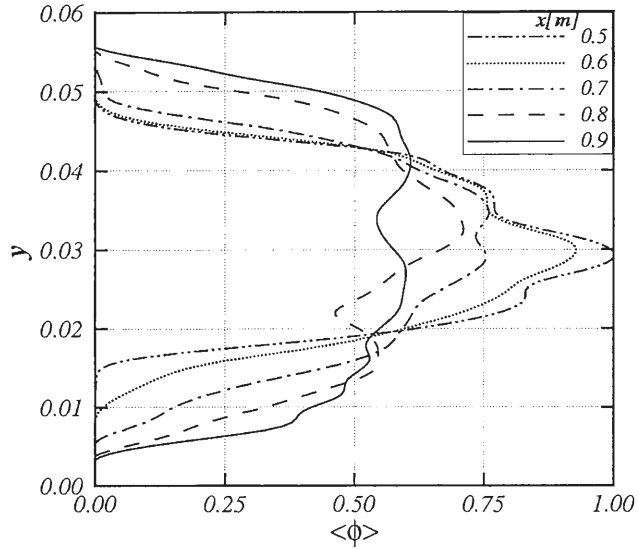


Figure 5.5 Normalized mean conserved scalar profiles for  $Re = 3000$ ,  $r = 0.5$ .

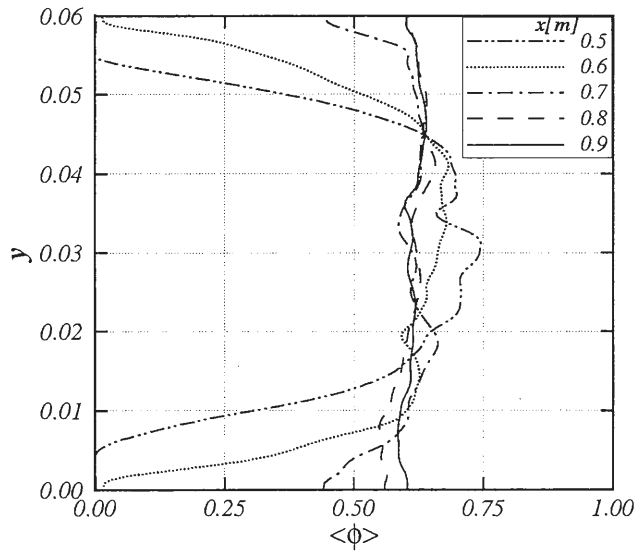


Figure 5.6 Normalized mean conserved scalar profiles for  $Re = 3000$ ,  $r = 0.3$ .

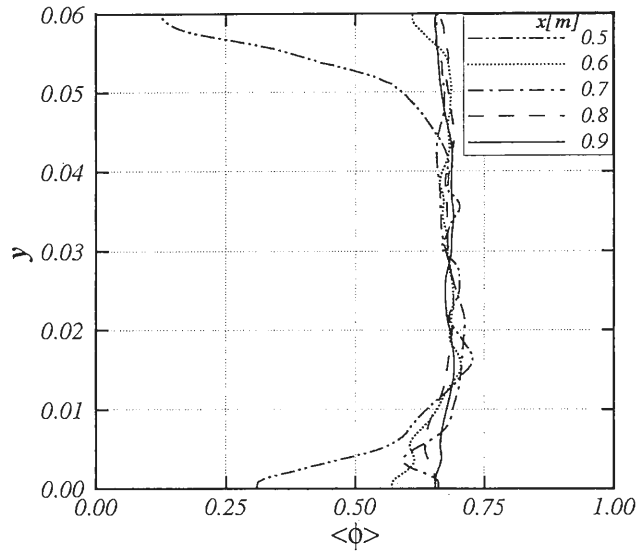


Figure 5.7 Normalized mean conserved scalar profiles for  $Re = 3000$ ,  $r = 0.25$ , .

the inner stream into the outer streams intensifies. This is shown by the decrease in the peak value of the mean scalar as the downstream distance increases and a corresponding increase of scalars near the channel walls. A similar trend is observed in Figs. 5.6 and 5.7 for velocity ratios of 0.3 and 0.25 respectively. Moreover, for the velocity ratio of 0.3, the scalar profile is an almost straight line beyond  $x = 0.8$  m and for the velocity ratio of 0.25, it is constant beyond 0.6 m. This however is not observed for the case of  $r = 0.5$  and can be explained as follows. For a velocity ratio of 0.5, the velocity difference between the fast and slow streams is small and the fast stream is unable to completely penetrate into the boundary layer of the slow stream. As the velocity ratio decreases (and the velocity difference between fast and slow streams increases) the fast stream is able to penetrate better into the slow stream causing efficient mixing. Hence for  $r = 0.5$ , the mixing is less efficient and can be seen by the zero-concentration scalars close to channel walls (refer to Fig. 5.5).

The RMS values of the scalar variable are illustrated in Figs. 5.8–5.10 for velocity

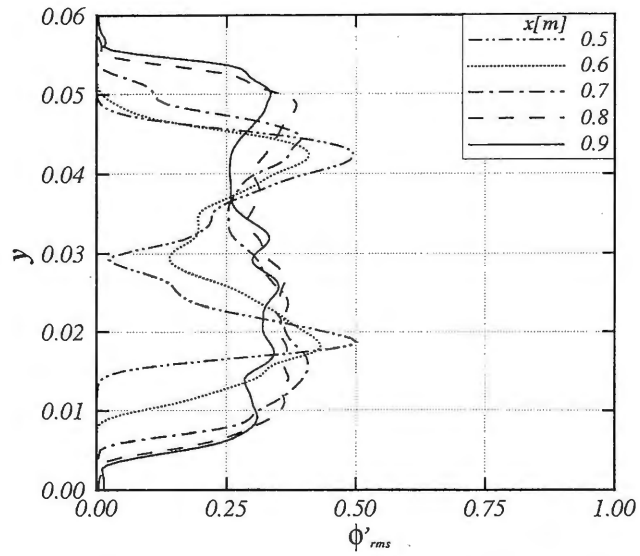


Figure 5.8 Normalized RMS conserved scalar profiles for  $Re = 3000$ ,  $r = 0.5$ .

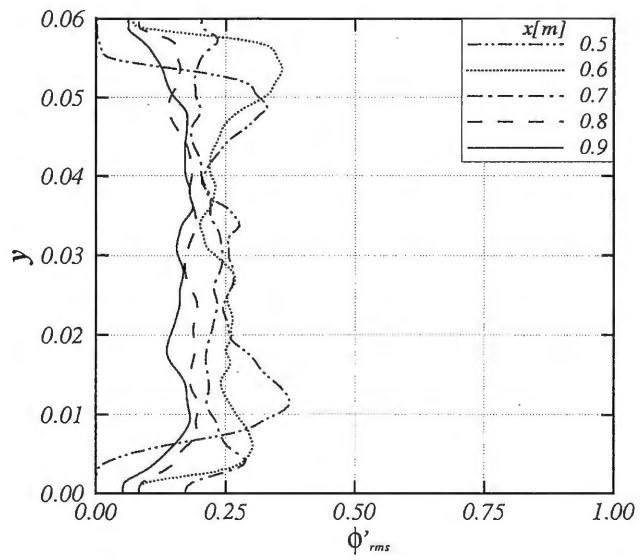


Figure 5.9 Normalized RMS conserved scalar profiles for  $Re = 3000$ ,  $r = 0.3$ .

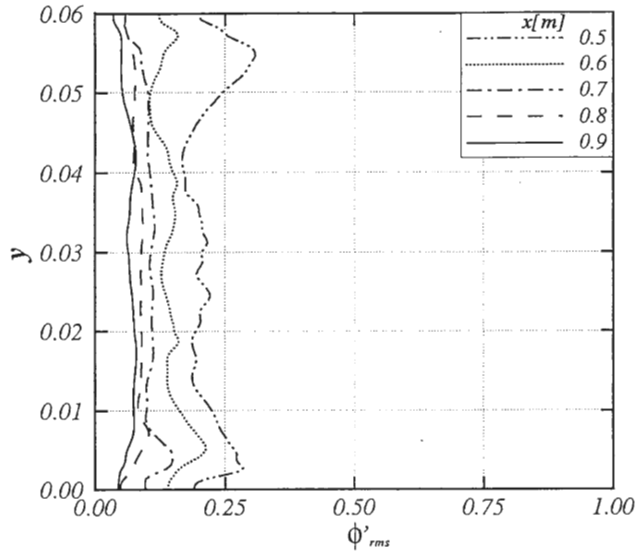


Figure 5.10 Normalized RMS conserved scalar profiles for  $Re = 3000$ ,  $r = 0.25$ .

ratios of 0.5, 0.3 and 0.25 respectively. The RMS values of the normalized concentrations across the layer, obtained from direct numerical simulations indicate that there are two peaks in the RMS profiles. These peaks are obvious for  $r = 0.5$  (refer Fig. 5.8), but less obvious for cases  $r = 0.3$  and  $r = 0.25$  (refer to Figs. 5.9 and 5.10) respectively. The peaks correspond to the location where the gradient of the mean value is highest. With increasing streamwise distance, the gradients reduce and so do the peak RMS values. In the case of  $r = 0.5$ , the scalar RMS close to walls is negligible indicating that for this case, the scalars never reach the channel walls, a result of inefficient mixing. For the case of  $r = 0.25$ , the RMS profile does not vary much across the cross-stream direction. Also the magnitude of RMS velocity reduces for this case beyond 0.7 m. The flat profile resembles the mean scalar profile at the same cross-sections. This re-emphasizes the fact that mixing is enhanced when the inner feed stream is much faster than the outer streams.

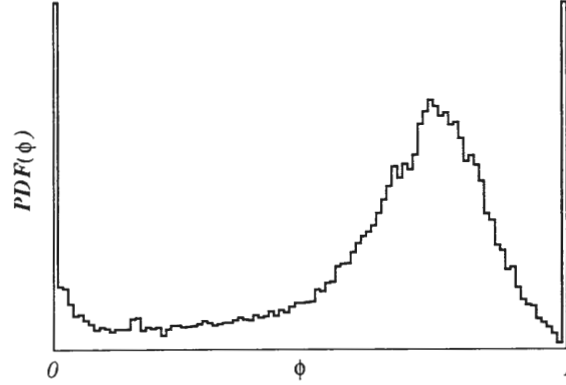


Figure 5.11 A typical PDF

## 5.4 Probability density function (PDF)

The time records of scalar  $\phi$  are used to construct probability density functions of the mixture fraction. The PDF is defined in the conventional manner:

$f(\alpha) d\alpha = \text{probability that } \alpha < \phi < \alpha + d\alpha, \text{ and}$

$$\int_{-\infty}^{\infty} f(\phi) d\phi = 1$$

A typical PDF of  $\phi$  across a given cross-section is shown in Fig. 5.11. The two ‘delta’ functions at  $\phi = 0$  and  $1$  are associated with the pure unmixed fluids in the low- and high-streams, respectively. The third peak in the plot between zero and one is the PDF of the ‘preferred’ scalar concentration  $\phi_p(x)$  for the mixed fluid. The value of  $\phi_p(x)$  at a given streamwise location in the flow does not change across the mixing layer, although the height of the peak may vary [17].

Here, the PDFs are shown for the three velocity ratios of 0.5, 0.3 and 0.25 in Figs. 5.12– 5.14 respectively. The range of  $\phi$ , (0–1), is divided into one-hundred intervals. PDFs are shown at four streamwise locations representing the evolution of the

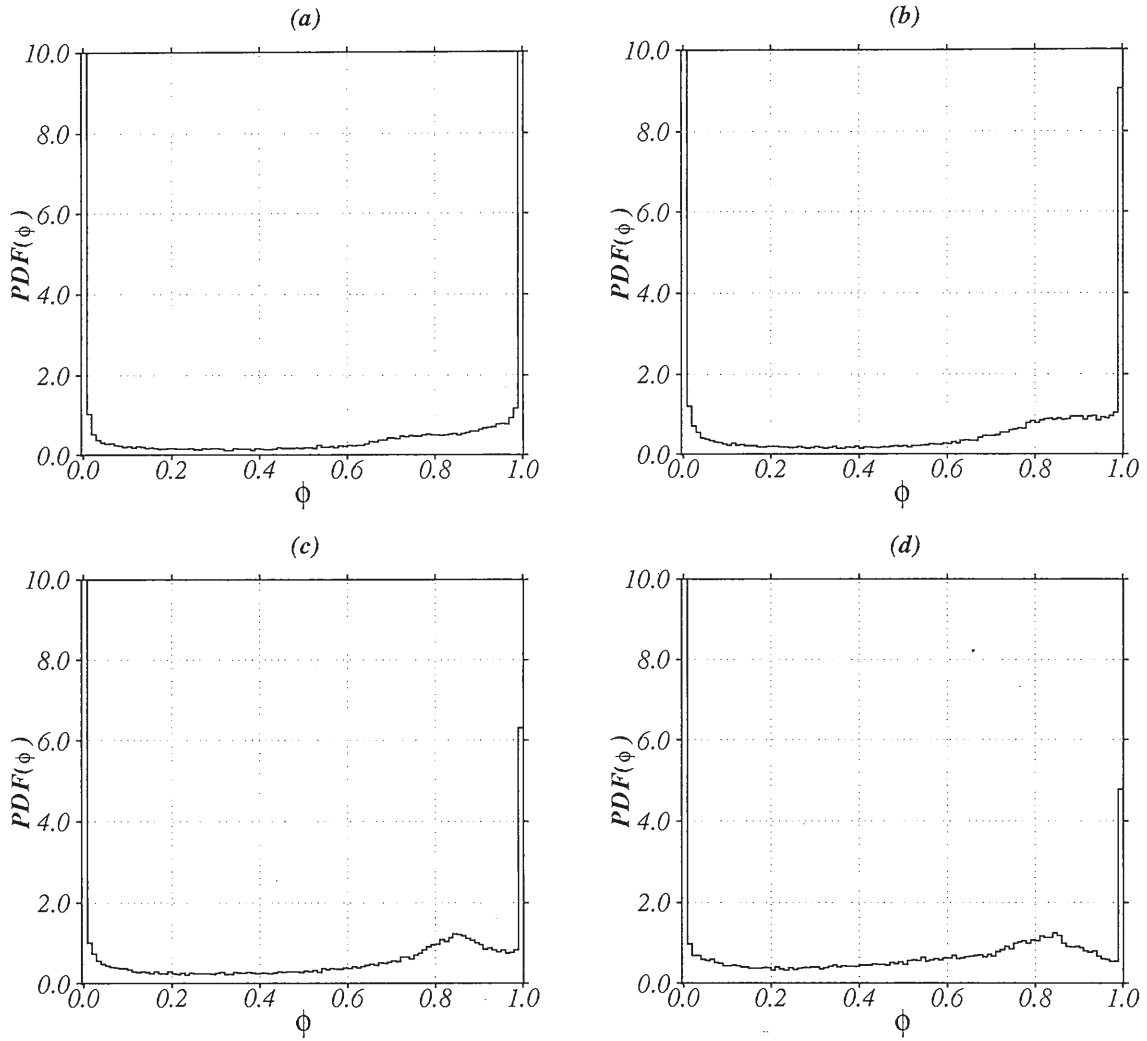


Figure 5.12 Evolution of the PDF of the scalar field for  $Re = 3000$ ,  $r = 0.5$ ,  
 (a)  $x = 0.5$  m, (b)  $x = 0.6$  m, (c)  $x = 0.7$  m, (d)  $x = 0.8$  m.

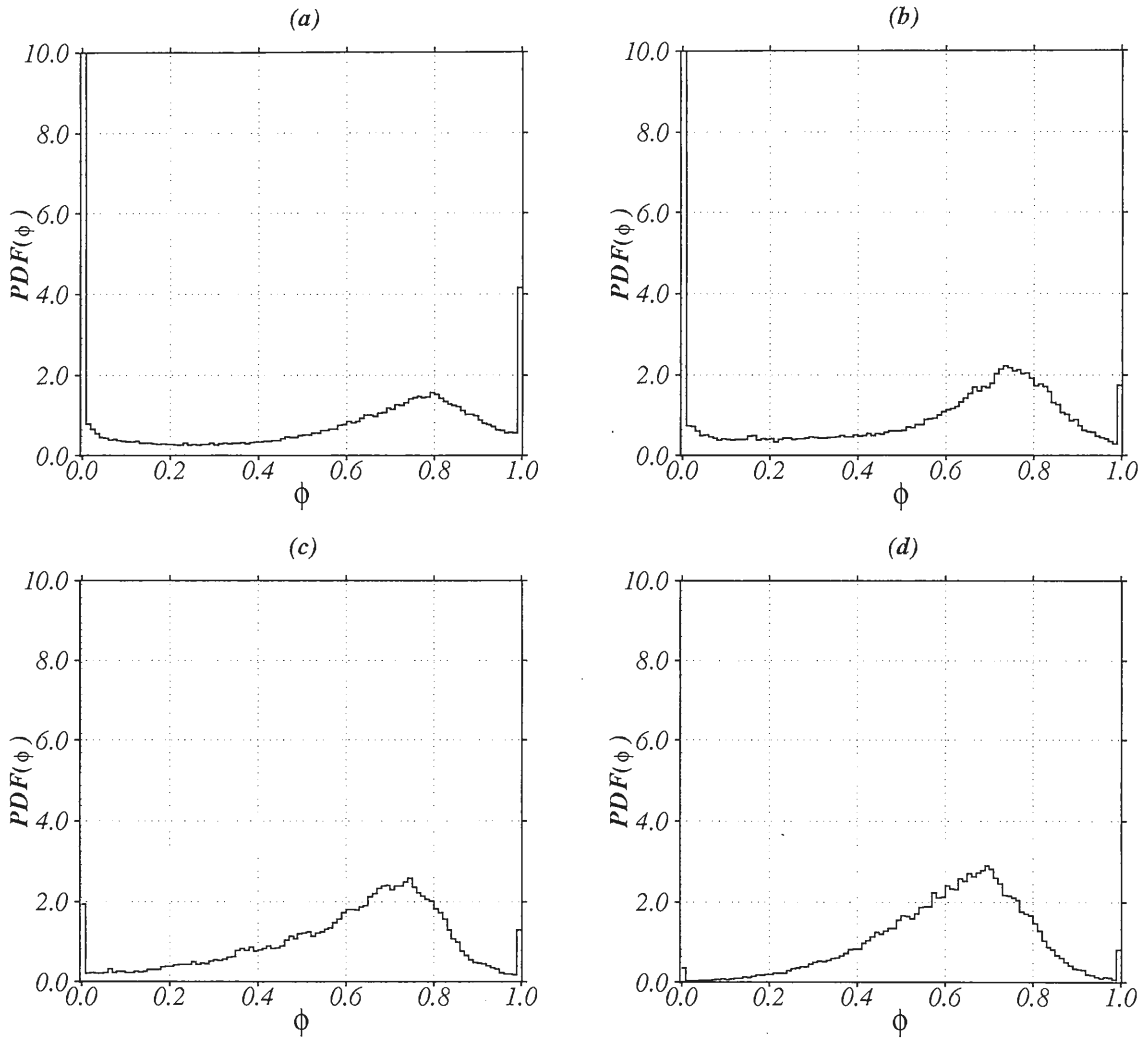


Figure 5.13 Evolution of the PDF of the scalar field for  $Re = 3000$ ,  $r = 0.3$ , (a)  $x = 0.5$  m, (b)  $x = 0.6$  m, (c)  $x = 0.7$  m, (d)  $x = 0.8$  m.

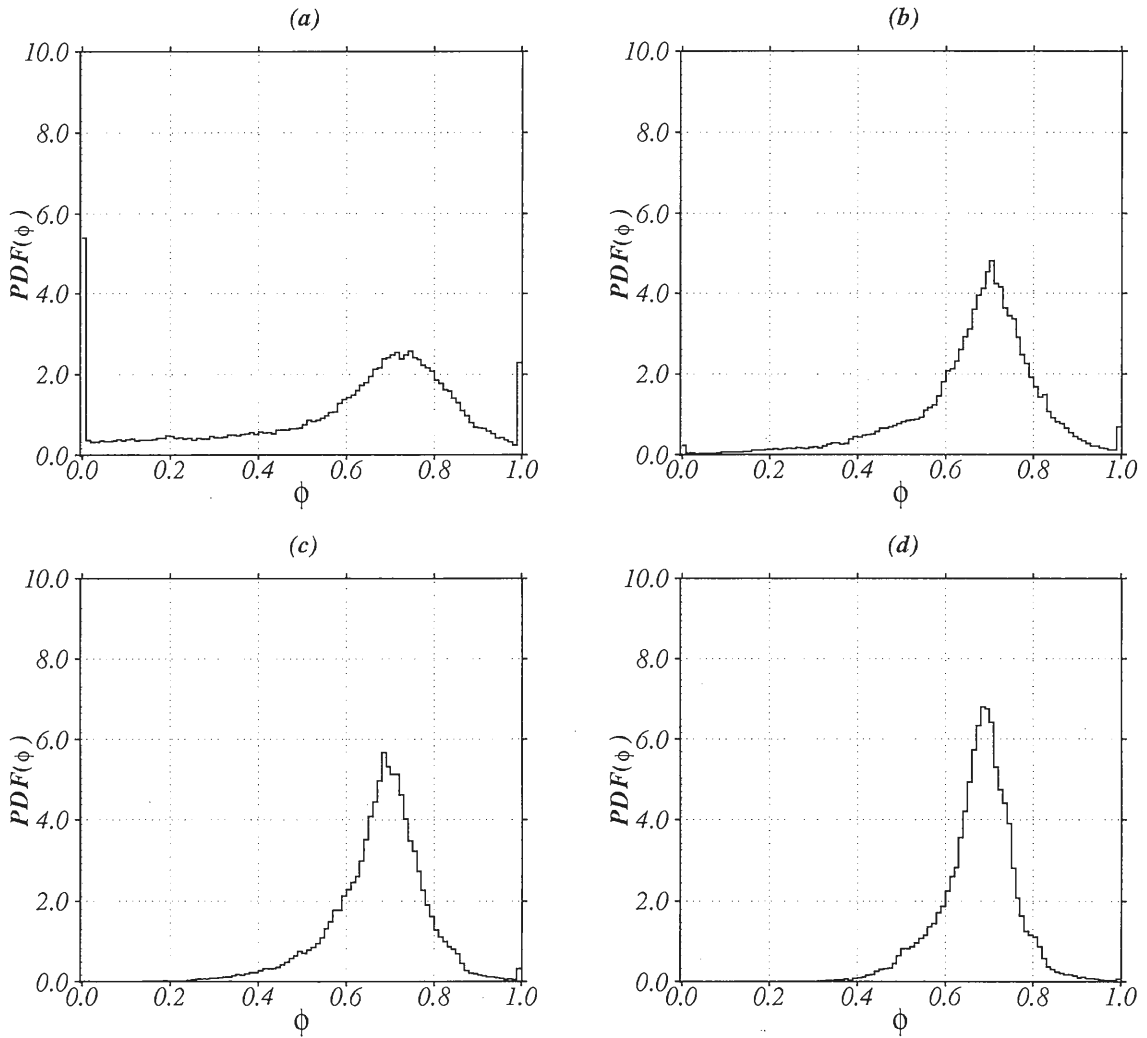


Figure 5.14 Evolution of the PDF of the scalar field for  $Re = 3000$ ,  $r = 0.25$ , (a)  $x = 0.5$  m, (b)  $x = 0.6$  m, (c)  $x = 0.7$  m, (d)  $x = 0.8$  m.

PDF during the mixing transition for the three velocity ratios. Each plot shows four frames of PDFs along the cross-stream direction at four different streamwise locations. Initially the PDFs are dominated by the delta peaks at  $\phi = 0$  and 1. As the downstream distance increases, the mixing layer evolves as can be seen by the development of the preferred concentration peak. The third peak is clearly noticeable for the cases  $r = 0.3$  and  $r = 0.25$  (Figs. 5.13 and 5.14) where mixing is more efficient than for  $r = 0.5$ . For  $r = 0.5$ , the conserved-scalar PDFs are characterized by peaks at 0 and 1, with probability densities only slightly greater than zero for  $0 < \phi < 1$ . The preferred concentration for velocity ratio of 0.3 changes from 0.8 to 0.7 and that for 0.25 changes from 0.75 to 0.66 along the downstream distance. It has been shown that the extent of mixing in liquid shear layers during the mixing layer growth changes from a lower value to a higher value [34]. The same trends are observed in this research, as shown most clearly in Figs. 5.13 and 5.14 by the increase in the PDF peaks.

## 5.5 Assessment of turbulence closures: turbulent viscosity and gradient diffusion hypotheses

An alternative approach to direct numerical simulations is the solution of turbulent flow problems by means of the Reynolds-Averaged Navier-Stokes equations (RANS). In RANS, the *averaged* properties of the transport variables are considered. The equations governing the transport of these averaged quantities contain various statistical correlations involving the fluctuations of the transport variables. These fluctuations are unknown and must be modeled for a complete closure. In turbulence simulations, particularly those of practical flows, traditionally *ad hoc* models are utilized for such closures. Unfortunately, the results obtained in this manner do not always capture the essential dynamical behavior of the flow. The use of model-free simulations can help overcome this problem in cases where such direct numerical simulations are possible. The results

furnished by model-free simulations can be utilized either to construct a new model, or to assess the extent of validity of a proposed closure.

### 5.5.1 Turbulent viscosity

The turbulent-viscosity hypothesis was introduced by Boussinesq [63] and is mathematically analogous to the stress-rate-of-strain relation for a Newtonian fluid. According to the hypothesis, the Reynolds stress is proportional to the mean rate of strain [1],

$$-\rho\langle u'v' \rangle = \rho\nu_T \left( \frac{\partial\langle u \rangle}{\partial y} + \frac{\partial\langle v \rangle}{\partial x} \right)$$

where the positive scalar coefficient  $\nu_T$  is the *turbulent viscosity* (also called eddy viscosity).  $\langle u \rangle$  and  $\langle v \rangle$  are the mean velocities in the streamwise and cross-stream directions, respectively and  $u'$  and  $v'$  are their respective fluctuations. The term  $\langle u'v' \rangle$  forms the Reynolds stress.

### 5.5.2 Turbulent diffusivity

The scalar flux  $\langle \mathbf{u}\phi' \rangle$  vector gives both the direction and the magnitude of the turbulent transport of the conserved scalar  $\phi$ . According to the gradient-diffusion hypothesis, transport is along the mean scalar gradient, i.e., in the direction of  $-\nabla\langle\phi\rangle$ . Thus, according to the hypothesis, there is a positive scalar,  $\Gamma_T(x, t)$ , known as the *turbulent diffusivity*, such that

$$\langle \mathbf{u}\phi' \rangle = -\Gamma_T \nabla\langle\phi\rangle$$

## 5.6 Modeling of turbulent convective fluxes

An important class of flows consists of those that can be described by the two-dimensional turbulent boundary layer equations. In these flows, the mean velocity  $\langle u \rangle$  is predominantly in the  $x$ -direction, while variations in mean quantities are predominantly

in the  $y$ -direction. Only one component  $\langle v' \phi' \rangle$  of the scalar flux, and one Reynolds stress term  $\langle u' v' \rangle$ , appear in the boundary layer equations. Consequently, the gradient-diffusion hypothesis reduces to

$$\langle v' \phi' \rangle = -\Gamma_T \frac{\partial \langle \phi \rangle}{\partial y} \quad (5.1)$$

and the turbulent-viscosity hypothesis becomes

$$\langle u' v' \rangle = -\nu_T \frac{\partial \langle u \rangle}{\partial y} \quad (5.2)$$

Equations 5.1 and 5.2 relate a single covariance to a single gradient and these equations can be taken as definitions of  $\Gamma_T$  and  $\nu_T$ , respectively. Specification of  $\nu_T(x, t)$  and  $\Gamma_T(x, t)$  solves the closure problem. That is, if  $\nu_T$  and  $\Gamma_T$  can somehow be specified, then the mean flow equations for  $\langle \mathbf{u} \rangle$  and for  $\langle \phi \rangle$  can be solved.

The values of turbulent viscosity are evaluated from the DNS data previously discussed in Chapter 4 to check and see if  $\nu_T$  is independent of position. Figures. 5.15–5.17 show the normalized turbulent viscosity  $\nu_T/\nu$  calculated at streamwise locations of 0.5 and 0.6 m for velocity ratios of 0.5, 0.3 and 0.25, respectively. The values of turbulent viscosity are reasonable and on the order of the molecular viscosity ( $10^{-6}$  m<sup>2</sup>/s for water). The existence of a narrow range for the values of  $\nu_T$  is encouraging from a modeling point of view and the RANS procedure can provide a reasonable means of depicting the mean transport in a boundary layer approximation of the Navier–Stokes equations in parallel shear flows. The peaks in the plots for  $r = 0.3$  and  $r = 0.5$  is due to the presence of low mean scalar gradients at these locations.

The turbulent Schmidt number  $Sc_T$  is the ratio of turbulent viscosity and turbulent diffusivity

$$Sc_T = \frac{\nu_T}{\Gamma_T}$$

Schmidt number profiles are shown in Figs. 5.18–5.20 for velocity ratios of 0.5, 0.3 and 0.25, respectively. Most of the values of  $Sc_T$  lie in the range of  $0 < Sc_T < 2.5$  as seen

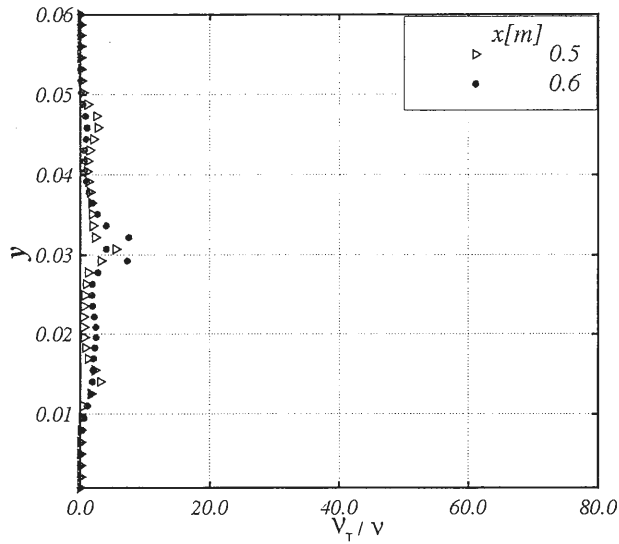


Figure 5.15 Normalized turbulent viscosity at  $x = 0.5, 0.6$  m for  $Re = 3000$ ,  $r = 0.5$ , showing every 3rd point.

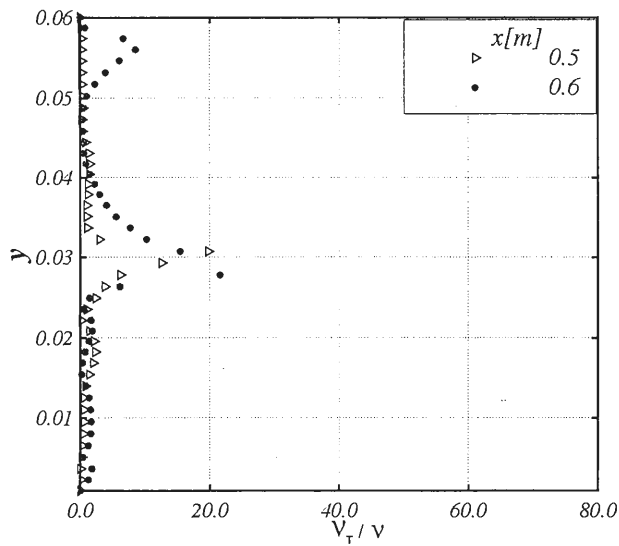


Figure 5.16 Normalized turbulent viscosity at  $x = 0.5, 0.6$  m for  $Re = 3000$ ,  $r = 0.3$ , showing every 3rd point.

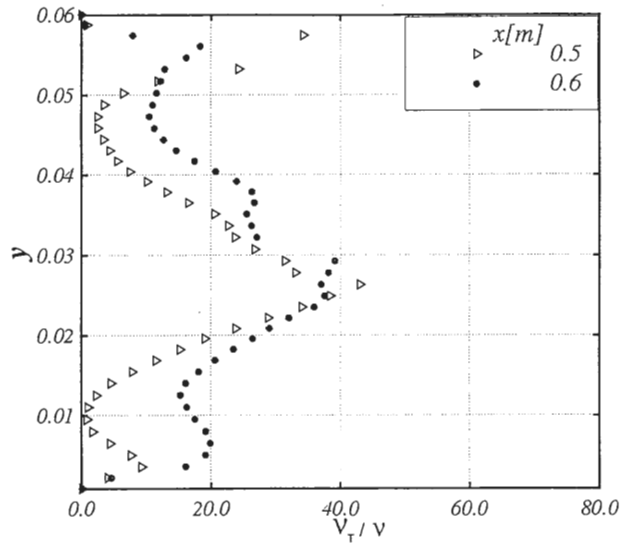


Figure 5.17 Normalized turbulent viscosity at  $x = 0.5, 0.6$  m for  $Re = 3000$ ,  $r = 0.25$ , showing every 3rd point.

from Figs. 5.18–5.20. A few points however lie outside this range and some have values close to 20 (refer to Fig. 5.19) and 45 (refer to Fig. 5.20). In highly intermittent flows such as mixing layers, the turbulent flow is interrupted by the presence of the non-turbulent surrounding flow and a simple gradient diffusion model does not accurately account for this discontinuity [64].

In this chapter, the advection and diffusion of a passive scalar field in the reactor was presented. The evolution of scalar-PDFs were also evaluated along the channel and the chapter was closed with a discussion of closure models for RANS equations. The following chapter will introduce three-dimensional simulations which forms the basis for future work.

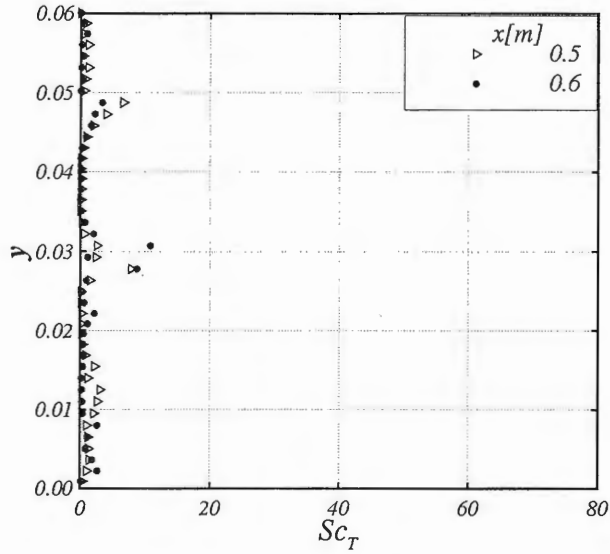


Figure 5.18 Turbulent Schmidt number at  $x = 0.5, 0.6$  m for  $Re = 3000$ ,  $r = 0.5$ , showing every 3rd point.

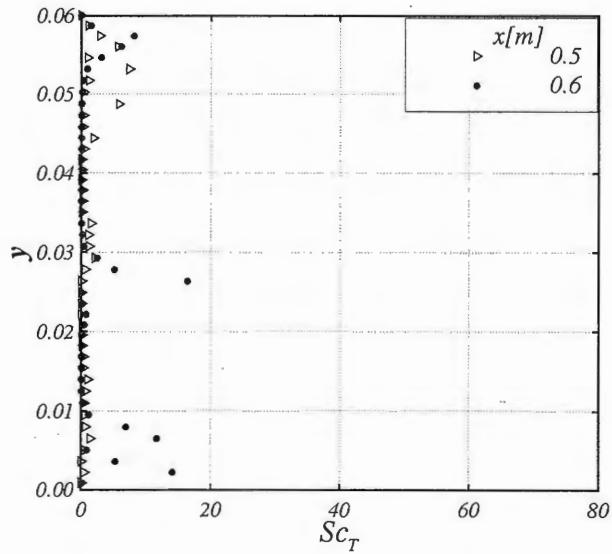


Figure 5.19 Turbulent Schmidt number at  $x = 0.5, 0.6$  m for  $Re = 3000$ ,  $r = 0.3$ , showing every 3rd point,  $Re = 3000$ .

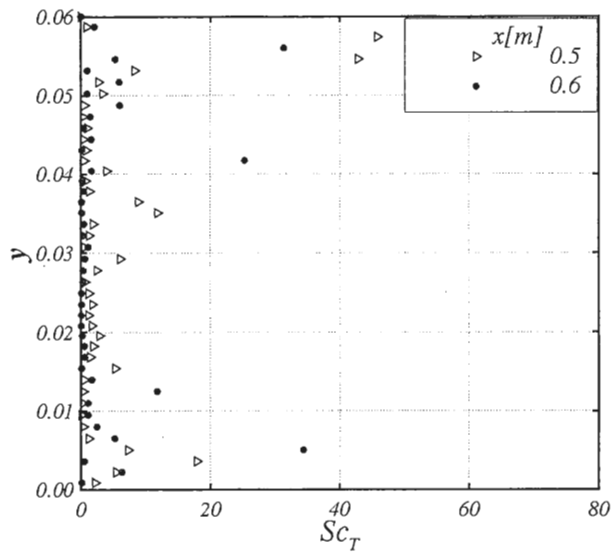


Figure 5.20 Turbulent Schmidt number at  $x = 0.5, 0.6$  m for  $Re = 3000$ ,  $r = 0.25$ , showing every 3rd point,  $Re = 3000$ .

## CHAPTER 6 TOWARD THREE-DIMENSIONAL SOLUTIONS: PROGRESS AND FUTURE WORK

The two-dimensional simulations have provided insights into the evolution of the mixing layer in the channel. Turbulent scales however are not limited to two-dimensions. It is therefore important to look at the mixing problem from a three-dimensional point of view. It has been observed that the shear layer contains a well organized array of streamwise vortices that superimpose onto spanwise eddies [40,41]. Results have shown that the streamwise structures first form in the braided region connecting adjacent spanwise vortices that lack significant spanwise vorticity and are dominated by large-scale strain [40–43]. The resolution requirements increase for direct numerical simulations (DNS) of three-dimensional problems. The Kolmogorov length scale is commonly quoted as the smallest scale that should be resolved and is given by  $(\nu/\epsilon)^{1/4}$ , where,  $\nu$  is the kinematic viscosity and is on the order of viscous scales and  $\epsilon$  is the dissipation and is on the order of large eddies. This requirement is too rigid and the resolution should be fine enough to capture most of the dissipation in order to obtain required statistical information [2].

The objective of this chapter is to provide an account of the progress toward simulating a three-dimensional mixing layer in the reactor and recommend directions for future work. A low Reynolds number is used for the purpose of simulation ( $Re = 1500$ ) in order to reduce the high resolution requirements. Since the three-dimensional simulations are presented from a point of view of future work, a qualitative analysis of the results is put

forth.

## 6.1 Numerical considerations

The results of three-dimensional direct numerical simulations will be validated against experimental data. These experiments will be performed in the near future using Particle Image Velocimetry and Planar Laser Induced Fluorescence. Direct numerical simulations will play an important role in extracting flow statistics that cannot be easily measured by experiments. The biggest hindrance for three-dimensional simulations using the present version of the code is that the computational time and memory requirements increase tremendously as the dimension of the problem changes from two to three. Moreover, as the Reynolds number increases, the grid size required increases exponentially as  $Re^{9/4}$ . Hence in this chapter results for a coarse grid simulation are presented as a first step towards future three-dimensional simulations. The present simulations were executed on a SUN-6800 machine using 4 processors. Automatic parallelization was used to run the code. The CPU time was around 15 minutes per time step per processor.

## 6.2 Configuration

### 6.2.1 Geometry and mesh

A schematic of the three-dimensional geometry is shown in Fig. 6.1. The three streams enter on the left side of the channel of length 1.0 m ( $L_c$ ), separated by splitter plates of length  $L_s$  for a streamwise distance of 0.1 m. The height of the channel in cross-stream direction is 0.06 m and is denoted by  $h$ . The length of domain in the spanwise direction is 0.1 m and denoted by  $w$ . The domain size is chosen to match with the experimental apparatus. The channel is enclosed by walls in the cross-stream and spanwise directions. Figure 6.2 is the grid used for the simulation and has  $513 \times 65 \times 73$

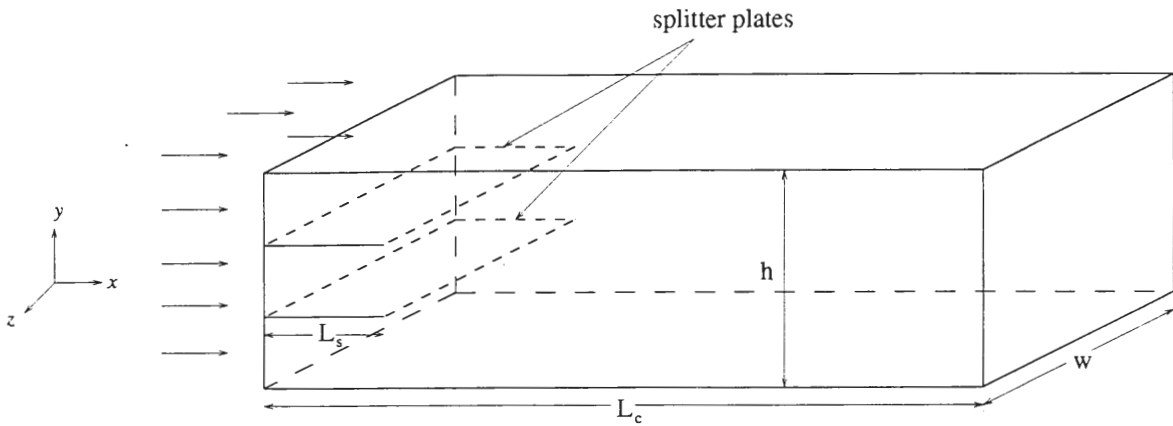


Figure 6.1 Schematic of mixing of three co-flowing streams in a reactor.

points in the  $x$ -,  $y$ - and  $z$ -directions, respectively. The grid is clustered near the channel walls and splitter plate walls to resolve the gradients in the flow.

### 6.2.2 Initial and boundary conditions

At the walls, a no-slip boundary condition is imposed. A plug flow velocity is specified at the inlet and ambient pressure is specified at the outlet. All other variables are extrapolated from within the domain. The high speed stream has velocity of  $u_2 = 0.045$  m/s and slow speed streams have speed of  $u_1 = 0.015$  m/s, making the velocity ratio  $r = 0.3$ . The Reynolds number based on average velocity in channel and the channel height is 1500. Initially a two-dimensional simulation was performed and the results of the two-dimensional simulation were used to initialize the three-dimensional solutions. This proves to be an excellent initial condition to implement for a three-dimensional simulation.

## 6.3 Results

Transient simulations were performed for the three-dimensional evolution of mixing layers. Since a coarse-grid is used for the simulations, the initial vortex is delayed and rollup occurs further downstream of the splitter plate. All results discussed are at an

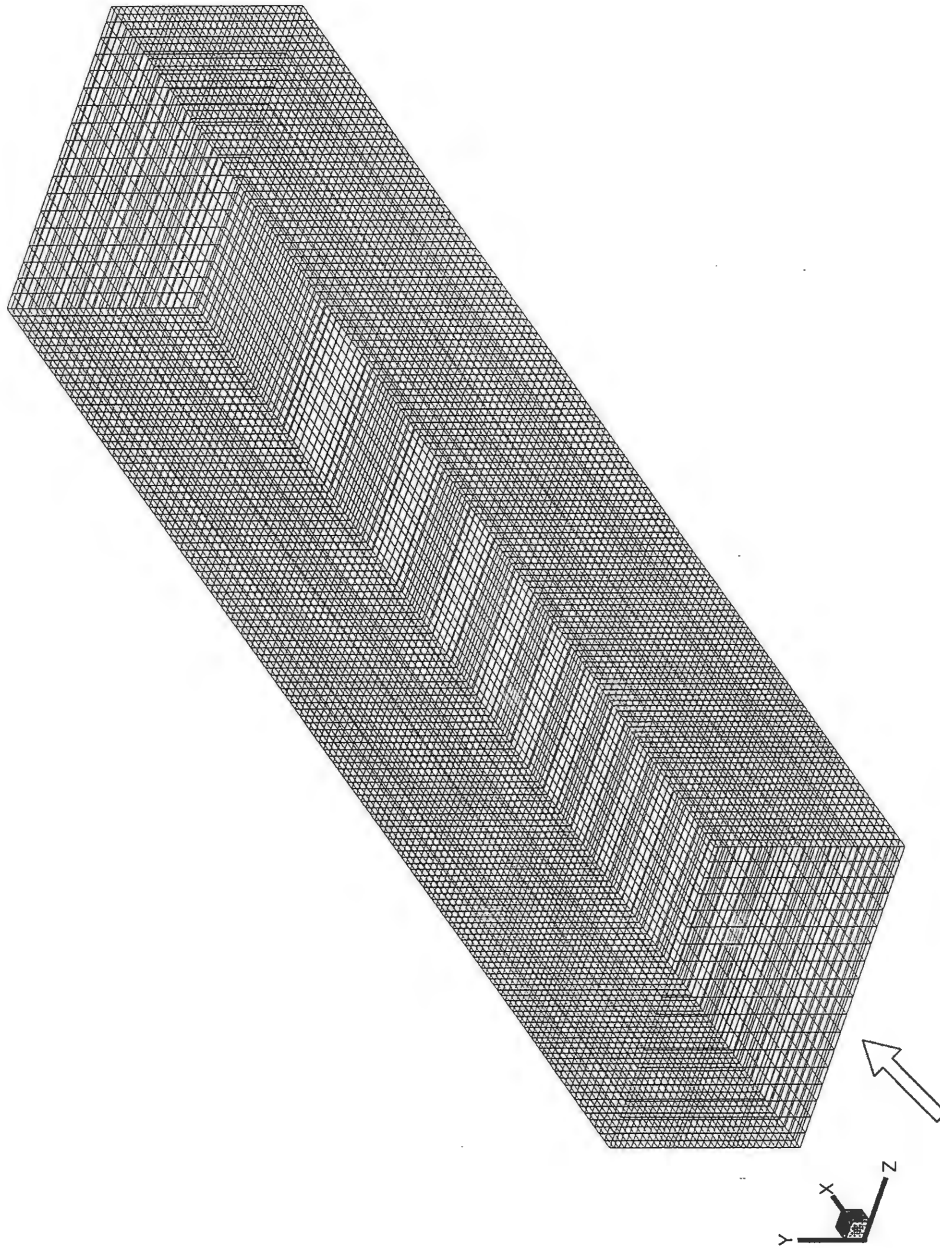


Figure 6.2 Grid for a three-dimensional reactor. Mesh is  $513 \times 65 \times 73$  showing every 4th node in  $x$ ,  $y$  and  $z$  directions.

instantaneous time of  $t = 75$  s. Figure 6.3 shows spanwise vorticity at three spanwise locations of  $z = 0.004$  m,  $0.02$  m and  $0.035$  m. The plane at  $z = 0.004$  m is close to the channel wall (at  $z = 0$  m) and hence the vorticity is small at this section as seen from the figure. The magnitude of vorticity increases as the distance from the channel wall increases. At  $z = 0.02$  m and  $z = 0.035$  m, the vortical structures can be seen growing as the flow moves downstream. The first vorticity rollup occurs at  $x = 0.5$  m and the structures grow larger with increasing downstream distance (for details on growth of mixing layer refer to Chapter 4). Figure 6.4 shows the passive scalar contours at the same three spanwise locations. The scalars mix in the channel by advection and diffusion. The faster fluid (red) is entrained into the shear layer along with the slower fluid (blue) which is engulfed into the mixing layer from the outer streams.

Fig. 6.5 shows cross-stream vorticity at three cross-stream planes, at distances  $y = 0.0095$  m,  $0.02$  m and  $0.03$  m. Plane  $y = 0.0095$  m is located between the lower channel wall (at  $y = 0$  m) and the lower splitter plate (at  $y = 0.02$  m). The section at  $y = 0.02$  is in the plane of the lower splitter plate and section at  $y = 0.03$  is at the center of the channel. The cross-stream vorticity in the channel is very small (close to zero) except near the walls for all three sections. Vorticity forms near the walls due to the development of the boundary layer and continues to grow and develop in the direction of the streamwise flow. Vorticity near the walls is due to high velocity gradient in the boundary layer. The effect of proximity to the lower channel wall is seen for plane at  $y = 0.0095$  m in the form of small vorticity at side walls. Close to the exit of the channel, the vorticity can be seen breaking away from the wall into the channel resulting in mixing. Figure 6.6 shows conserved passive scalar contours at the same three locations in the cross-stream direction. At  $y = 0.0095$  m, which is at the center of lower feed stream, the scalar concentration is zero for most of the channel. Beyond a streamwise distance of  $0.7$  m however, the scalar concentration increases and mixing develops. The section  $y = 0.03$  m is located in the faster feed stream and the scalar concentration is unity for

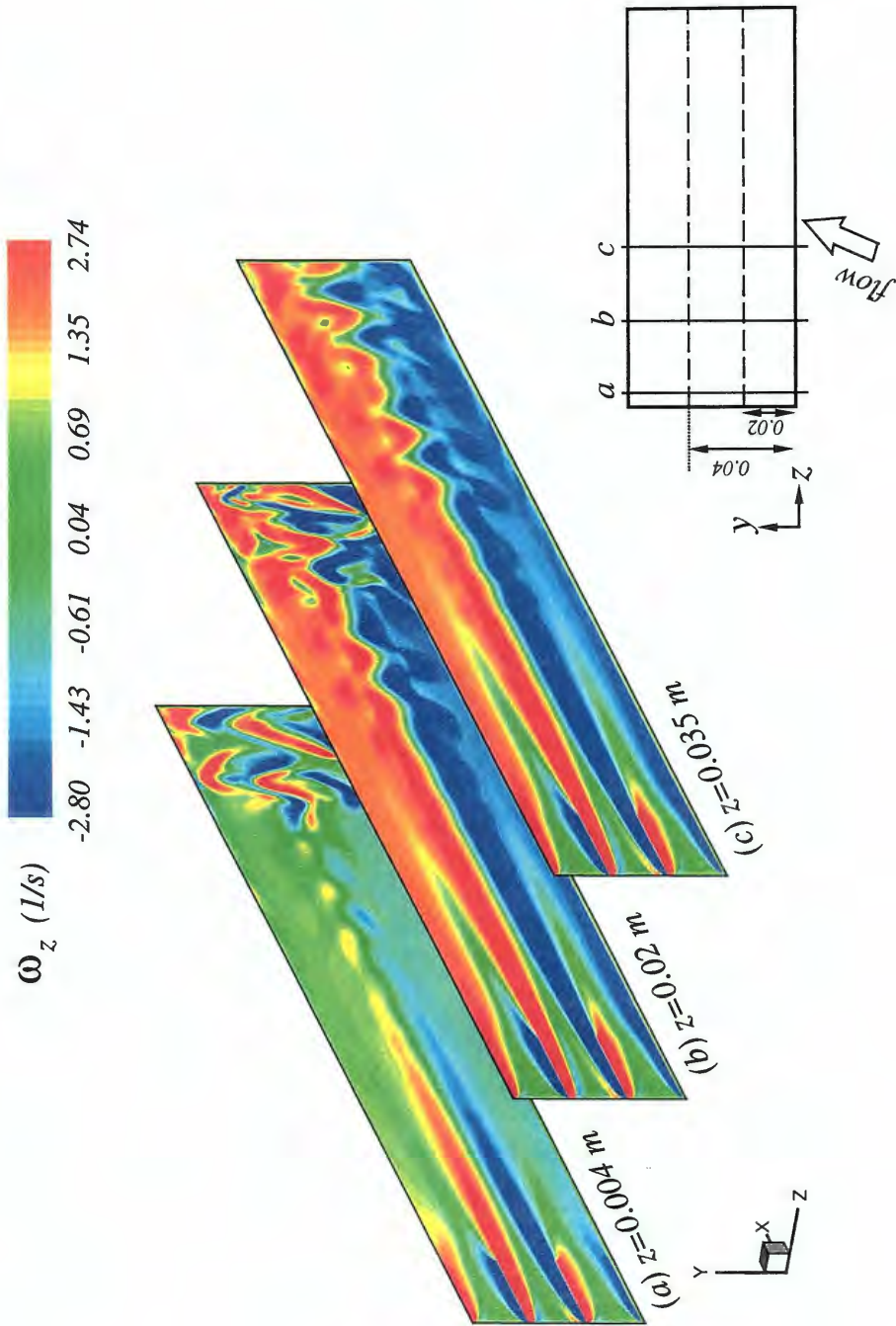


Figure 6.3 Spanwise vorticity contours at three spanwise planes for  $Re = 1500$ ,  $t = 75$  s,  $r = 0.3$ .

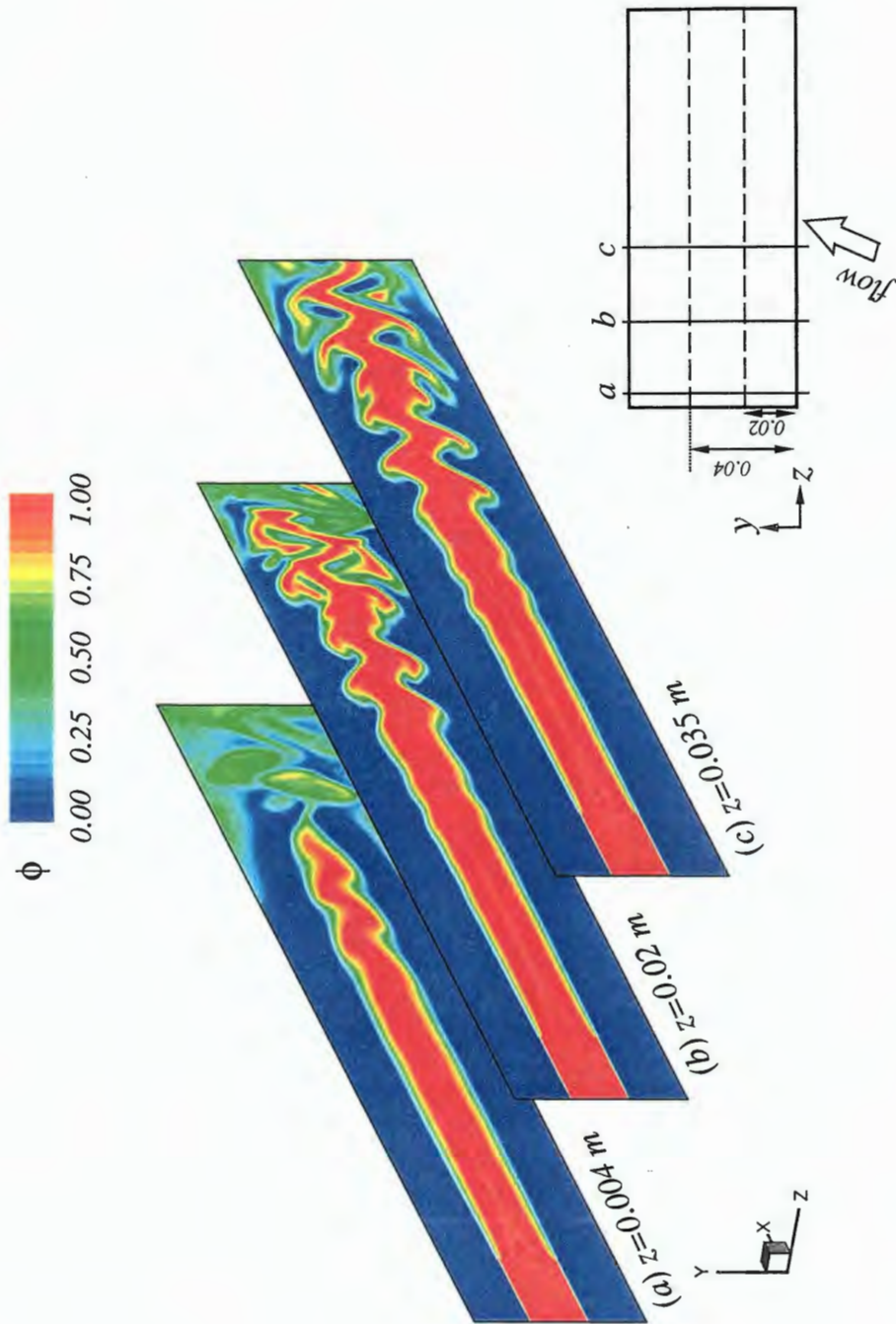


Figure 6.4 Conserved scalar contours at three spanwise locations for  $Re = 1500$ ,  $t = 75$  s,  $r = 0.3$ .

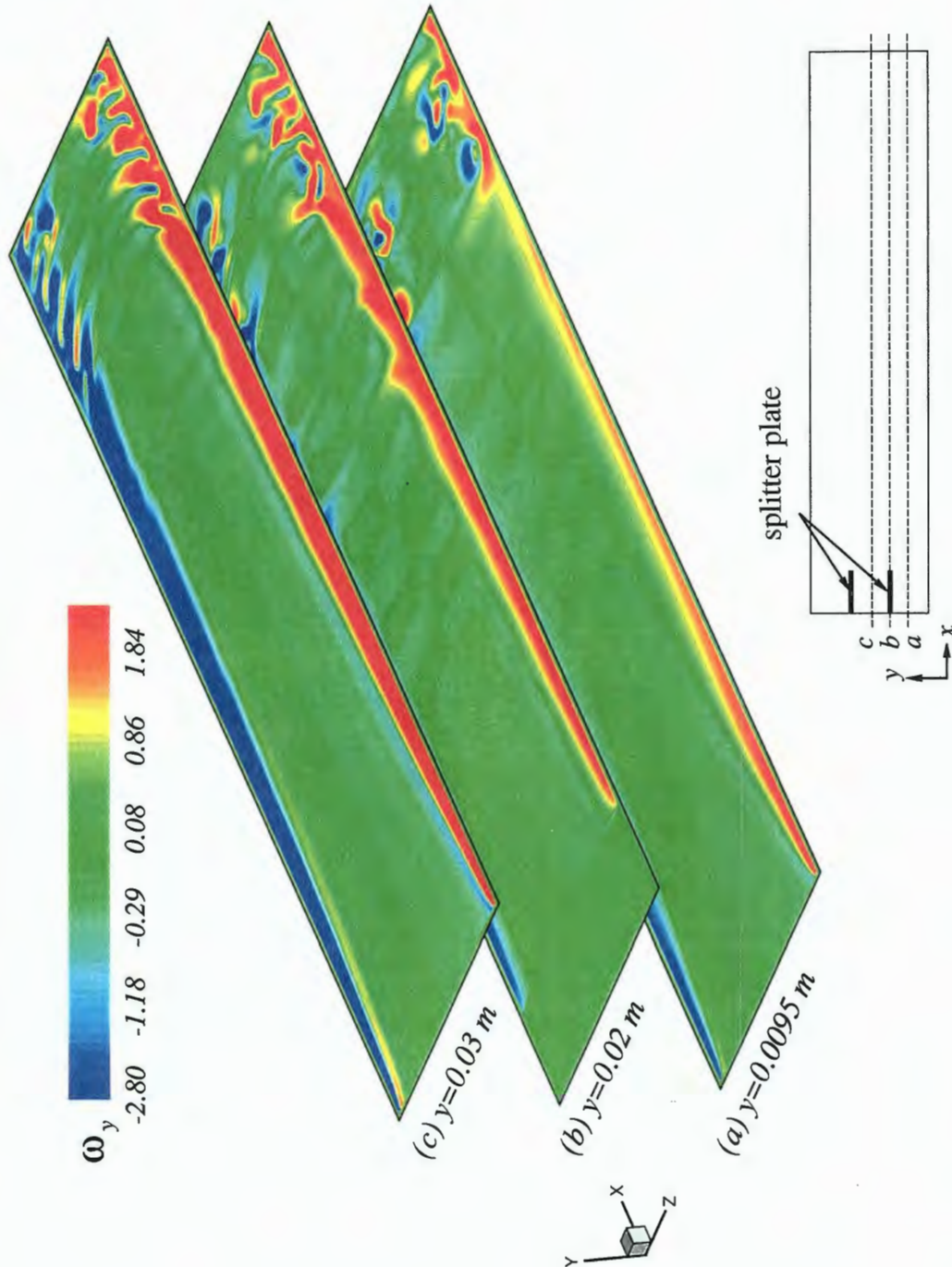


Figure 6.5 Cross-stream vorticity contours at three cross-stream planes for  $Re = 1500$ ,  $t = 75$  s,  $r = 0.3$ .

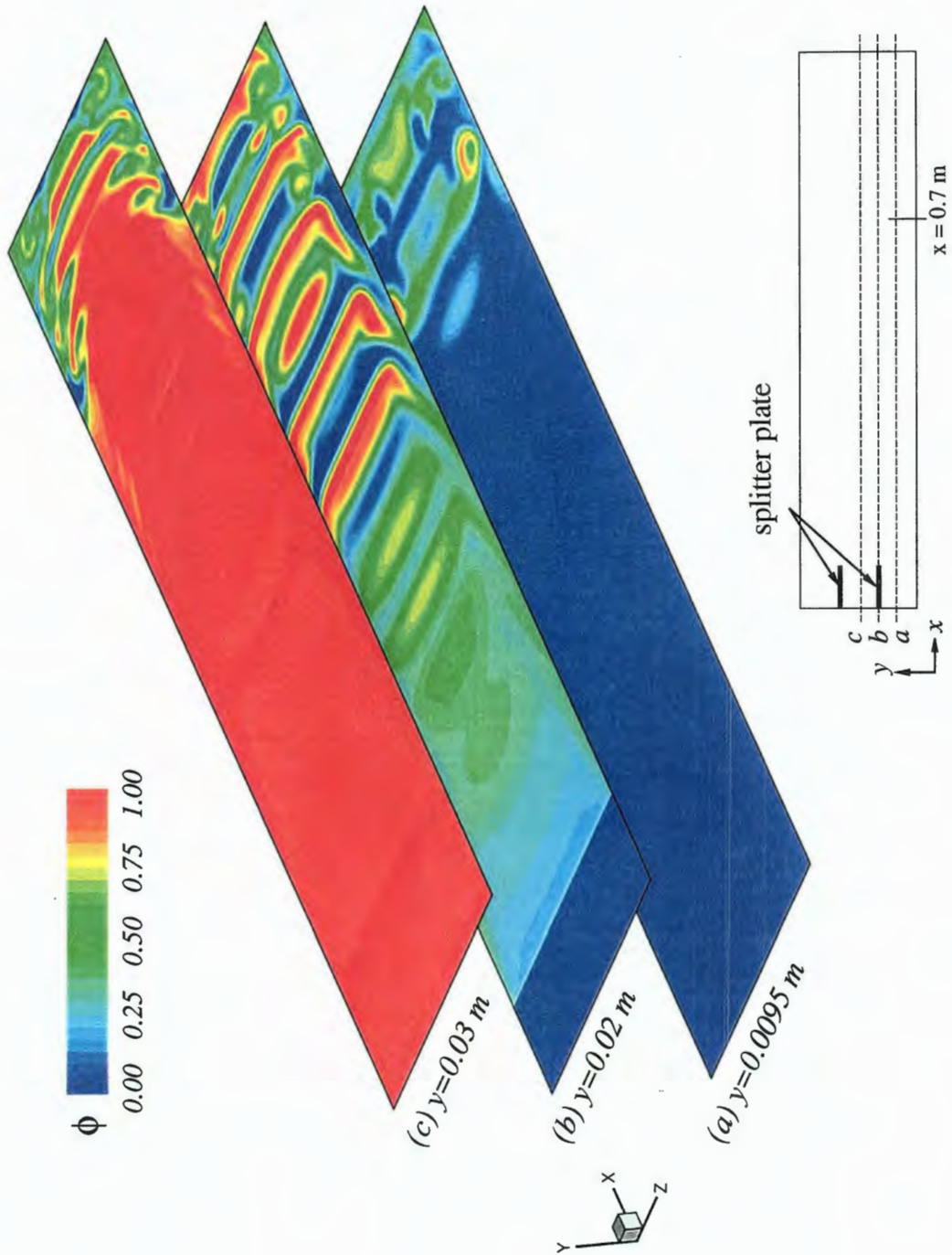


Figure 6.6 Conserved scalar contours at three cross-stream locations for  $Re = 1500$ ,  $t = 75$  s,  $r = 0.3$ .

most of the streamwise length. Beyond  $x = 0.7$  m, the slower stream mixes with the faster stream as observed by the lower scalar concentration. The section at  $y = 0.02$  m is in the plane of the splitter plate and hence at the center of the shear layer. Here alternate bands of fast and slow stream fluids can be seen (alternate red and blue bands). This clearly reveals that the two streams across the shear layer are alternately entrained in the mixing layer.

Figure 6.7 depicts the three-dimensional vorticity magnitude. The plot is an iso-contour of magnitude  $2.5$   $1/s$ . The dominant spanwise vorticity is clearly seen close to the channel exit. Streamwise vorticity evolves in the form of ring-like structures in the strain field of two-dimensional structures. Lin and Corcos [65] have found that sheets of streamwise vorticity sometimes form concentrated round vortex filaments under certain conditions of strain, vortex spacing and viscosity. These streamwise filaments do not inhibit further two-dimensional pairing. Figure 6.8 shows the streamwise vorticity at  $x = 0.7, 0.8, 0.9$  and  $1.0$  m. Initially, the round vortex filaments seen in Fig. 6.7 can be seen at  $x = 0.7$  and  $0.8$  m, and the vorticity has high values near the walls. There is, however, a sudden change in streamwise vorticity at  $x = 0.9$  m. Between  $x = 0.8$  and  $0.9$  m, the vortical structures break down, although the vorticity remains close to the walls. At  $x = 1.0$  m, the vorticity further evolves and progresses into the channel, away from the walls. Figure 6.9 shows scalar contours at the same streamwise locations. At  $x = 0.7$  m, the central fast stream (red) can be seen distinctly in the upper and lower slow streams (blue). At  $x = 0.8$  m, although the central red scalar concentration is seen, some mixing has occurred as observed from the green contours appearing in the upper feed stream. At  $x = 0.9$  m and beyond, the central scalars diffuse into the upper and lower feed streams and mixing develops.

In this chapter, preliminary results were presented on the direct numerical simulations of the three-dimensional evolution of mixing layer using a coarse grid. As Reynolds number increases, the range of turbulent scales increases and the size of smallest scales

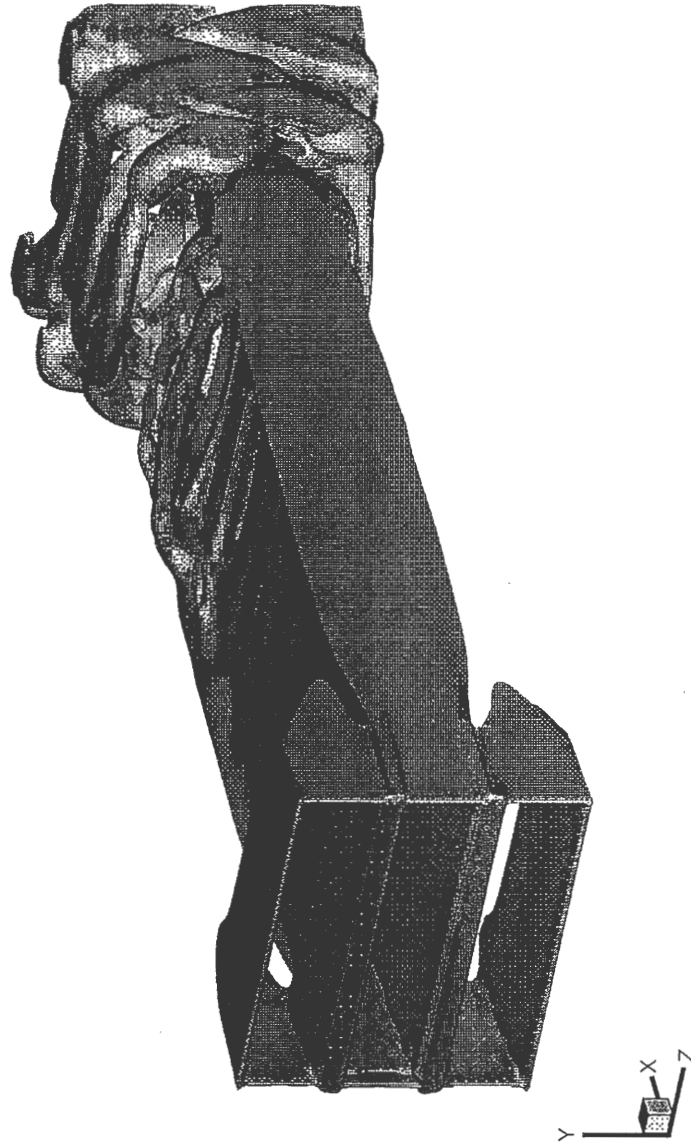


Figure 6.7 Three-dimensional iso-vorticity contours of magnitude  $2.5 \text{ 1/s}$  for  $Re = 1500$ ,  $t = 75 \text{ s}$ ,  $r = 0.3$ .

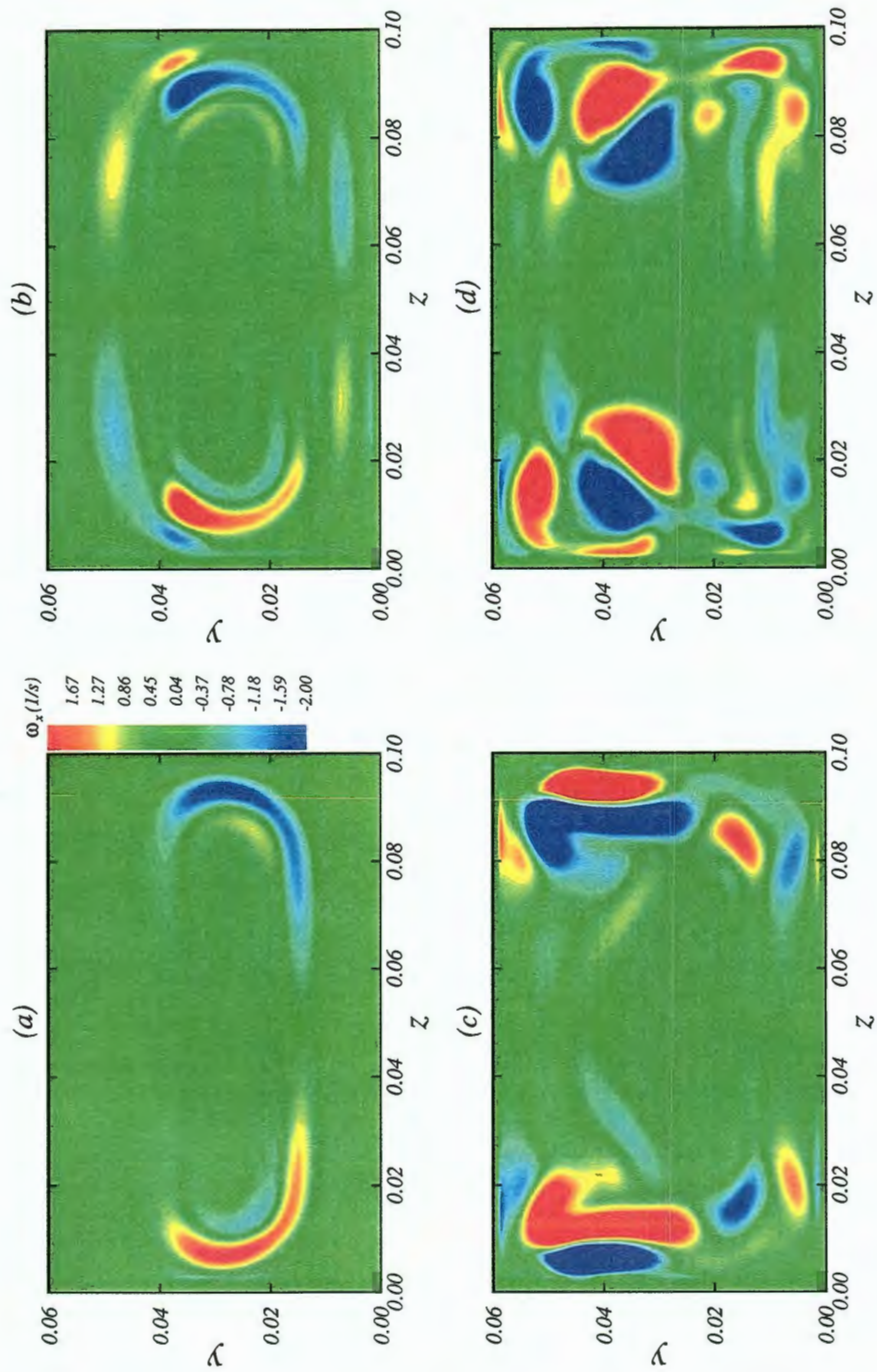


Figure 6.8 Streamwise vorticity at locations for  $Re = 1500$  (a)  $x = 0.7$  m, (b)  $x = 0.8$  m, (c)  $x = 0.9$  m, (d)  $x = 1.0$  m,  $t = 75$  s,  $r = 0.3$ .

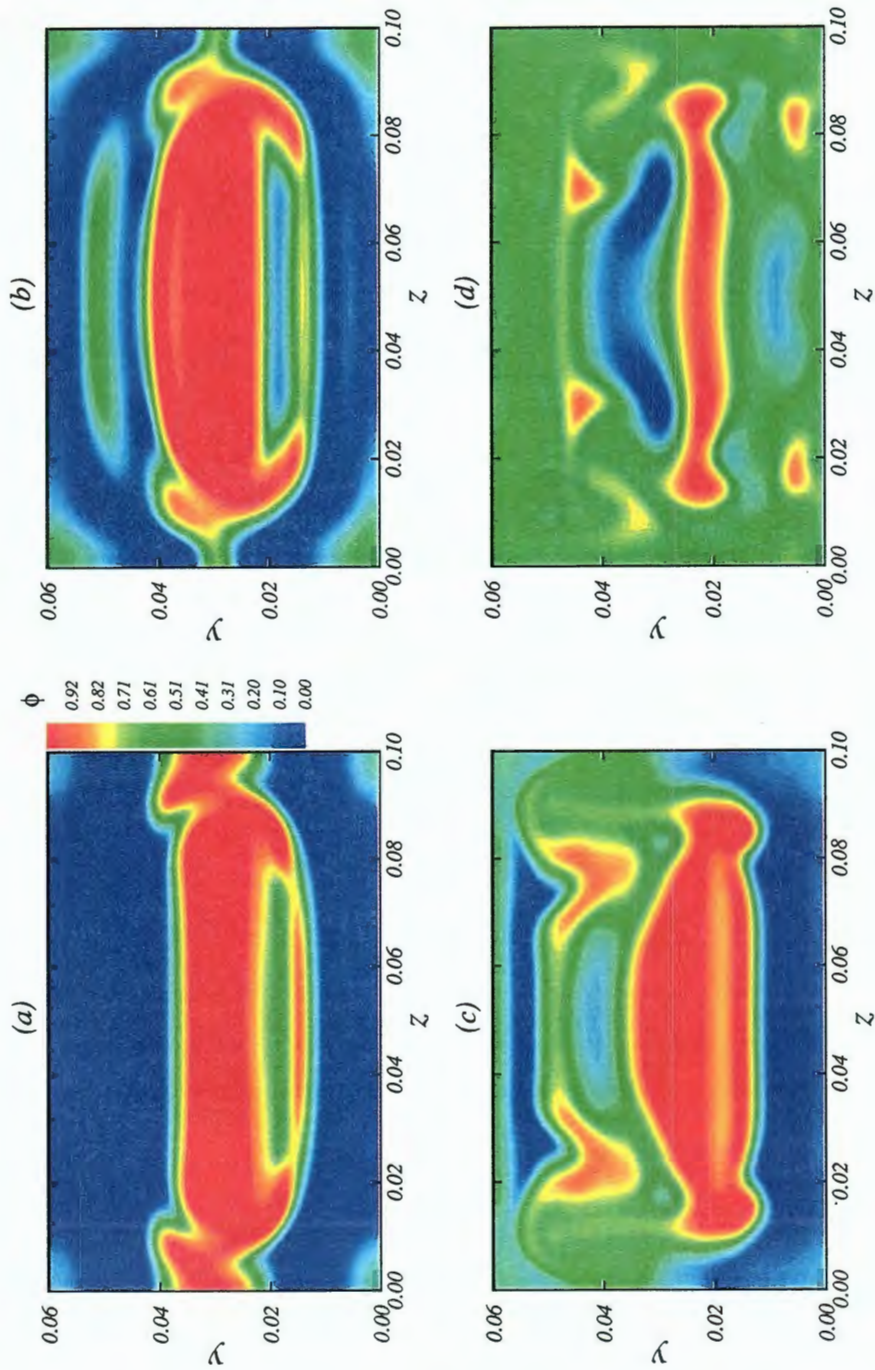


Figure 6.9 Conserved scalar contours at locations for  $Re = 1500$  (a)  $x = 0.7$  m, (b)  $x = 0.8$  m, (c)  $x = 0.9$  m, (d)  $x = 1.0$  m,  $t = 75$  s,  $r = 0.3$ .

reduces further. In order to capture all the relevant scales, the grid size required for the simulation increases exponentially leading to high memory and CPU time requirements. Hence to run efficient three-dimensional, high Reynolds number simulations, the code must be parallelized using Message Passing Interface. This will enable the usage of as many processors as needed, to speedup the simulations. The following chapter summarizes the important results obtained and recommendations for future work.

## CHAPTER 7 CONCLUDING REMARKS

Turbulent mixing processes are of great importance in reacting flows owing to the fact that turbulence induces reactants to mix rapidly thereby increasing the reaction rate. A splitter plate configuration is a well-studied geometry, known to induce mixing as a result of the Kelvin-Helmholtz instability in shear layers. A turbulent mixing flow exhibits complex dynamic behavior and the advection of a passive scalar, such as a reactant, by the same flow reveals many phenomenological parallels with the behavior of the velocity field. Direct numerical simulations have been established as important tools for research in turbulent fluid mechanics. A highly resolved simulation precludes the need for closure models. Detailed information can be obtained in places where it is difficult to obtain experimental data.

In this research, direct numerical simulations are performed for the evolution of mixing layer in a reactor with two splitter plates at the inlet. Detailed field information is obtained by solving the unsteady Navier-Stokes equations. The two-dimensional simulations of the unsteady, spatially developing mixing layer are able to capture the large-scale vortical structures that are shed at the trailing edge of the splitter plates. Instabilities are generated and are a consequence of the Kelvin-Helmholtz mechanism which constitute dominating factors in the roll-up of coherent vortices. It is found that growth of the mixing layer is due to pairing of neighboring vortices. The vortex pairs rotate around each other and coalesce giving rise to a larger vortex. Instability increases as velocity ratio decreases and the vortex roll ups occur closer to the trailing edge of splitter plates. The vortex strength also increases with decrease in velocity ratio.

Mean velocity profiles show that the fast central stream is able to penetrate the outer streams better as the velocity ratio decreases. Reynolds stresses reveal that the turbulent momentum flux is transferred from the center of the channel towards the channel walls along the stream wise direction.

The transport of a conserved passive scalar is examined to assess the mechanisms of entrainment and mixing within the shear flow. The scalars mix in the channel by means of advection and diffusion. As the streamwise distance from the splitter plates increases, the scalars mix rapidly and is a result of growth of the mixing layer. Better mixing at low velocity ratios is attained due to increased advection. Mean scalar profiles reveal that as the velocity ratio decreases, the scalar mixes rapidly and this is demonstrated by a flat scalar profile. Scalar RMS profiles emphasize the fact that mixing is enhanced when the inner feed stream is much faster than outer feed streams. Scalar PDFs reveal that the preferred scalar concentrations at different streamwise locations decrease as velocity ratio decreases from 0.5 to 0.3. This is a result of efficient mixing.

The results obtained through these direct simulations are then used to assess the validity of the gradient diffusion closures in modeling the cross-stream turbulent convective flux of the streamwise velocity and the scalar variable and the validity of turbulent viscosity hypothesis. Assessments were made for the purpose of potential applications of the viscosity and gradient closure model in boundary layer simulations of the averaged transport equations. The results of this assessment predict reasonable values of turbulent viscosity. However, the model fails to account for the effect of convective transport of scalar quantities for general applications.

A coarse-grid three-dimensional simulation is performed to ascertain the ability of the code to solve the Navier-Stokes equations. The vorticity rollups were delayed due to the coarse grid. Round streamwise vortical structures were observed in the channel. It was concluded that the use of multiple processors is necessary in order to solve three-dimensional problems at high Reynolds numbers.

Future work is suggested as follows:

1. Provide turbulence at inlet in order to trip the flow early.
2. Parallelize the present version of serial code using Message Passing interface to solve three-dimensional, high Reynolds number flows.
3. Solve for reacting scalars in addition to passive scalars and compare their probability density functions along the mixing layer.
4. Use large eddy simulations to study the mixing layer problem.
5. Validate DNS results against experimental data and provide flow statistics at places where it is difficult to measure experimentally.

## Bibliography

- [1] Pope, S.B., *Turbulent Flows*, Cambridge University Press, New York, 1 edition, 2000.
- [2] Moin, P. and Krishnan, M., DIRECT NUMERICAL SIMULATION: A Tool in Turbulence Research, *Annual Review of Fluid Mechanics*, **30**:539–578 (1998).
- [3] Friedrich, R., Hüttl, T., Manhart, M., and Wagner, C., Direct numerical simulation of incompressible turbulent flows, *Computers and Fluids*, **30**:555–579 (2001).
- [4] Fox, R. O., Computational methods for turbulent reacting flows in the chemical process industry, *Revue de l'Institut Francais du Petrolé*, **51**:215–243 (1996).
- [5] Eswaran, V. and Pope, S.B., Direct numerical simulations of the turbulent mixing of a passive scalar, *Physics of Fluids*, **31**(3):506–520 (1988).
- [6] Shraiman, B.I. and Siggia, E.D., Scalar Turbulence, *Nature*, **405**:639–646 (2000).
- [7] Deshpande, M., Feng, J.-Z., and Merkle, C., Cavity Flow Predictions Based on the euler Equations, *Journal of Fluids Engineering*, **116**:36–44 (1994).
- [8] Battaglia, F., Tavener, S., Kulkarni, A., and Merkle, C., Bifurcation of Low Reynolds Number Flows in Symmetric Channels, *AIAA Journal*, **35**(1):99–105 (1997).
- [9] Winant, C.D. and Browand, F.K., Vortex pairing: the mechanism of turbulent mixing-layer growth at moderate Reynolds number, *Journal of Fluid Mechanics*, **63**:237–255 (1974).
- [10] Brown, G.L. and Roshko, A., On density effects and large structure in turbulent mixing layers, *Journal of Fluid Mechanics*, **64**:775–816 (1974).
- [11] Roshko, A., Structure of Turbulent Shear Flows: A New Look, *AIAA Journal*, **14**(10):1349–1357 (1976).
- [12] Browand, F.K. and Weidman, P.D., Large scales in the developing mixing layer, *Journal of Fluid Mechanics*, **76**:127–144 (1976).
- [13] Dimotakis, P.E. and Brown, G.L., The mixing layer at high Reynolds number: large-structure dynamics and entrainment, *Journal of Fluid Mechanics*, **78**:535–560 (1976).

- [14] Ho, C.-M. and Huang, L.-S., Subharmonics and vortex merging in mixing layers, *Journal of Fluid Mechanics*, **119**:443–473 (1982).
- [15] Browand, F.K. and Ho, C.-M., The mixing layer: An example of quasi two-dimensional turbulence, *Journal de Mécanique théorique et appliquée Numéro spécial*, pp. 99–120 (1983).
- [16] Dimotakis, P.E., Two-Dimensional Shear-Layer Entrainment, *AIAA Journal*, **24**(11):1791–1796 (1986).
- [17] Koochesfahani, M.M. and Dimotakis, P.E., Mixing and chemical reactions in a turbulent liquid mixing layer, *Journal of Fluid Mechanics*, **170**:83–112 (1986).
- [18] Slessor, M.D., Bond, C.L., and Dimotakis, P.E., Turbulent shear-layer mixing at high Reynolds numbers: effects of inflow conditions, *Journal of Fluid Mechanics*, **376**:115–138 (1998).
- [19] Spencer, B.W. and Jones, B.G., Statistical investigation of pressure and velocity fields in the turbulent two-stream mixing layer, *AIAA 4th Fluid and Plasma Dynamics Conference*, Palo Alto, California, June 21–23 1971.
- [20] Hussain, A.K. and Clark, A.R., On the coherent structure of the axisymmetric mixing layer: a flow visualization study, *Journal of Fluid Mechanics*, **104**:263–294 (1981).
- [21] Wood, D.H. and Bradshaw, P., A turbulent mixing layer constrained by a solid surface. Part 1. Measurements before reaching the surface, *Journal of Fluid Mechanics*, **122**:57–89 (1982).
- [22] Davis, R.W. and Moore, E.F., A numerical study of vortex merging in mixing layers, *Physics of Fluids*, **28**(6):1626–1635 (1985).
- [23] Korczak, K.Z. and Wessel, R.A., Mixing Control in a Plane Shear Layer, *AIAA Journal*, **27**(12):1744–1751 (1989).
- [24] Battaglia, F. and Givi, P., Direct Lagrangian Simulations of a Mixing Layer by the Transport-Element Method, *Journal of Non-Equilibrium Thermodynamics*, **18**:173–194 (1993).
- [25] Koochesfahani, M.M., Dimotakis, P.E., and Broadwell, J.E., Chemically reacting turbulent shear layers, AIAA paper 83-0475, New York, 1983.
- [26] Mungal, M.G. and Dimotakis, P.E., Mixing and combustion with low heat release in a turbulent shear layer, *Journal of Fluid Mechanics*, **148**:349–382 (1984).
- [27] Grinstein, F.F., Oran, E.S., and Boris, J.P., Numerical simulations of asymmetric mixing in planar shear flows, *Journal of Fluid Mechanics*, **165**:201–220 (1985).

- [28] Masutani, S.M. and Bowman, C.T., The structure of a chemically reacting plane mixing layer, *Journal of Fluid Mechanics*, **172**:93–126 (1986).
- [29] Michalke, A., On spatially growing disturbance in an inviscid shear layer, *Journal of Fluid Mechanics*, **23**:521–544 (1965).
- [30] Jaber, F.A., Colucci, P.J., James, S., Givi, P., and Pope, S.B., Filtered mass density function for large-eddy simulation of turbulent reacting flows, *Journal of Fluid Mechanics*, **401**:85–121 (1999).
- [31] Gicquel, L., Givi, P., Jaber, F.A., and Pope, S.B., Velocity filtered density function for large eddy simulation of turbulent flows, *Physics of Fluids*, **14**(3):1196–1213 (2002).
- [32] Toor, H.L., Mass transfer in dilute turbulent and non turbulent systems with rapid irreversible reactions and equal diffusivities, *AIChE Journal*, **8**:70–78 (1962).
- [33] Batt, R.G., Turbulent mixing of passive and chemically reacting species in a low-speed shear layer, *Journal of Fluid Mechanics*, **82**:53–95 (1977).
- [34] Breidenthal, R.E., Structure in turbulent mixing layers and wakes using chemical reaction, *Journal of Fluid Mechanics*, **109**:1–24 (1981).
- [35] Mungal, M.G., Hermanson, J.C., and Dimotakis, P.E., Reynolds number effects on mixing and combustion in a reacting shear layer, *AIAA Journal*, **23**:1418–1423 (1985).
- [36] Karasso, P.S. and Mungal, M.G., Scalar mixing and reaction in plane liquid shear layers, *Journal of Fluid Mechanics*, **323**:23–63 (1996).
- [37] Pope, S.B., A Monte Carlo method for the PDF equations of turbulent reactive flow, *Combustion Science and Technology*, **25**:159–174 (1981).
- [38] Kollmann, W. and Janicka, J., The probability density function of a passive scalar in turbulent shear flows, *Physics of Fluids*, **25**:1755–1769 (1982).
- [39] Jones, W.P. and Whitelaw, J.H., Calculation methods for reacting turbulent flows: A review, *Combustion and Flame*, **48**:1–26 (1982).
- [40] Bernal, L.P. and Roshko, A., Streamwise vortex structure in plane mixing layers, *Journal of Fluid Mechanics*, **170**:499–525 (1986).
- [41] Lasheras, J.C., Cho, J.S., and Maxworthy, T., On the origin and evolution of streamwise vortical structures in a plane, free shear layer, *Journal of Fluid Mechanics*, **172**:231–258 (1986).
- [42] Lasheras, J.C. and Choi, H., Three-dimensional instability of a plane free shear layer: an experimental study of the formation and evolution of streamwise vortices, *Journal of Fluid Mechanics*, **189**:53–86 (1988).

- [43] Rogers, M.M. and Moser, R.D., The three-dimensional evolution of a plane mixing layer: the Kelvin-Helmholtz rollup, *Journal of Fluid Mechanics*, **243**:183–226 (1992).
- [44] Wiecek, K.C. and Mehta, R.D., Effects of velocity ratio on mixing layer three-dimensionality, *Experimental Thermal and Fluid Science*, **16**:165–176 (1998).
- [45] Rogers, M.M. and Moser, R.D., Spanwise scale selection in plane mixing layers, *Journal of Fluid Mechanics*, **247**:321–337 (1993).
- [46] Moser, R.D. and Rogers, M.M., The three-dimensional evolution of a plane mixing layer: Pairing and transition to turbulence, *Journal of Fluid Mechanics*, **247**:275–320 (1993).
- [47] White, F.M., *Viscous Fluid Flow*, McGraw-Hill, New York, 1991.
- [48] Fletcher, C.A.J., *Computational Techniques for Fluid Dynamics*, Springer Series in Computational Physics, Vol. I, Springer-Verlag, New York, 1988.
- [49] Peyret, R. and Viviani, H., Computation of viscous compressible flows based on the Navier-Stokes equations, *AGARDograph*, **2** (1975).
- [50] Merkle, C.L., Unified time-marching procedure for compressible and incompressible flow, Proceedings of the International Conference on Hydrodynamics, Wuxi, China, 1994.
- [51] A., Chorin. A numerical method for solving incompressible viscous flow problems, *Journal of Computational Physics*, **2**:191–209 (1967).
- [52] Merkle, C.L. and Athavale, M.M., Time-accurate unsteady incompressible flow algorithms based on artificial compressibility, *8th AIAA Computational Fluid Dynamics Conference*, AIAA Paper 87-1137, 1987.
- [53] Venkateswaran, S. and Merkle, C.L., Dual time stepping and preconditioning for unsteady computations, *33rd Aerospace Sciences Meeting & Exhibit*, AIAA Paper 95-0078, Reno, Nevada, January 1995.
- [54] John C. Tannehill, Dale A. Anderson and Pletcher, Richard H., *Computational Fluid Mechanics and Heat Transfer*, Taylor and Francis, Washington DC, 2 edition, 1997.
- [55] Hoffmann, K.A., *Computational Fluid Dynamics for Engineers*, Engineering Education System, Austin, Texas, 1989.
- [56] Merkle, C.L. and Tsai, Y.L., Application of Runge-Kutta schemes to incompressible flows, *24th AIAA Aerospace Sciences Meeting*, AIAA Paper 86-0553, Reno, Nevada, January 1986.

- [57] Kwak, D., Chang, J., Shanks, S., and Chakravarthy, S., A three-dimensional Navier-Stokes flow solver using primitive variables, *AIAA Journal*, **24**:390–396 (1986).
- [58] Tsai, Y.L., Time marching schemes for solving the Euler equations, PhD thesis, Dept. of Mechanical Engineering, Pennsylvania State Univ., 1988.
- [59] Fletcher, C.A.J., *Computational Techniques for Fluid Dynamics*, Springer Series in Computational Physics, Vol. II, Springer-Verlag, New York, 2 edition, 1991.
- [60] Warhaft, Z., Passive scalars in turbulent flows, *Annual Review of Fluid Mechanics*, **32**:203–240 (2000).
- [61] Chaté, H., Villiermaux, E., and Chomaz, J., *Mixing Chaos and Turbulence*, NATO ASI Series, Series B:Physics, Vol. 373, Advanced Science Institutes, 1999.
- [62] Mitrani, I., *Probabilistic Modelling*, Cambridge University Press, UK, 1998.
- [63] Boussinesq, J., Essai Sur La Théorie Des Eaux Courantes, *Mem. Présentés Acad. Sci.*, **23**:46 (1877).
- [64] Givi, P. and Jou, W.-H., Mixing and Chemical Reaction in a Spatially Developing Mixing Layer, *Journal of Non-equilibrium thermodynamics*, **13**:355–372 (1988).
- [65] Lin, S.J. and Corcos, G.M., The mixing layer: deterministic models of a turbulent flow. Part 3. The effect of plane strain on the dynamics of streamwise vortices, *Journal of Fluid Mechanics*, **141**:139–178 (1984).

## ACKNOWLEDGEMENTS

I would like to sincerely thank Dr. Battaglia for her invaluable guidance and encouragement. I would also like to thank my committee members Dr. Fox, especially for the knowledge gained from his course (ChemE 652), and Dr. Pletcher, for his participation and suggestions. I would also like to acknowledge Dr. Hill for his suggestions in our meetings. I would like to thank people in the CFD lab (0095D) - Chunjian, Farshid, Jin, John, Joon, Kunlun, Nan, Ravi, Steve, Xiaofeng and Yang for all their help and for a wonderful time and students from chemical engineering, Mothi and Venkat for their help and support.

Finally, the love, support and patience of my family and friends is greatly appreciated.